

Alma Mater Studiorum – Università di Bologna

**DOTTORATO DI RICERCA IN
MECCANICA E SCIENZE AVANZATE DELL'INGEGNERIA**

Ciclo XXXII

Settore Concorsuale: 09/C2

Settore Scientifico Disciplinare: ING-IND/18

**DEPOSITION OF THIN FILMS BY A NON-EQUILIBRIUM ATMOSPHERIC
PRESSURE PLASMA JET: A POLY-DIAGNOSTIC STUDY**

Presentata da: Federica Barletta

**Coordinatore Dottorato
Prof. Marco Carricato**

**Supervisore
Prof. Vittorio Colombo**

**Co-supervisore
Dr. Matteo Gherardi**

Esame finale anno 2020

“In doing something, do it with love or never do it at all”

-

Mahatma Ghandi

Table of Contents

Abstract	3
1. Introduction	6
1.1 Atmospheric pressure plasmas for thin films deposition on thermo-sensitive materials: a general overview	6
1.2 SiO ₂ -based thin films.....	9
1.3 Scientific background on plasma polymerized TEOS thin films	12
1.3.1 Overview on APPs for SiO ₂ thin films deposition using TEOS as precursor	12
1.3.2 Overview on LPPs for SiO ₂ thin films deposition using TEOS as precursor	16
1.4 Outline/scope of the thesis.....	18
1.5 Publications	20
1.5.1 Publications in international journals	20
1.5.2 Publications in international journals	20
1.6 References	22
2. Thin films: surface characterization	27
2.1 Materials and methods	27
2.1.1 Atmospheric Pressure Plasma Jet (APPJ) for thin film deposition	27
2.1.1.1 Plasma deposition system.....	29
2.1.1.2 Operating conditions and electrical characterization ..	31
2.1.2 ATR-FTIR	32
2.1.2.1 ATR-FTIR measurement settings	34
2.1.3 XPS	34
2.1.3.1 XPS measurement settings	35
2.1.4 AFM	35
2.1.4.1 AFM measurement settings	36
2.1.5 SEM	36
2.1.5.1 SEM measurement settings	37
2.2 Results and discussion	38
2.2.1 Chemical structure	38
2.2.2 Morphological structure and thickness measurements	44
2.2.3 Substrate temperature	48

2.3	Conclusions	51
2.4	References	51
3.	Insights of Ar/TEOS gas-phase processes: excited-state species	55
3.1	Materials and methods	56
3.1.1	<i>OES and fast imaging set-up</i>	<i>56</i>
3.1.2	<i>Gas temperature and electron density measurements</i>	<i>57</i>
3.1.3	<i>Rayleigh scattering experiment.....</i>	<i>58</i>
3.2	Results and discussion	60
3.2.1	<i>Emission spectra analysis and T_{gas} measurements.....</i>	<i>60</i>
3.2.2	<i>Electron density measurements.....</i>	<i>65</i>
3.2.3	<i>Phase-resolved measurements</i>	<i>67</i>
3.2.4	<i>Time-resolved discharge imaging</i>	<i>69</i>
3.3	Conclusions	71
3.4	References	72
4.	Insights of Ar/TEOS gas-phase processes: ground-state species	75
4.1	Materials and methods	78
4.1.1	<i>OH-LIF measurements</i>	<i>79</i>
4.1.2	<i>CH-LIF measurements</i>	<i>81</i>
4.1.3	<i>O-TALIF measurements</i>	<i>81</i>
4.2	Results and discussion	83
4.2.1	<i>O atoms: precursor and voltage effect</i>	<i>84</i>
4.2.2	<i>Two-dimensional LIF imaging of OH radicals in Ar/TEOS plasmas.....</i>	<i>88</i>
4.2.3	<i>Two-dimensional LIF imaging of CH radicals in Ar/TEOS plasmas</i>	<i>91</i>
4.3	Conclusions	93
4.4	References	94
5.	General conclusions & Outlooks	97
	Annex I.....	100
	Acknowledgement	105

ABSTRACT

The use of atmospheric pressure plasmas (APPs) for thin film deposition on thermo-sensitive materials is currently one of the main challenges of the plasma community. Indeed, over the last years, the number of research groups working in the above-mentioned field, the amount of papers published on this topic and the industrial interest for innovative atmospheric plasma technologies for thin films deposition have been constantly growing. Nevertheless, the understanding of APPs for deposition purposes is still immature as compared to other application fields since additional heavy molecules (the thin film precursors) are present within the discharge, inducing an increased complexity of the gas-phase reaction kinetics.

In this respect, the existing knowledge gap between gas-phase reaction mechanisms and thin film properties is one of the most important barriers to overcome for a successful process control and optimization of thin film performances. Accordingly, the best way to progress in this complex research area consists in a fully comprehensive step-by-step study of the process by means of several different gas-phase diagnostic tools and surface characterization techniques in order to establish a clear correlation between the selected external plasma parameters and the resulting surface features.

Among the many precursors available for modifying the surface properties of thermo-sensitive materials by APPs, organosilicon compounds have always attracted wide attention because of their organic-inorganic behaviour, low cost and relatively non-toxic character. In particular, Tetraethyl orthosilicate (TEOS, $[\text{Si}(\text{OC}_2\text{H}_5)_4]$) is often preferred for plasma-polymerization processes since its easily convertible into Si-based thin films, well suited for a large number of applications such as barrier films for food and beverage packaging, functional coatings for biomedical implants or hard protective layers for electronic devices.

Despite TEOS is widely used in case of APPs, the dominant gas-phase processes and the most important monomer fragmentation pathways have not yet been completely identified in atmospheric pressure conditions. In view of this, in the present dissertation an in-depth study of an atmospheric pressure plasma jet (APPJ) specifically designed for the deposition of thin films by using an Ar/Tetraethyl orthosilicate (TEOS) mixture is undertaken. The APPJ source under investigation is an AC-driven Corona-jet configuration facing a grounded dielectric plate that allows to obtain deposits in ambient air on different kind of materials and complex surfaces without the use of expensive vacuum equipments.

As a first step of the study, the effect of several process parameters, such as applied power and gas mixture, on the film surface structure and chemistry is determined by various surface characterization techniques. In details, Attenuated total reflectance-Fourier transform infrared spectroscopy (ATR-FTIR) and X-ray photoelectron spectroscopy (XPS) are employed for an exhaustive description of the thin films chemical structure. ATR-FTIR spectroscopy results highlight the presence, for the whole range of studied operating conditions, of strong absorption Si-O-Si peaks and Si-OH silanol bonds, highly representative of the thin films inorganic behaviour and density respectively. On the other hand, complementary analysis of the silica-like film quality, performed by spatially resolved XPS measurements, show a change in terms of chemical composition across of the samples by varying the distance from the Corona-jet high voltage (HV) electrode. Some useful information on thin films roughness and thickness are then provided by Atomic

Force Microscopy (AFM): RMS roughness values remain quite low ($R_q=7-9$ nm) for all cases but the number of small features on the surface clearly grow with increasing applied power. Moreover, AFM results reveal a coating thickness of 0.115 ± 0.04 μm for the lowest power condition tested while a strong heating-up of the thermo-sensitive surface affects thickness measurements in case of high operating conditions. The morphological uniformity of deposits and the possible presence of defects is then discussed by Scanning electron microscopy (SEM). The presence of cracks on the coating deposited at higher power conditions confirms a strong heating-up of the polymeric substrate while the SEM maps performed in 5 different points of the deposit indicate a quite good uniformity in terms of morphology. Lastly, substrate temperature measurement, performed by using an IR camera confirm an overheating of approximately $30-40^\circ\text{C}$ (after 60 second of plasma treatment) in case of higher power conditions, resulting in crack formation on the thin film surface. Otherwise, the absence of defects for low power modes is in line with the low thermal stress detected. Substrate temperature radial profiles highlight also a donut shape temperature distribution probably induced by gas-phase Penning ionization reactions between Ar metastables and ambient air N_2 molecules.

Concerning the gas-phase process, the above mentioned APPJ device working in Ar/TEOS mixtures produce a “cocktail” of highly reactive excited and ground state species, typically generated by collisions with high-energy particles like electrons, ions or Ar metastable atoms. Because of the relative novelty of this research area and the complexity of the mechanisms involved in the atmospheric pressure deposition process, any improvements of such technology pass through a precise poly-diagnostic study of the most relevant species spatial-temporal distribution, density and temperatures.

First, passive optical emission spectroscopy (OES) is used for the gas temperature (T_{gas}) estimation by means of rotational temperature (T_{rot}) calculation from $\text{OH } A^2\Sigma^+ \rightarrow X^2\Pi_i$ (0,0), $\text{N}_2 C^3\Pi_u \rightarrow B^3\Pi_g$ (0,2) and $\text{CH } A^2\Delta \rightarrow X^2\Pi$ (0,0) bands. The obtained results reveal that the rotational temperature of $\text{N}_2(C-B)$ transition, equal to 550 K, is not a realistic estimate of the gas temperature in case of Ar/TEOS plasmas due to quasi-resonance processes with Ar metastables. On the other hand, the rotational temperature of OH excited radicals, obtained in the assumption of a non-Boltzmann rotational distribution, is significantly lower than the one obtained with N_2 molecular bands and its mean value (409 K) is in a good agreement with the result obtained by means of Rayleigh scattering technique. In addition, the Ar metastables as well as the electron impact reactions with TEOS fragments are presumably playing a key role in the CH(A) radical formation leading to an overestimation of the gas temperature (590 K) by CH emission bands in the investigated type of discharges. In order to understand of the most significant pathways of CH(A) formation, TEOS dissociation reactions, electron impact dissociative excitation and Penning reactions are discussed in detail. Electron density, estimated from the Stark broadening of H_α lines, and reactive species dynamics during the AC plasma period are used to clarify the dominant production mechanisms of excited state discharge species. Then, the streamer evolution between the jet electrodes and the spatial-temporal behaviour of excited species is evaluated by means of fast imaging of Ar atoms, O atoms, N_2 molecules, CH and OH radicals for a further step toward the understanding of the main pathways of the process.

Lastly, a detailed analysis of the most relevant plasma non-emitting species is performed by two different active spectroscopy techniques. For the first time Laser Induced Fluorescence (LIF) and Two-photon absorption Laser Induced Fluorescence (TALIF) measurements of OH, CH and O atoms are carried out in case of atmospheric pressure Ar/TEOS plasmas. In detail, the effect of TEOS addition, power applied and air diffusion on the spatial distribution of OH, CH radicals and O atoms is investigated by 2D LIF

imaging. Moreover, the dominant production and recombination processes of such active species are discussed in order to point out the impact of oxidant active species, such as atomic oxygen and hydroxyl radical, on the organic content removal from both gas-phase and adsorbed thin film fragments as well as correlate the physics behind ground state particles generation to the predominant excited state production mechanisms. The results obtained confirm that most of O atom population in pure Ar and Ar/TEOS mixtures is generated by dissociation of water molecules contained in the Ar gas flow due to electron and Ar metastable impact. Nevertheless, it is found that the OH radical production in presence of a high content of hydrocarbon fragments is dominated by recombination processes between O atoms and CH radicals thus revealing the presence of further O atoms loss mechanisms respect the pure Ar case. Moreover, based on the 2D LIF imaging results, the presence of gas-surface reactions able to improve the thin film inorganic content is excluded due to the very low CH radical and O atom signal detected in correspondence of the dielectric plate.

The obtained results, combined with predominant excited species production pathways and thin films features, provide a fully-comprehensive study of the Ar/TEOS atmospheric pressure plasma process primarily aimed at the development of innovative computational models, crucial for a further optimization of the process.

1

INTRODUCTION

This chapter provides a general introduction regarding the use of atmospheric pressure plasma (APPs) for thin film deposition purposes. First, the most significant plasma agents and basic scientific principles involved in polymerization processes on thermo-sensitive materials are summarized to provide some background information essential for a clear understanding of the current work. Second, the use of APPs for the deposition of Si-based thin films is discussed in detail to highlight the lack of clarity related to the dominant gas-phase reactions and the complete absence of reference data about monomer fragmentation pathways in case of TEOS-containing plasmas. Third, an overview of the state of art and the most promising industrial solutions for the deposition of silica-like films starting from TEOS as precursor is presented to clarify the motivation behind the work. At the end, dissertation outlines and scientific works attained over the three-years of research activity are presented.

1.1 Atmospheric pressure plasmas for thin films deposition on thermo-sensitive materials: a general overview

The possibility of avoiding expensive pumping systems, reduce equipment cost and use low process temperatures makes APPs a promising alternative to low pressure (LP) plasmas and chemical vapour deposition (CVD) techniques typically employed for thin film deposition since the mid-20th century.[1],[2] The lack of high temperature which induce the thermal activation of gas-phase reactions, as in the case of CVD, as well as the weak plasma stability, due to low mean free paths of plasma species with respect to conventional LP processes, were just some of the main barriers towards a widespread development of APPs technologies for industrial applications.[3],[4] As proven by the volume of critical reviews published and the number of patents deposited on this topic, a large part of the plasma scientific community has worked on a deeper understanding of APPs over the last two decades aiming to replace the use of “conventional” techniques for thin films deposition.[5]–[7] Despite this, significant additional efforts are required to obtain dense and uniform thin films on complex thermo-sensitive surfaces.

In this regard, a short overview of APPs main competitive advantages with respect to conventional methods for deposition purposes is presented in this introductory paragraph aimed at providing a comprehensive basis to fully understand the relevance of the topic in terms of industrial and scientific outlooks.

First, unlike conventional approaches, in case of APPs technologies the thin film precursor is always diluted in a main gas which acts as plasma gas and carrier flow at the same time.[8] From a physico-chemical and economical point of view, the choice of such main gas is a key factor towards the industrialisation of the process since it has a notable influence on the discharge stability, generation of energetic species, gas temperatures, total process costs and quality of the resulting thin films.[9]–[13] Typically, the gasses most widely utilized in APP processes are noble gasses such as He and Ar due to the presence high energy metastable atoms which largely participate to ionization (through Penning ionization reactions) and collisional processes with precursor molecules.[14] The active participation of metastable atoms in nucleation and thin film growth mechanisms is one of the most significant difference between AP and LP plasma where gas-phase fragmentation processes are strictly induced by electron impact.[15] This discrepancy, together with a different duration of each discharge pulse and spatial-temporal behaviours of ground and excited species, limits the transferability of the knowledge accumulated on low pressure processes to APPs.[16] Accordingly, for a complete understanding and an adequate control of the plasma-assisted deposition process at atmospheric pressure, a completely new different fundamental study of the detailed physics, dominant gas-phase mechanisms and thin films features is needed as a starting point towards the achievement of a well-established technology.

Nevertheless, it is also important to highlight that such technologies, in most cases, work in ambient air and the presence of surrounding air impurities must be taken into account since the thin films chemical and structural uniformity can be affected by gas-phase reactions between electrons/metastable atoms and N_2 , O_2 or H_2O molecules.[17] In order to limit this problem, nowadays, the research is focused on the development of cost-efficient nitrogen-based gas mixtures solutions for thin films deposition.[18] Although this is clearly a further step in the industrial implementation of APPs, the employment of N_2 or air as process gasses reduce considerably the process efficiency due to the lack of metastable atoms and the number of possible plasma configuration suitable for thin film deposition on complex thermo-sensitive surfaces. In general, the introduction of diatomic molecules such as N_2 and O_2 and the consequent increase of chemical reaction process pathways makes the study of the deposition process even more challenging.[19] In the current work, the filamentary Ar and Ar/TEOS plasma discharges studied are sustained in ambient air and the influence of air back diffusion will be considered during the discussion of the obtained results.

In the last years, the large use of polymers in a variety of industrial fields and the need to decrease their environmental impact by reducing the amount of resources used, has prompted the exploration of more lightweight, low-cost and eco-friendly alternative solutions. Among them, the possibility of modifying or improving the polymers functionality by thin films application, using different kind of APPs technologies, is certainly one of the most interesting from an industrial point of view.[20] As known, in contrast to plasmas in equilibrium typically used for CVD of thin films, atmospheric pressure plasma operate far away from the local thermal equilibrium (LTE). In this case, the neutrals remain relatively cold respect excited species making these plasmas suitable for the treatment of thermo-sensitive materials.[21] Despite such very low neutrals temperature, which could be assumed equal to the macroscopic gas temperature (T_{gas}) perceived by the target, provides the possibility of using APPs on a wide range of polymers and plastics in general, the interaction between APPs and thermo-sensitive materials remains a critical issue. Indeed, a polymeric substrate could be affected by a drastic and discontinuous change in terms of structural properties if subjected to temperatures even

slightly higher respect the ambient temperature therefore influencing thin films performances.[22] As a consequence, the gas temperature is one of the most important process parameters and an accurate measurement of T_{gas} is strongly demanded for an adequate deposition process control. In light of this, critical issues, possible solutions and various technique potentially applicable for T_{gas} measurements will be disclosed in detail over the next sections.

The use of APPs has raised great interest also for the versatility of such technologies both in terms of possible device configurations and key parameters which have a significant effect on thin films features.[23],[24] In this regard, it is worth emphasising that nowadays two major categories of APP devices capable of covering a wide range of industrial applications exist. Indeed, conventionally, atmospheric pressure deposition process can be assisted by “direct” or “indirect” plasmas; in the first case active species and precursor fragments are generated directly near the target while, in case of indirect plasma, they are created remotely and carried on the substrate by a gas flow. [25] For the treatment of planar surface, e.g. PET or PP foils for flexible electronic devices, the direct configuration is the best available option given the possibility of performing large area treatments with low gas consumption. Otherwise an indirect configuration, such as atmospheric pressure plasma jet (APPJ) technologies, is the only reasonable choice for the deposition on complex 3D surfaces. Several reviews have extensively discussed advantages and disadvantages of both solutions; however, an accurate understanding of the specific advantages and limits is a fundamental step to justify the “hybrid” APP configuration employed in this work. On the other hand, the determination of the optimal process parameters for the achievement of thin films suitable for industrial application is an even more complex topic. These, indeed, are strongly interdependent and may result in undesirable effects in terms of morphological and chemical thin films properties. By the way, the use of different pulse repetition frequencies and duty cycle (DC) values, the influence of the gas flow-rate and the energy supplied per unit of monomer (Yasuda factor) on thin film features have been deeply investigated in the past.[8],[19] For example, Morent [26] has studied the Yasuda factor effect on HMDSO (Hexamethyldisiloxane) coatings features by varying the amount of precursor and the power applied during the polymerization process. By working in the “monomer deficient region”, where the amount of active species produced is higher respect the number of precursor molecules introduced, inorganic coating can be easily obtained; while thin films including a high organic content have been achieved by operating in the “monomer sufficient region” where the amount of active species produced is lower respect the number of precursor molecules introduced. Otherwise, studies performed by Starostine [27] have highlighted the possibility to deposit powder-free coatings with a pulsing regime achieved through the use of an appropriate duty cycle ($DC = t_{\text{on}} / t_{\text{on}} + t_{\text{off}}$); while Caquineau [28] has shown a strong correlation between the layer non-uniformity and the presence of gas recirculation, due to overly high gas flow-rate, into the discharge zone. Although the results achieved in terms of thin film features are an interesting starting point for an accurate study of the process, are not enough to understand the complex mechanisms which take place over the atmospheric pressure deposition process. Therefore, a good correlation between the plasma parameters selected and the most significant gas-phase mechanisms involved in the deposition process will be discussed in detail over the present dissertation.

In conclusion, it is worth mentioning that atmospheric plasma systems allow the deposition of a wide range of coatings starting from different gas/vapor precursor and, on this point, the critical review of Merche et al. [8] provides an overview of advantages and disadvantages of possible organic and inorganic coatings typically deposited by plasma-assisted processes. Obviously, the choice of these coatings and relative precursors is mostly

dictated by the main industrial users and the search for innovative solutions never comes to an end. Among the many possible ones, nowadays, Si-based coatings are certainly the most studied category thanks to their excellent chemical, thermal, and optical properties. However, because of the relative novelty of this research area in AP conditions, many questions are yet unanswered and some scientific and industrial problems still need to be ironed out. The main goals achieved up to now, the most used precursors and the main open questions of the plasma community on this topic are presented in the next sections.

1.2 SiO₂-based thin films

In the last decades, plasma-polymerized Si-based films have received great interest because of their unique properties in terms of heat and corrosion resistance, cross-linking and good substrate adhesion. Among all silicon-based materials, silicon dioxide (SiO₂), also known as silica, is probably the best-known due to its further properties in terms of dielectric strength, optical transparency and barrier performance.[29] The actual importance of SiO₂ layers emerges clearly from the widespread range of industrial applications. For example, in the microelectronic field these thin films are used as dielectric layers for electronic devices due to their superior electrical insulation properties or absorption layers in flexible solar cell for efficiency improvements.[24],[25] Alternatively, Si-based thin films could be used for optical amplification and antireflection improvement in the optical field or as barrier layer of polymeric materials typically employed in the packaging industry.[32] Indeed, most of packaging materials used nowadays, such as conventional polymers (PET, PVC, PP) or innovative biodegradable bioplastics, cannot offer a sufficient barrier against oxygen and water vapour thus leading to a reduced shelf-life of food products.[33] In light of this, silicon oxide films deposition gradually become one of the most interesting solutions.

The presence of chemical bonds between silicon and oxygen atoms is the defining characteristic of SiO₂ thin film, however different Si and O atoms arrangements or chemical impurities can induce a wide variety of network structures leading to thin films more or less silica-like. In the particular case of APPs deposition processes, the achievement of pure silica thin films can be considered as one of the greatest challenges of the sector for two main reasons: the use of complex starting precursors with a chemical composition quite far the one of pure silica and the presence of not easily controllable multiple gas-phase fragmentation pathways and surface reactions which could take part in thin films formation and result in unpredictable film composition. Moreover, in case of deposition on thermoplastic-polymers everything is even more complicated by the fact that silica-like coatings are characterized by thermomechanical properties completely different from the substrate. In fact, despite the substrate temperature has a central role in the SiO₂ thin films densification, the stretching of the polymeric substrate and the consequent appearance of cracks in the silica layer (due to a relatively lower coefficient of thermal expansion) could occur, thus hindering their industrial implementation. [34]

As mentioned above, the choice of the precursor plays an important role in the deposition process and, consequently, a quick overview of the most used Si-based precursor is required. Plasma polymerization of SiH₄ in oxygen-based mixtures has been used for many years for the deposition of SiO₂ thin film with low pressure plasmas due to the low concentrations (less than 1%) of Si-H and Si-OH impurities in the deposit and deposition rates completely independent from substrate temperature.[35] However, the possible occurrence of spontaneous combustion events without the need of an external ignition,

makes the use of SiH₄ hazardous in case of LP processes and completely unsuitable for open air processes. Thus, among other monomers, Hexamethyldisiloxane (HMDSO) and Tetraethoxysilane (TEOS) have become important substitutes in both AP and LP processes. Such precursors are characterized by a symmetrical chemical structure, which results in a low enthalpy of vaporization due to weak intermolecular interactions, and by the presence of silicon units already bonded with oxygen atoms.[36] These non-toxic compounds, easily available from commercial sources at a moderate price, are called in general organosilicon precursors due to their organic–inorganic character. Despite HMDSO and TEOS compounds belong to the same family, their differ in terms of chemical structure, stoichiometric ratio and chemical bonds dissociation energy as presented in **Figure 1.1**.

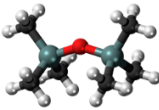
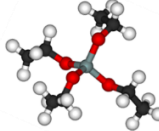
	Formula	Stoichiometry [Si]:[C]:[O]	Dissociation energy [eV]	3D structure
HMDSO	C ₆ H ₁₈ OSi ₂	2:6:1	Si-O → 5.7 Si-C → 3.8	
TEOS	SiC ₈ H ₂₀ O ₄	1:8:4	Si-O → 5.0 C-O → 4.0 C-C → >3.8	

Figure 1.1 –Formula, stoichiometric ratio, dissociation Energies and 3D structure of HMDSO and TEOS molecules

Due to its chemical composition, HMDSO is often adopted for plasma polymerization of coatings with an organic character and chemical structure similar to Polydimethylsiloxane (PDMS), a carbon-based polymer typically used for biomedical application due to its smooth flexible surface without cracks, its hydrophobic behaviour and high biocompatibility.[37] Some results discussed by Morent *et al.* [13] clearly show that the chemical and morphological properties of plasma polymerized HMDSO coatings are strongly affected by the process gas composition and a gradual transition from organic PDMS-like to inorganic SiO₂-like coatings is strongly dependent on the oxygen/air percentage introduced inside the plasma source. The possibility to produce thin films with tailored properties by controlling external parameters, e.g gas composition, has made HMDSO the most popular precursor in case of AP deposition processes. Accordingly, this general interest on HMDSO thin films has also led over the years to the investigation of the most important gas phase mechanisms. In that regard, Sonnenfeld [38] has shown the dominant electron impact reactions involved in the conversion and/or fragmentation of the monomer, as reported in **Figure 1.2**, by using the Gas Chromatography (GC) technique on a filamentary Dielectric Barrier Discharge (DBD) configuration working in air mixture.

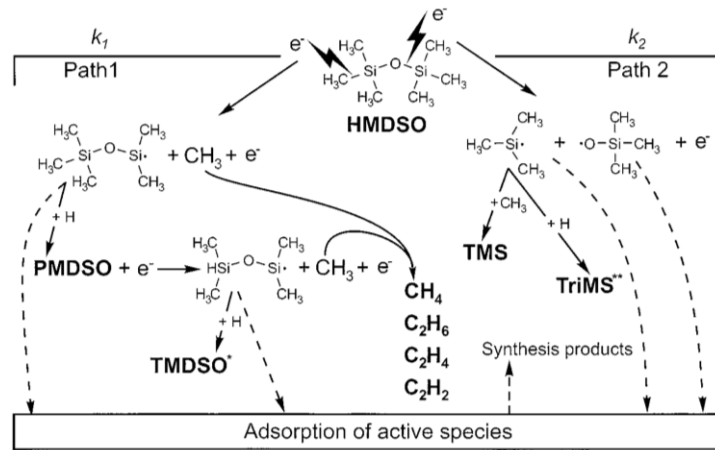


Figure 1.2 – Scheme of predominant gas-phase mechanisms in air/HMDSO plasma detected by GC of exhaust gasses [38]

Moreover, Loffhagen *et al.*[39], in 2017, studied for the first time the most significant gas phase reactions of a DBD in highly diluted HMDSO/Ar mixtures by an analytical model based on the reaction-kinetics model reported by Becker [40] (including 14 Ar species and 114 reactions), extended by the inclusion of reactions between Ar species and HMDSO. The list of collision processes reported in the above-mentioned work is presented in **Figure 1.3**. These large number of publications has thus bridged the knowledge gap between gas-phase mechanisms and thin film properties making further comprehensive study of the process redundant.

Index	Reaction	Rate coefficient
Electron impact ionization		
1	$(\text{CH}_3)_3\text{SiOSi}(\text{CH}_3)_3 + e \rightarrow (\text{CH}_3)_3\text{SiOSi}^+(\text{CH}_3)_2 + \text{CH}_3 + 2e$	$k_{HI}(u_e)$
Electron-ion recombination		
2	$(\text{CH}_3)_3\text{SiOSi}^+(\text{CH}_3)_2 + e \rightarrow \text{Products}$	$3.6 \times 10^{-6} (T_e/300)^{-0.5}$
Ion-molecule reactions		
3	$\text{Ar}^+ + (\text{CH}_3)_3\text{SiOSi}(\text{CH}_3)_3 \rightarrow (\text{CH}_3)_3\text{SiOSi}^+(\text{CH}_3)_2 + \text{CH}_3 + \text{Ar}$	2.0×10^{-9}
4	$\text{Ar}_2^+ + (\text{CH}_3)_3\text{SiOSi}(\text{CH}_3)_3 \rightarrow (\text{CH}_3)_3\text{SiOSi}^+(\text{CH}_3)_2 + \text{CH}_3 + 2\text{Ar}$	1.4×10^{-9}
Penning ionization processes		
5	$\text{Ar}[1s_3] + (\text{CH}_3)_3\text{SiOSi}(\text{CH}_3)_3 \rightarrow (\text{CH}_3)_3\text{SiOSi}^+(\text{CH}_3)_2 + \text{CH}_3 + \text{Ar} + e$	$\alpha_{PI} \times 5.0 \times 10^{-10}$
6	$\text{Ar}[1s_4] + (\text{CH}_3)_3\text{SiOSi}(\text{CH}_3)_3 \rightarrow (\text{CH}_3)_3\text{SiOSi}^+(\text{CH}_3)_2 + \text{CH}_3 + \text{Ar} + e$	$\alpha_{PI} \times 5.0 \times 10^{-10}$
7	$\text{Ar}[1s_5] + (\text{CH}_3)_3\text{SiOSi}(\text{CH}_3)_3 \rightarrow (\text{CH}_3)_3\text{SiOSi}^+(\text{CH}_3)_2 + \text{CH}_3 + \text{Ar} + e$	$\alpha_{PI} \times 5.0 \times 10^{-10}$
8	$\text{Ar}[1s_2] + (\text{CH}_3)_3\text{SiOSi}(\text{CH}_3)_3 \rightarrow (\text{CH}_3)_3\text{SiOSi}^+(\text{CH}_3)_2 + \text{CH}_3 + \text{Ar} + e$	$\alpha_{PI} \times 5.0 \times 10^{-10}$
9	$\text{Ar}[2p] + (\text{CH}_3)_3\text{SiOSi}(\text{CH}_3)_3 \rightarrow (\text{CH}_3)_3\text{SiOSi}^+(\text{CH}_3)_2 + \text{CH}_3 + \text{Ar} + e$	$\alpha_{PI} \times 5.0 \times 10^{-10}$
10	$\text{Ar}[2p'] + (\text{CH}_3)_3\text{SiOSi}(\text{CH}_3)_3 \rightarrow (\text{CH}_3)_3\text{SiOSi}^+(\text{CH}_3)_2 + \text{CH}_3 + \text{Ar} + e$	$\alpha_{PI} \times 5.0 \times 10^{-10}$
11	$\text{Ar}[hl] + (\text{CH}_3)_3\text{SiOSi}(\text{CH}_3)_3 \rightarrow (\text{CH}_3)_3\text{SiOSi}^+(\text{CH}_3)_2 + \text{CH}_3 + \text{Ar} + e$	$\alpha_{PI} \times 5.0 \times 10^{-10}$
Quenching of excited argon species		
12	$\text{Ar}[1s_3] + (\text{CH}_3)_3\text{SiOSi}(\text{CH}_3)_3 \rightarrow (\text{CH}_3)_3\text{Si} + (\text{CH}_3)_3\text{SiO} + \text{Ar}$	$(1 - \alpha_{PI}) \times 5.0 \times 10^{-10}$
13	$\text{Ar}[1s_4] + (\text{CH}_3)_3\text{SiOSi}(\text{CH}_3)_3 \rightarrow (\text{CH}_3)_3\text{Si} + (\text{CH}_3)_3\text{SiO} + \text{Ar}$	$(1 - \alpha_{PI}) \times 5.0 \times 10^{-10}$
14	$\text{Ar}[1s_5] + (\text{CH}_3)_3\text{SiOSi}(\text{CH}_3)_3 \rightarrow (\text{CH}_3)_3\text{Si} + (\text{CH}_3)_3\text{SiO} + \text{Ar}$	$(1 - \alpha_{PI}) \times 5.0 \times 10^{-10}$
15	$\text{Ar}[1s_2] + (\text{CH}_3)_3\text{SiOSi}(\text{CH}_3)_3 \rightarrow (\text{CH}_3)_3\text{Si} + (\text{CH}_3)_3\text{SiO} + \text{Ar}$	$(1 - \alpha_{PI}) \times 5.0 \times 10^{-10}$
16	$\text{Ar}[2p] + (\text{CH}_3)_3\text{SiOSi}(\text{CH}_3)_3 \rightarrow (\text{CH}_3)_3\text{Si} + (\text{CH}_3)_3\text{SiO} + \text{Ar}$	$(1 - \alpha_{PI}) \times 5.0 \times 10^{-10}$
17	$\text{Ar}[2p'] + (\text{CH}_3)_3\text{SiOSi}(\text{CH}_3)_3 \rightarrow (\text{CH}_3)_3\text{Si} + (\text{CH}_3)_3\text{SiO} + \text{Ar}$	$(1 - \alpha_{PI}) \times 5.0 \times 10^{-10}$
18	$\text{Ar}[hl] + (\text{CH}_3)_3\text{SiOSi}(\text{CH}_3)_3 \rightarrow (\text{CH}_3)_3\text{Si} + (\text{CH}_3)_3\text{SiO} + \text{Ar}$	$(1 - \alpha_{PI}) \times 5.0 \times 10^{-10}$
19	$\text{Ar}_2[{}^3\Sigma_u^+, v = 0] + (\text{CH}_3)_3\text{SiOSi}(\text{CH}_3)_3 \rightarrow (\text{CH}_3)_3\text{Si} + (\text{CH}_3)_3\text{SiO} + \text{Ar}$	5.0×10^{-10}
20	$\text{Ar}_2[{}^1\Sigma_u^+, v = 0] + (\text{CH}_3)_3\text{SiOSi}(\text{CH}_3)_3 \rightarrow (\text{CH}_3)_3\text{Si} + (\text{CH}_3)_3\text{SiO} + \text{Ar}$	5.0×10^{-10}
21	$\text{Ar}_2[{}^3\Sigma_u^+, v \gg 0] + (\text{CH}_3)_3\text{SiOSi}(\text{CH}_3)_3 \rightarrow (\text{CH}_3)_3\text{Si} + (\text{CH}_3)_3\text{SiO} + \text{Ar}$	5.0×10^{-10}
22	$\text{Ar}_2[{}^1\Sigma_u^+, v \gg 0] + (\text{CH}_3)_3\text{SiOSi}(\text{CH}_3)_3 \rightarrow (\text{CH}_3)_3\text{Si} + (\text{CH}_3)_3\text{SiO} + \text{Ar}$	5.0×10^{-10}

Figure 1.3 – Atmospheric pressure collision processes between Ar species and HMDSO molecules [39]

By contrast, very little work has been done to analyse the main fragmentation pathways resulting from electron or Ar metastable impact on TEOS molecules at atmospheric pressure, despite being characterised by the possibility of depositing silica-like coatings by avoiding the use of further oxygen-based gasses and by a chemical structure very close to SiO₂, opening interesting perspectives in terms of energetic and economic savings.[41] The state of the art on key achievements and scientific/technologic barriers of plasma-assisted TEOS deposition processes is summarized in the following sections with the aim of underlining the necessity of new scientific discoveries for an adequate control and an in depth understanding of the process as provided in the past for the HMDSO case.

1.3 Scientific background on plasma polymerized TEOS thin films

The scientific literature concerning plasma polymerized TEOS thin films is clearly divided in two main different branches. On the one hand, the study of low pressure plasmas for silica coating deposition, primarily aimed at evaluating the main gas-phase reactions involved in the process; while, on the other hand, a detailed analysis of chemical and physical properties of the silica-like thin films obtained by atmospheric pressure processes mainly focused on the development of new configuration suitable for industrial on-line processes. In the first case, the thin film characteristics are usually good in terms of inorganic content, water resistance and absence of defects, even if the insufficient deposition rates associated to a good process control could result as an effective barrier for the industrial implementation.[42] In light of this, the plasma community has focused its efforts on the study of the gas-phase mechanism by using different kind of diagnostic techniques in order to define a clear correlation between operating condition and coating performances and understand how speed up the process without affecting the thin films quality. In case of atmospheric plasmas, the scientific approach is completely different. Indeed, the deposition of thin films with good chemical and morphological properties is not an easy task and the research of TEOS thin films with surface features competitive with those gained under LP conditions is ongoing. Considering this, almost all the publications on this topic are limited to presenting surface characterization results by varying operating conditions or device configurations adopted without any consideration on the gas-phase physics and chemistry behind the deposition process.[43], [44]. For reasons of clarity, some of the major discoveries in the field of SiO₂ thin films obtained by means of atmospheric plasma are described in section 1.3.1; an overview of low pressure processes for SiO₂ thin films deposition by using TEOS as precursor is presented in section 1.3.2.

1.3.1 Overview on APPs for SiO₂ thin films deposition using TEOS as precursor

Although the use of thermal plasmas discharges for TEOS thin films deposition has expanded enormously since the late 1970s for integrated circuit manufacturing by thermal decomposition (CVD) of TEOS at temperatures higher than 600 °C, the first papers and patents concerning the deposition of TEOS at lower substrate temperature (< 400 °C) in atmospheric pressure conditions have been published in the first half of the nineties thanks to the development of capacitive radiofrequency discharges.[45] On this subject, Babayan [46] has presented for the first time a plasma jet configuration operating in O₂/He mixtures suitable for the deposition of SiO₂ thin films with operating temperature included between 115 - 350 °C. The author proved that the features of thin films deposited at 350 °C, which

exhibit infrared peaks at 450, 800 and 1080 cm^{-1} due to the rocking, bending and stretching modes of siloxane linkages, are comparable to those of thermally grown SiO_2 films, while absorption peaks at 930 and 3400 cm^{-1} , caused by bending and stretching vibrations of hydroxyl groups, appear only in case of low temperature (115°C) deposit (as shown in **Figure 1.4.**) by revealing the presence of undesirable water molecules onto the thin film surface.

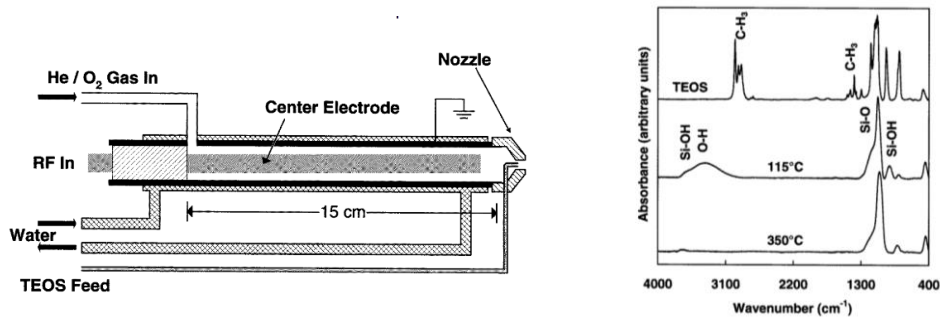


Figure 1.4 – Plasma source cross-sectional view (left) and FTIR spectra (right) of: pure TEOS thin film deposited at 115° and thin film deposited at 350°C [46]

Despite the excellent results achieved in terms of inorganic content, the use of such plasmas on thermo-sensitive materials was still forbidden due to the high process temperatures. In order to overcome this problem, in 1995, Sawada [47] proposed a new plasma technology, called atmospheric pressure glow (APG) discharge, for the synthesis of plasma polymerized TEOS thin films in He or O_2/He mixtures by using an AC generator. Interestingly, in case of pure He plasma, morphological results confirmed a surface smooth and free from defects at low temperature ($<100^\circ\text{C}$) while FTIR spectra revealed the presence of organic bonds by means of C=O stretching and Si-C stretching absorption peaks at 1730 cm^{-1} and 880 cm^{-1} respectively (**Figure 1.5**). This organic content, confirmed by XPS analyses (C=33%, Si= 29%, O= 38%), completely disappear with the addition of a low percentage of oxygen (C=0%, Si= 36%, O= 64%) leaving space to broad absorption peaks caused by OH groups as shown in the Babayan case. Of interest is also the fact that the Sawada's work reports also some preliminary consideration about gas-phase processes hard to find in case of APPs. However, the result observed by optical emission spectroscopy (OES) were used only for a comparison with LP studies in terms of emitting species produced thus not allowing to draw any consideration on AP gas-phase processes.

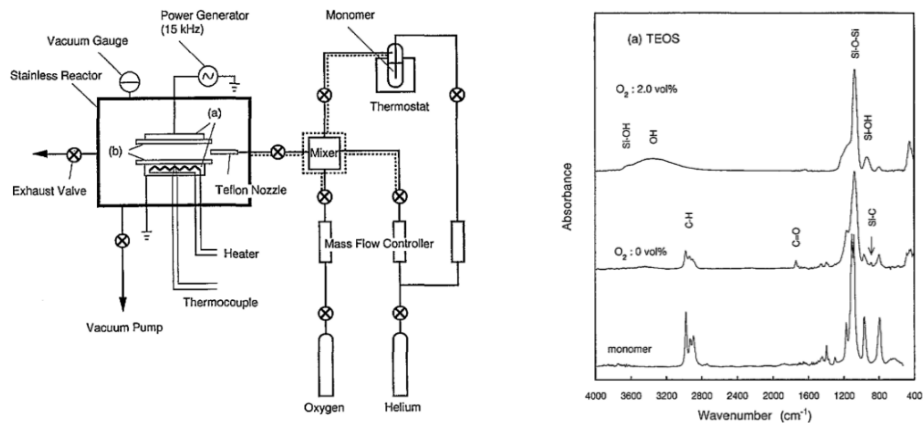


Figure 1.5 – Experimental set-up (left) and FTIR spectra under different TEOS/ O_2 mixture (right) [47]

After that, other configurations were studied in the early 2000's with the aim of improving the industrial applicability and performances of SiO₂ thin films. In particular, several research groups have shown the use of DBD configurations with dynamic electrode arrangement for the deposition of thin films on polymeric sheets. As an example, the influence of plasma parameters such as energy released for each single pulse, position of the sample and deposition rate were investigated by T. Opaliska et al. [48]; while coating thickness, surface energy and grown rate were studied in details by B. Twomey [49] as a function of the He/O₂ flow rates. In 2002, a similar configuration was used by Sonnenfeld [38] to study the influence of the power applied (energy per precursor molecule) on thin films surface properties. The DBD plasma source, presented in **Figure 1.6**, operates in a dynamic mode in Ar/TEOS or Ar/O₂/TEOS admixtures and is driven by a sinusoidal voltage power supply with a fixed frequency of 6.6 kHz. From XPS data it was found that the amount of carbon content (C=43.7%, Si= 11%, O= 45.3%) in case of Ar/TEOS plasma is reduced with respect to the TEOS stoichiometric ratio; but, also in this case, the organic content seems significantly decreased in deposits achieved by using Ar/O₂ mixture as gas flow. By comparison with the previous cases, it is clear that the use of this “new” dynamic plasma configurations, typically working in Argon, makes the deposition of silica-like coating even more difficult due to the lack of high process/substrate temperature or long TEOS residence times inside the active deposition zone. Moreover, it is worth mentioning that, in order to study the gas-phase chemical conversion of TEOS during the deposition process, the exhaust gas of the plasma device was analysed by means of Gas Chromatography (GC). Ethanol (C₂H₅OH) was found to be the dominant stable product of the gas phase process probably produced by the recombination of -OC₂H₅ fragments generated after the Si-O bond breaking due to electron impact reaction with TEOS molecules; while, as shown in **Figure 1.6**, all the other compounds detected (TE₁–TE₅) were not identified. Also, in this case the gas phase study is not exhaustive and cannot be used to draw concrete conclusions regarding the dominant fragmentation pathways of the process in contrast to the HMDSO proposal performed by the same authors (presented in **Figure 1.2**). However, the possibility to use plasma devices easily implementable in production lines paved the way for a new generation of atmospheric plasma prototypes over the following years.

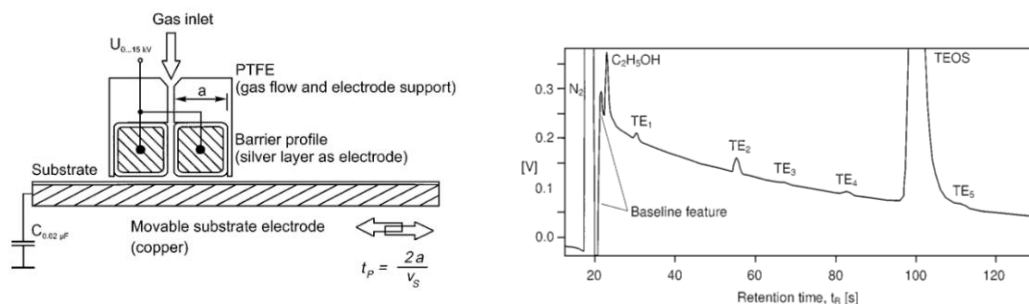


Figure 1.6 – “dynamic” DBD configuration (left) and GC results obtained in Ar/TEOS mixture (right) [38]

Indeed, in 2010, the research group headed by M.C.M van de Sanden [39],[48] reported for the first time the deposition of SiO₂-like thin films on flexible large-area polymeric substrates, e.g polyethylene terephthalate (PET) and polyethylene-2,6 naphthalate (PEN) sheets, by using an AP uniform glow-like DBD technology. The presented device allows the deposition of uniform inorganic coatings in Ar/N₂/O₂ mixtures thanks to the

implementation of an electronic stabilization unit (Matching Network) between the HV generator and the plasma device. The schematic picture of the roll-to-roll reactor is shown in **Figure 1.7**. XPS and AFM results obtained using 10 slm of N₂, 1 slm of Ar, 0.2 slm of O₂ and 150 ppm of TEOS as process gasses have shown a very low carbon contamination ($1.7 \pm 0.1\%$) and a smooth morphology with a root mean square (rms) value insignificantly altered respect the bare polymer substrate. Furthermore, the produced single layers presented excellent gas barrier performances in terms of oxygen transmission rate (OTR: $<5 \times 10^{-3} \text{ cm}^3 \text{ m}^2 \text{ day}^{-1}$) and water vapour transmission rate (WVTR: $<5 \times 10^{-3} \text{ g m}^{-2} \text{ day}^{-1}$).[41] Five years later, the influence of two key parameters, namely dynamic deposition rate and substrate temperature was investigated by preserving the same plasma configuration in order to define the minimum energy value required for the deposition of good performing silica-like films.[51] 20 slm of N₂, 1 slm of Ar and a fixed TEOS/O₂ ratio of 4.5×10^{-3} slm were used for this further step and, also in this case, almost totally inorganic (C $<0.3\%$) smooth (rms = $1.7 \pm 0.1 \text{ nm}$ for $2 \times 2 \mu\text{m}$ of characterization area) thin films were deposited for the whole studied range of operating conditions. However, a minimum specific energy equal to 1.1 keV/molecule, substantially higher than TEOS chemical bonds dissociation energy ($\sim 4\text{-}5 \text{ eV}$), was determined to be crucial for the formation of dense inorganic silica-like layer by suggesting the presence of additional surface or gas-phase reactions involved in the process not merely for the scission of the hydrocarbon groups, but mostly for the densification of the deposited layer. In the years following 2016, supplementary informations on this specific deposition process were provided by F.M. Elam [52] and Y. Liu[53]. In particular, the first paper showed the possibility to use a bilayer architecture to prevent the formation of microdefects on the film surface which could appear at extreme process conditions in terms of input energies per precursor molecule; while the second paper reported a gas-phase analysis of stable molecules in the gas effluent by using a high-resolution Fourier-transform infrared spectrometer. Such measurements revealed high rates of CO_x species produced due to the precursor dissociation or PEN substrate etching in case of precursor flow lower than 100 ppm (etching-deposition regime) and highlight formic acid (HCOOH), formed through the plasma synthesis of CO_x, as best sensitive indicator for etching rates.

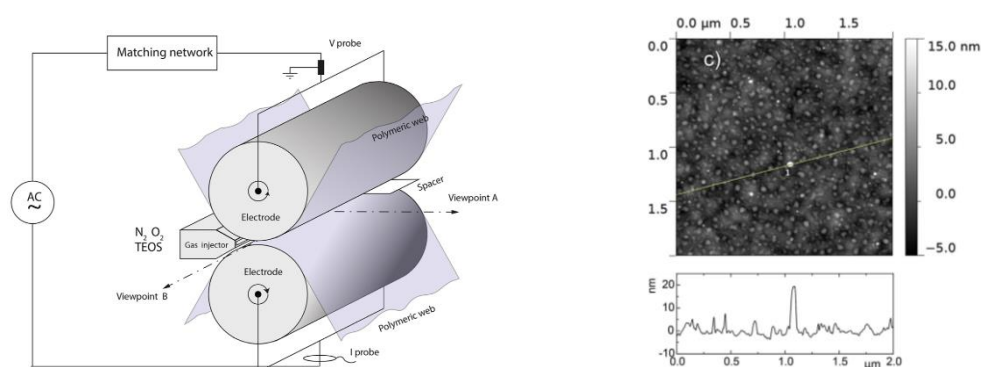


Figure 1.7 – “roll-to-roll” DBD configuration (left) and AFM results obtained in Ar /N₂ /O₂ /TEOS mixture (right) [51]

This branch of activity was almost totally supported by the industrial partnership with FUJIFILM Manufacturing Europe BV (the largest manufacturing and research organisation of FUJIFILM Co. outside Japan) that, on the basis of the scientific research presented above, developed the innovative “Green atmospheric glow plasma” prototype, shown in

Figure 1.8, for the deposition of silica-like thin films on PV-cells and flexible electronics devices in order to prevent moisture penetration and consequently increase the products lifespan.

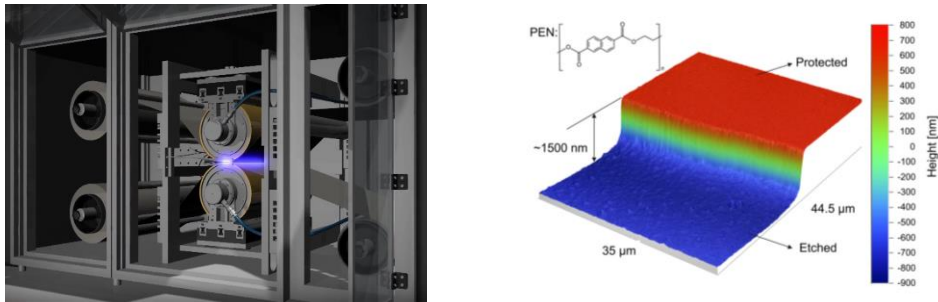


Figure 1.8 – “Green atmospheric glow plasma” FUJIFILM prototype (left) and interferometric microscopy results of PEN foils treated in air-based mixtures (right) [53]

Also in this case, despite the significative reduction in terms of electronic device production costs and the greatest results achieved from the thin film properties point of view, the main gas-phase mechanisms and dominant TEOS fragmentation pathways involved in the process were never been studied in detail.

As anticipated in the introductory part, this approach is actually the common thread between all paper published on this topic; accordingly, it is clear that the plasma scientific community has to explore innovative ways for a further process optimization. Although the result obtained up to now are even better than a single SiO₂ layer deposited at low pressure conditions, a deeper understanding of the gas-phase deposition mechanisms by means of different spectroscopy techniques as well as the establishment of plasma physical and chemical parameters which have an influence on coating properties could open the way for real-time control systems implementable on production lines, thus increasing the industrial diffusion of APP device for thin film deposition.

1.3.2 Overview on LPPs for SiO₂ thin films deposition using TEOS as precursor

In the first half of the nineties, simultaneously to the development of capacitive radiofrequency discharges for TEOS thin film deposition at atmospheric pressure, several research groups focused their studies on the optimization of pre-existing low-pressure processes. Over these years, such well-established technology was used for the first time for the deposition on plastics and other thermosensitive materials, with and without oxygen addition, at temperatures lower than 100°C. Consequently, new diagnostic techniques combined with structural analysis of deposits were developed to qualitatively explain innovative experimental findings.

For example, in 1992, F. Fracassi *et al.* [2] presented for the first time a proposal of the gas-phase reaction pattern behind low pressure plasmas in TEOS/O₂ mixture with the aim of defining the dominant mechanism involved in the thin films composition control. By the use of two in-situ diagnostic tools, Mass-spectrometric (MS) analysis and Optical Emission Spectroscopy (OES), the authors delineated two different kinds of reactive species which occurs simultaneously from electron collision with TEOS molecules: silicon-based species (bonded with carbon and oxygen atoms) and organic radicals (hydrocarbon fragments). On

the other hand, the results obtained showed also the active role of oxygen atoms in increasing TEOS gas-phase conversion pathways and removing the thin film organic content by means of gas-surface reactions. The main reaction mechanisms, validated also in terms of surface features by XPS and FTIR results, are reported in **Figure 1.9**. It is important to highlight that in this case OES was used for the detection of reactive emitting species (H and O atoms, CH and OH radicals or CO molecules) and for actinometric measurements of O concentration as function of O₂/TEOS ratio (Figure 1.9), while MS was used for the definition of the conversion rate of TEOS molecules by detection of exhaust-gasses stable species. Despite the use of OES was not a novelty for TEOS deposition processes, this paper contains the first proposal of a poly-diagnostic approach.

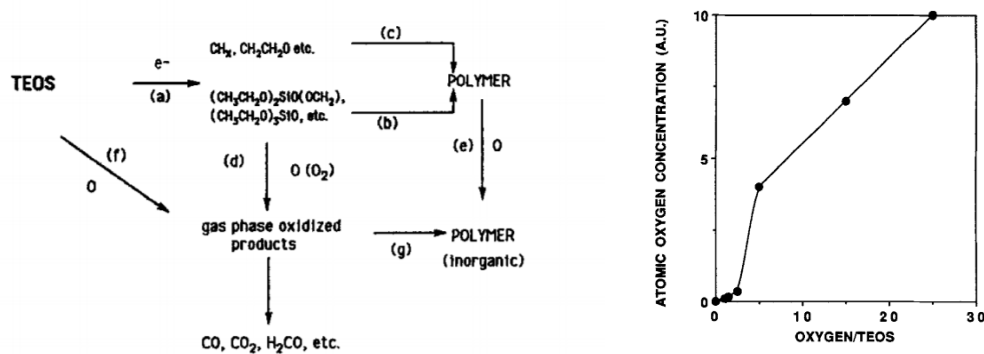


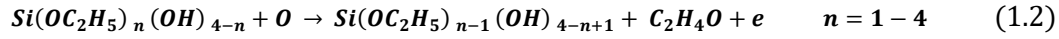
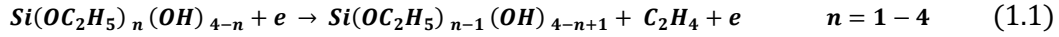
Figure 1.9 – Gas-phase reaction pattern (left) and actinometric measurements of O concentration as function of O₂/TEOS ratio [2]

An OES study of the LP TEOS deposition process was performed also by K. Aumaille *et al.*[36] in order to correlate the structure and properties of the deposited thin films with the plasma gas composition by varying the amount of precursor content in O₂/TEOS plasmas. Also in this case, the results detected by several ex situ thin films diagnostics combined with emission spectra show that O atoms are not necessary for the deposition of organic film, due to the efficient dissociation of TEOS molecules by electron impact, but are strictly required to obtain SiO₂-like films. This paper clearly underlines that the use of a single gas-phase diagnostic techniques is not enough to identify the nature of the fragments responsible for the film's deposition and the simultaneous use of other in situ diagnostics is necessary.

To confirm this, in 2002, A. Granier [54] showed a detailed analysis of the excited species produced during the process by recording low and high resolution OES spectra. Also in this case, despite the high resolution spectra (acquired by a Fourier transform spectrometer) were shown to be essential to prove the presence of the weakly emissive species invisible by low resolution spectra (0.3 nm), the employment of a single diagnostic techniques is not enough for a full understanding of the gas-phase mechanisms. Anyway, the excited species detected in this paper, can be use as partial reference data for the interpretation of the optical emission spectra presented in this dissertation.

Recently, also M. Abbasi-Firouzjah *et al.* [55] use OES to monitor the low pressure deposition process performed in TEOS/O₂/Ar mixtures and investigate the oxygen role. Their gas-phase study is almost totally based on the Monte-Carlo simulation carried out by Stout and Kushner [56] in 1993 for SiO₂ thin film deposition in LP conditions. Indeed, according to Kushner model, TEOS can be dissociated both by electron impact and oxidation mechanisms in order to generate a thin film with performances very similar to

that of pure silica. The most significant reaction pathways proposed consist in the two gas phase reactions reported in **Equation 1.1** and **1.2** and surface reactions which have an active role in the removal of the thin film organic content and formation of the Si-O-Si band as claimed by F. Fracassi.



In particular, looking at the pure TEOS spectrum obtained by OES, M. Abbasi-Firouzjeh assumes that the H_α excitation line is a consequence of the TEOS molecule dissociation and confirms the mechanism proposed in Eq.1.2 by observing that the intensity of the H_α excitation line increase with the increasing of the oxygen content.

This short overview of the most significant papers on low pressure plasmas for silica-like films deposition by using TEOS as precursor is mostly aimed at describing some diagnostic tools typically used for the gas-phase plasma deposition study rather than presenting surface thin film properties achievable by conventional LP processes. As confirmed by the discussion above, despite the use of diagnostic technique such as OES is very widespread, it is difficult to find exhaustive gas-phase characterization of the deposition process also in case of low-pressure plasmas. This almost total absence of reference data makes the study of this precursor even more attractive.

1.4 Outline/scope of the thesis

In the present thesis a poly-diagnostic study of an APP jet specifically designed for the deposition of coatings by using an Ar/Tetraethyl orthosilicate (TEOS) mixture is undertaken. The graphical abstract of the dissertation is shown in **Figure 1.10**. In general, the main aim of the work presented is a fully comprehensive study of the process starting from the surface characterization of the deposits to an in-depth analysis of the dominant gas-phase mechanisms involved in the process by considering both excited and ground state species produced. To reach this goal, the dissertation is structured in the following way:

- In **chapter 2**, a detailed description of the experimental set-up and the operating conditions, investigated in this work for the deposition of Si-based thin films, is given. Afterward, a short overview on different kind of ex-situ techniques employed for a complete thin films surface characterization is provided. The precursor gas flow and the applied power effect of the on the thin films chemical properties is studied by FTIR technique, while the effect of process temperature and power on the structural properties of plasma polymerized TEOS films is investigated by XPS, AFM and SEM analyses. The results discussed in this chapter highlight the achievement of smooth, almost inorganic and free from defects thin films under the lowest operating conditions (6 kV-12 kHz) while thermally damaged thin films are detected under higher power conditions.
- Even if the density of excited species is much lower than the density of species in the ground state, the study of gas-phase mechanisms involving these emitting species is an

important first step for an in-depth understanding of the deposition process. In this regard, a detailed study of both the discharge physics and the chemical gas-phase mechanisms involved in the deposition process is performed by imaging, optical emission spectroscopy and Rayleigh scattering techniques in **chapter 3**. An overview of the most important emitting species detected by Optical Emission spectroscopy under the highest operating conditions is provided. Moreover, due to the key role of gas temperature on the gas-phase reactions kinetics and thin film properties, the influence of TEOS admixture on gas temperature is studied by OES and Rayleigh scattering techniques. The predominant excited species production mechanisms are then revealed by combining time-resolved electron density results and spatial-temporal behaviours Ar, O, N₂, OH and CH radicals. Special attention is paid to the main formation pathways of excited CH radicals in order to shed the light on the role of Ar^m and electrons on TEOS fragmentation under atmospheric pressure conditions.

- The lack of clarity behind gas-phase processes involving non emitting species is actually one of the main barriers preventing a good process understanding. In **chapter 4**, the effect of TEOS addition on CH, OH radicals and O atoms generation mechanisms under atmospheric pressure conditions is investigated for the first time by spatially resolved laser-induced fluorescence (LIF) and two-photon laser induced fluorescence (TALIF) techniques respectively. The ground state species spatial distribution is studied as a function of the carrier gas flow injected and the voltage applied during the plasma treatment by preserving the same operating conditions previously employed for thin film deposition (chapter 2). Then, the dominant ground state recombination processes in presence of a high content of hydrocarbon fragments are also discussed. In addition, the physics behind ground state particles generation is combined to the predominant excited state production mechanisms defined in chapter 3.
- The general conclusions are draw in **chapter 5** with a particular focus on possible next steps required for the current work finalisation and the development of innovative computational models.

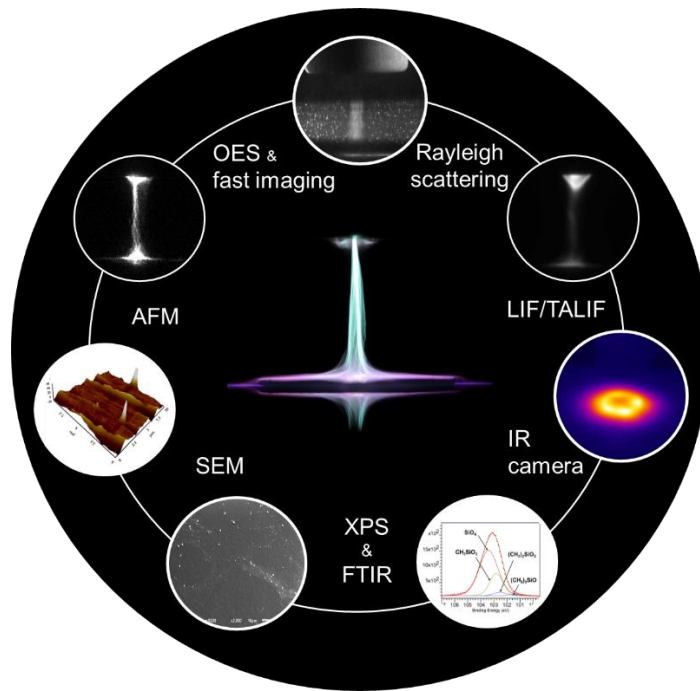


Figure 1.10 – Graphical abstract summarizing the poly-diagnostic approach used in the work

1.5 Publications

1.5.1 Publications in international journals

- I. **F. Barletta**, A. Liguori, Ch. Leys, V. Colombo, M. Gherardi and A. Nikiforov, “*Novel method for NH-rich coatings engineering by means of aerosol assisted atmospheric pressure plasma deposition*”, *Materials Letters*, 214, 76–79, 2018.
- II. **F. Barletta**, Ch. Leys, V. Colombo, M. Gherardi, N. Britun, R. Snyders and A. Nikiforov, “*Insight in plasma-assisted polymerization at atmospheric pressure by spectroscopic diagnostic*”, under review in *Plasma Processes and Polymers*.
- III. E. Simoncelli, J. Schulpen, **F. Barletta**, R. Laurita, V. Colombo, A. Nikiforov and M. Gherardi, “*UV-VIS optical spectroscopy investigation on the kinetics of long-lived RONS produced by a surface DBD plasma source*” *Plasma Sources Science and Technology*, 28, 095015 (13 pp), 2019.

1.5.2 Publications in international conferences

- I. **F. Barletta et al.**, “*New research tools for the field of cold atmospheric plasma applications*” poster presentation at the National Congress of the Italian Society of Biomaterials, Milano, Italy 24-26 May 2017.
- II. **F. Barletta et al.**, “*Cold atmospheric pressure plasma for the crosslinking of*

electrospun gelatin mats and gelatin films containing drugs” poster presentation at the National Congress of the Italian Society of Biomaterials, Milano, Italy 24-26 May 2017.

- III. **F. Barletta et al.**, “*Deposition of polymeric films and co-deposition of nanocomposite coatings by means of a cold atmospheric pressure plasma jet*” invited presentation at 17th International Conference on Plasma Physics and Application, Bucharest, Romania 15-20 June 2017.
- IV. **F. Barletta et al.**, “*Cold atmospheric pressure plasma for the deposition of polymeric films and the co-deposition of nanocomposite coatings*” oral presentation at 23rd International Symposium on Plasma Chemistry, Montréal, Canada 30 July – 4 August 2017.
- V. **F. Barletta et al.**, “*Deposition of polymeric films and co-deposition of nanocomposite coatings by means of a cold atmospheric pressure plasma jet*” oral presentation at 28th Annual Meeting of the European Society for Biomaterials, Athens, Greece 4-8 September 2017.
- VI. **F. Barletta et al.**, “*Correlation between the concentration of reactive species produced by a Surface Barrier Discharge plasma source and its antimicrobial effects*” poster presentation at the international school on low temperature plasma physics: basics and applications, Bad Honnef, Germany 7-12 October 2017.
- VII. **F. Barletta et al.**, “*Correlation between the concentration of reactive species produced by a Surface Barrier Discharge plasma source and its antimicrobial effects*” poster presentation at 7th International Conference on Plasma Medicine, Philadelphia, 17-22 June 2018.
- VIII. **F. Barletta et al.**, “*Novel method for NH-rich coatings engineering by means of aerosol assisted atmospheric pressure plasma deposition*” poster presentation at 29th Annual Meeting of the European Society for Biomaterials, Maastricht, 9-13 September 2018.
- IX. **F. Barletta et al.**, “*Single-step deposition of surface chemical gradients with a corona jet at atmospheric pressure*” poster presentation at 24th International Symposium on Plasma Chemistry, Naples, Italy 9-14 June 2019.
- X. **F. Barletta et al.**, “*UV-VIS optical spectroscopy investigation on the kinetics of long-lived RONS produced by a surface DBD plasma source*” oral presentation at ISPC24, Naples, Italy, 9-14 June 2019.
- XI. **F. Barletta et al.**, “*On the Versatility of Atmospheric Non-equilibrium Plasmas: Material Synthesis, Packaging Sanitation and Oncological Applications*” invited presentation at 66th American Vacuum Society International Symposium & Exhibition, Columbus, Ohio, US, 20-25 October 2019.

1.6 References

- [1] J. Luque, W. Juchmann, and J. B. Jeffries, “Absolute concentration measurements of CH radicals in a diamond-depositing dc-arcjet reactor,” *Appl. Opt.*, vol. 36, no. 15, p. 3261, 1997.
- [2] F. Fracassi, R. D’Agostino, and P. Favia, “Plasma-Enhanced Chemical Vapor Deposition of Organosilicon thin Films from Tetraethoxysilane-Oxygen Feeds,” *J. Electrochem. Soc.*, vol. 139, no. 9, pp. 2636–2644, 1992.
- [3] D. Hegemann, B. Nisol, S. Watson, and M. R. Wertheimer, “Energy Conversion Efficiency in Plasma Polymerization – A Comparison of Low- and Atmospheric-Pressure Processes,” *Plasma Process. Polym.*, vol. 13, no. 8, pp. 834–842, 2016.
- [4] J. Luque, M. Kraus, A. Wokaun, K. Haffner, U. Kogelschatz, and B. Eliasson, “Gas temperature measurement in CH₄/CO₂ dielectric-barrier discharges by optical emission spectroscopy,” *J. Appl. Phys.*, vol. 93, no. 8, pp. 4432–4438, 2003.
- [5] C. Tendero, C. Tixier, P. Tristant, J. Desmaison, and P. Leprince, “Atmospheric pressure plasmas: A review,” *Spectrochimica Acta - Part B Atomic Spectroscopy*, vol. 61, no. 1, pp. 2–30, 2006.
- [6] D. Hegemann, B. Nisol, S. Watson, and M. R. Wertheimer, “Energy Conversion Efficiency in Low- and Atmospheric-Pressure Plasma Polymerization Processes, Part II: HMDSO,” *Plasma Chem. Plasma Process.*, vol. 37, no. 1, pp. 257–271, 2017.
- [7] S. E. Alexandrov and M. L. Hitchman, “Chemical vapor deposition enhanced by atmospheric pressure non-thermal non-equilibrium plasmas,” *Chemical Vapor Deposition*, vol. 11, no. 11–12, pp. 457–468, 2005.
- [8] D. Merche, N. Vandecasteele, and F. Reniers, “Atmospheric plasmas for thin film deposition: A critical review,” *Thin Solid Films*, vol. 520, no. 13, Elsevier B.V., pp. 4219–4236, 2012.
- [9] Y. Liou, A. Inspektor, R. Weimer, D. Knight, and R. Messier, “The effect of oxygen in diamond deposition by microwave plasma enhanced chemical vapor deposition,” *J. Mater. Res.*, vol. 5, no. 11, pp. 2305–2312, 1990.
- [10] F. Massines, N. Gherardi, A. Fornelli, and S. Martin, “Atmospheric pressure plasma deposition of thin films by Townsend dielectric barrier discharge,” *Surf. Coatings Technol.*, vol. 200, no. 5–6, pp. 1855–1861, 2005.
- [11] J. Albaugh, C. O’Sullivan, and L. O’Neill, “Controlling deposition rates in an atmospheric pressure plasma system,” *Surf. coatings Technol.*, vol. 203, no. 5–7, pp. 844–847, 2008.
- [12] J. Schäfer, R. Foest, A. Quade, A. Ohl, and K. D. Weltmann, “Local deposition of SiO_x plasma polymer films by a miniaturized atmospheric pressure plasma jet (APPJ),” *J. Phys. D. Appl. Phys.*, vol. 41, no. 19, p. 194010, 2008.
- [13] R. Morent, N. De Geyter, S. Van Vlierberghe, P. Dubruel, C. Leys, and E. Schacht, “Organic-inorganic behaviour of HMDSO films plasma-polymerized at atmospheric pressure,” *Surf. Coatings Technol.*, vol. 203, no. 10–11, pp. 1366–1372, 2009.
- [14] C. P. Klages, A. K. Czerny, J. Philipp, M. M. Becker, and D. Loffhagen, “DBD-based plasma polymerization from monomer-argon mixtures: Analytical model of monomer reactions with excited argon species,” *Plasma Process. Polym.*, vol. 14, no. 12, 2017.
- [15] D. Thiry, S. Konstantinidis, J. Cornil, and R. Snyders, “Plasma diagnostics for the low-pressure plasma polymerization process: A critical review,” *Thin Solid Films*,

- vol. 606, no. June 2018. Elsevier B.V., pp. 19–44, 2016.
- [16] M. J. Shenton and G. C. Stevens, “Surface modification of polymer surfaces: atmospheric plasma versus vacuum plasma treatments,” *J. Phys. D: Appl. Phys.*, vol. 34, no. 18, p. 2761, 2001.
- [17] X. Zhu, F. Arefi-Khonsari, C. Petit-Etienne, and M. Tatoulian, “Open air deposition of SiO₂ films by an atmospheric pressure line-shaped plasma,” *Plasma Process. Polym.*, vol. 2, no. 5, pp. 407–413, 2005.
- [18] F. Massines, N. Gherardi, A. Fornelli, and S. Martin, “Atmospheric pressure plasma deposition of thin films by Townsend dielectric barrier discharge,” *Surf. Coatings Technol.*, vol. 200, no. 5–6, pp. 1855–1861, 2005.
- [19] W. Van Gaens and A. Bogaerts, “Erratum: Kinetic modelling for an atmospheric pressure argon plasma jet in humid air (J. Phys. D: Appl. Phys. 46 (2013) 275201),” *Journal of Physics D: Applied Physics*, vol. 47, no. 7, 2014.
- [20] H. Biederman, *Plasma polymer films*. World Scientific, 2004.
- [21] M. Moreau, N. Orange, and M. G. J. Feuilleley, “Non-thermal plasma technologies: new tools for bio-decontamination,” *Biotechnol. Adv.*, vol. 26, no. 6, pp. 610–617, 2008.
- [22] J. Petersen, J. Bardon, A. Dinia, D. Ruch, and N. Gherardi, “Organosilicon coatings deposited in atmospheric pressure townsend discharge for gas barrier purpose: Effect of substrate temperature on structure and properties,” *ACS Appl. Mater. Interfaces*, vol. 4, no. 11, pp. 5872–5882, 2012.
- [23] S. Asadollahi, J. Profili, M. Farzaneh, and L. Stafford, “Development of organosilicon-based superhydrophobic coatings through atmospheric pressure plasma polymerization of HMDSO in nitrogen plasma,” *Materials (Basel)*, vol. 12, no. 2, p. 219, 2019.
- [24] J. Schäfer, R. Foest, A. Quade, A. Ohl, J. Meichsner, and K. D. Weltmann, “Carbon-free SiO_x films deposited from octamethylcyclotetrasiloxane (OMCTS) by an atmospheric pressure plasma jet (APPJ),” *Eur. Phys. J. D*, vol. 54, no. 2, pp. 211–217, 2009.
- [25] F. Massines, C. Sarra-Bournet, F. Fanelli, N. Naudé, and N. Gherardi, “Atmospheric pressure low temperature direct plasma technology: Status and challenges for thin film deposition,” *Plasma Processes and Polymers*, vol. 9, no. 11–12, pp. 1041–1073, 2012.
- [26] R. Morent *et al.*, “Plasma-Polymerization of HMDSO Using an Atmospheric Pressure Dielectric Barrier Discharge,” *Plasma Process. Polym.*, vol. 6, no. S1, pp. S537–S542, 2009.
- [27] S. Starostine, E. Aldea, H. de Vries, M. Creatore, and M. C. M. van de Sanden, “Atmospheric pressure barrier discharge deposition of silica-like films on polymeric substrates,” *Plasma Process. Polym.*, vol. 4, no. SUPPL.1, pp. 440–444, 2007.
- [28] H. Caquineau, I. Enache, N. Gherardi, N. Naudé, and F. Massines, “Influence of gas flow dynamics on discharge stability and on the uniformity of atmospheric pressure PECVD thin film,” *J. Phys. D: Appl. Phys.*, vol. 42, no. 12, 2009.
- [29] Y. C. Ke and P. Stroeve, *Polymer-layered silicate and silica nanocomposites*. Elsevier, 2005.
- [30] J. Schmidt, M. Kerr, and A. Cuevas, “Surface passivation of silicon solar cells using plasma-enhanced chemical-vapour-deposited SiN films and thin thermal SiO₂/plasma SiN stacks,” *Semicond. Sci. Technol.*, vol. 16, no. 3, p. 164, 2001.
- [31] F. Crisostomo *et al.*, “Experimental testing of SiN_x/SiO₂ thin film filters for a

- concentrating solar hybrid PV/T collector,” *Renew. Energy*, vol. 72, pp. 79–87, 2014.
- [32] V. Siracusa, “Food packaging permeability behaviour: A report,” *Int. J. Polym. Sci.*, vol. 2012, no. i, 2012.
- [33] Y. Leterrier, “Durability of nanosized oxygen-barrier coatings on polymers,” *Progress in Materials Science*, vol. 48, no. 1. pp. 1–55, 2003.
- [34] G. Carlotti, L. Doucet, and M. Dupeux, “Comparative study of the elastic properties of silicate glass films grown by plasma enhanced chemical vapor deposition,” *J. Vac. Sci. Technol. B Microelectron. Nanom. Struct. Process. Meas. Phenom.*, vol. 14, no. 6, pp. 3460–3464, 1996.
- [35] H. Del Puppo, T. Sindzingre, L. Peccoud, and J. Desmaison, “Downstream microwave plasma enhanced chemical vapour deposition of SiO₂ using O₂/SiH₄ and N₂O/SiH₄ mixtures,” *Le J. Phys. IV*, vol. 2, no. C2, pp. C2–421, 1991.
- [36] K. Aumaille, C. Vallée, A. Granier, A. Goullet, F. Gaboriau, and G. Turban, “A comparative study of oxygen/organosilicon plasmas and thin SiO_xC_yH_z films deposited in a helicon reactor,” *Thin Solid Films*, vol. 359, no. 2, pp. 188–196, 2000.
- [37] F. Benitez, E. Martinez, M. Galan, J. Serrat, and J. Esteve, “Mechanical properties of plasma deposited polymer coatings,” *Surf. Coatings Technol.*, vol. 125, no. 1–3, pp. 383–387, 2000.
- [38] A. Sonnenfeld and J. F. B. and R. H. T. M. Tun, L. Zajíčková, K. V. Kozlov, H.-E. Wagner, “Deposition Process Based on Organosilicon Precursors in Dielectric Barrier Discharges at Atmospheric Pressure—A Comparison,” *Plasmas Polym.*, vol. 6, no. 4, pp. 237–266, 2001.
- [39] D. Loffhagen, M. M. Becker, A. K. Czerny, J. Philipp, and C. P. Klages, “Impact of hexamethyldisiloxane admixtures on the discharge characteristics of a dielectric barrier discharge in argon for thin film deposition,” *Contrib. to Plasma Phys.*, vol. 58, no. 5, pp. 337–352, 2018.
- [40] M. M. Becker, T. Hoder, R. Brandenburg, and D. Loffhagen, “Analysis of microdischarges in asymmetric dielectric barrier discharges in argon,” *J. Phys. D. Appl. Phys.*, vol. 46, no. 35, 2013.
- [41] P. A. Premkumar *et al.*, “Smooth and self-similar SiO₂-like films on polymers synthesized in roll-to-roll atmospheric pressure-PECVD for gas diffusion barrier applications,” *Plasma Process. Polym.*, vol. 7, no. 8, pp. 635–639, 2010.
- [42] S. C. Deshmukh and E. S. Aydil, “Investigation of low temperature SiO₂ plasma enhanced chemical vapor deposition,” *J. Vac. Sci. Technol. B Microelectron. Nanom. Struct. Process. Meas. Phenom.*, vol. 14, no. 2, pp. 738–743, 1996.
- [43] H. J. Kim, Q. Shao, and Y.-H. Kim, “Characterization of low-dielectric-constant SiOC thin films deposited by PECVD for interlayer dielectrics of multilevel interconnection,” *Surf. coatings Technol.*, vol. 171, no. 1–3, pp. 39–45, 2003.
- [44] C. Huang, C.-H. Liu, and S.-Y. Wu, “Surface characterization of the SiO_x films prepared by a remote atmospheric pressure plasma jet,” *Surf. Interface Anal. An Int. J. devoted to Dev. Appl. Tech. Anal. surfaces, interfaces thin Film.*, vol. 41, no. 1, pp. 44–48, 2009.
- [45] J. Park, I. Henins, H. W. Herrmann, G. S. Selwyn, and R. F. Hicks, “Discharge phenomena of an atmospheric pressure radio-frequency capacitive plasma source,” *J. Appl. Phys.*, vol. 89, no. 1, pp. 20–28, 2001.
- [46] S. E. Babayan, J. Y. Jeong, V. J. Tu, J. Park, G. S. Selwyn, and R. F. Hicks, “Deposition of silicon dioxide films with an atmospheric-pressure plasma jet,” *Plasma Sources Sci. Technol.*, vol. 7, pp. 286–288, 1998.

- [47] Y. Sawada, S. Ogawa, and M. Kogoma, "Synthesis of plasma-polymerized tetraethoxysilane and hexamethyldisiloxane films prepared by atmospheric pressure glow discharge," *J. Phys. D. Appl. Phys.*, vol. 28, no. 8, pp. 1661–1669, 1995.
- [48] T. Opalinska, B. Ulejczyk, and K. Schmidt-Szalowski, "Applications of pulsed discharge to thin-film deposition," *IEEE Trans. Plasma Sci.*, vol. 37, no. 6, pp. 934–940, 2009.
- [49] B. Twomey, D. Dowling, G. Byrne, L. O'Neill, and L. A. O'Hare, "Properties of siloxane coatings deposited in a reel-to-reel atmospheric pressure plasma system," in *Plasma Processes and Polymers*, 2007, vol. 4, no. SUPPL.1, pp. 450–454.
- [50] S. A. Starostin, P. A. Premkumar, M. Creatore, H. De Vries, R. M. J. Paffen, and M. C. M. Van De Sanden, "High current diffuse dielectric barrier discharge in atmospheric pressure air for the deposition of thin silica-like films," *Appl. Phys. Lett.*, vol. 96, no. 6, pp. 21–24, 2010.
- [51] S. A. Starostin, M. Creatore, J. B. Bouwstra, M. C. M. Van De Sanden, and H. W. De Vries, "Towards roll-to-roll deposition of high quality moisture barrier films on polymers by atmospheric pressure plasma assisted process," *Plasma Process. Polym.*, vol. 12, no. 6, pp. 545–554, 2015.
- [52] F. M. Elam, S. A. Starostin, A. S. Meshkova, B. C. A. M. Van Der Velden-Schuermans, M. C. M. Van De Sanden, and H. W. De Vries, "Defect prevention in silica thin films synthesized using AP-PECVD for flexible electronic encapsulation," *J. Phys. D. Appl. Phys.*, vol. 50, no. 25, 2017.
- [53] Y. Liu, S. Welzel, S. A. Starostin, M. C. M. Van De Sanden, R. Engeln, and H. W. De Vries, "Infrared gas phase study on plasma-polymer interactions in high-current diffuse dielectric barrier discharge," *J. Appl. Phys.*, vol. 121, no. 24, 2017.
- [54] A. Granier, M. Vervloet, K. Aumaille, and C. Vallée, "Optical emission spectra of TEOS and HMDSO derived plasmas used for thin film deposition," *Plasma Sources Sci. Technol.*, vol. 12, no. 1, p. 89, 2003.
- [55] M. Abbasi-firouzjah, S. Hosseini, M. Shariat, and B. Shokri, "The effect of TEOS plasma parameters on the silicon dioxide deposition mechanisms," *J. Non. Cryst. Solids*, vol. 368, pp. 86–92, 2013.
- [56] P. J. Stout and M. J. Kushner, "Monte Carlo simulation of surface kinetics during plasma enhanced chemical vapor deposition of SiO₂ using oxygen/tetraethoxysilane chemistry," *J. Vac. Sci. Technol. A Vacuum, Surfaces, Film.*, vol. 11, no. 5, pp. 2562–2571, 1993.

2

THIN FILMS: SURFACE CHARACTERIZATION

A complete thin films surface characterization is mandatory to understand the influence on thin films properties of the specific experimental set-up and operating conditions used in this work. As known, the power applied and the amount of precursor injected into the plasma source have a key role in the determination of the energy released per TEOS molecule and consequently on the dissociation efficiency of the plasma source. Therefore, as first step of the study, the effect of such parameters on the structure and chemistry of the film surface have been studied in detail in order to define the best operating condition for the achievement of smooth, inorganic (silica-like) and defect-free thin films on thermo-sensitive substrates. The same operating conditions will be then employed for the poly-diagnostic study of the most significative emitting (chapter 3) and non-emitting (chapter 4) species produced during the gas-phase deposition process in order to provide a global characterization of the process and define the physico-chemical parameters playing a key role in the attainment of high quality inorganic thin films onto polymeric substrates.

2.1 MATERIALS and METHODS

An overview of Atmospheric Pressure Plasma Jet (APPJ) configurations typically used for deposition purposes and a detailed description of the plasma deposition system used in this work is presented in the first section of this chapter. Afterward, different kind of surface characterization techniques are introduced by means of a brief description of the basic working principle followed by a detailed description of the specific systems employed in this dissertation.

2.1.1 Atmospheric Pressure Plasma Jet (APPJ) for thin film deposition

The employment of APPJs for thin film deposition is not an easy task both in terms of experimental set-up and device configurations. Indeed, beyond the common APPJ limitations such as the use of expensive noble gasses and small treatment zones, all the problems linked to the determination of the optimal precursor injection configuration have

to be taken into account.[1] Up to now different designs have been investigated for the deposition on complex thermo-sensitive surface, such as DBD-Jet and Corona-Jet configurations, however each of these two main categories presents several drawbacks.[2],[3] In case of DBD-Jets the plasma discharge is typically generated between two coaxial cylindrical electrodes and blown out into the open space by a gas flow to form an afterglow plume in contact with the target.[4] The spatial separation between the plasma generation zone and the plasma treatment area can lead to very low plasma temperature in the point of application and can prevent the direct influence of the target on the plasma discharge.[5] However, in case of deposition processes, the main fragmentation reactions induced by electron impact or argon metastable atoms take place inside the “active” plasma region contained between the electrodes and the risk of thin film deposition on conductive/dielectric structural parts is high.[6] Thus, the reduction in terms of deposition rate and the need of periodic maintenance makes this technology unsuitable for industrial processes.

Otherwise, in case of Corona-Jet devices the precursor molecules are directly dissociated near the target since the plasma discharge is generated between the single HV tip and the substrate. It’s worth mentioning that this type of plasma source could operate in “floating-mode”, without ground electrode, or in the “DBD-mode” with the HV single electrode directly faced on a grounded plate, covered with a dielectric barrier in order to stabilize the discharge. In both cases, the discharge, characterized by an intensive corona plasma region located close to the tip of the HV electrode, is in direct contact with the target, thus leading to the occurrence of gas-surface reactions which often play a significant role in the polymerization process. The role of surface reactions in thin film growth processes and chemical composition have been presented in section 1.3.2 for the case of low pressure plasmas but is also reported by R. Reuter for the deposition of SiO₂-like thin films in HMDSO/O₂ mixtures under atmospheric pressure conditions.[7] Beside these advantages, one of the main drawbacks of this configuration operating in the “DBD-mode” is the influence of the target electric properties on the plasma discharge behaviour. Indeed, the plasma plume can change in terms of stability, shape, strength and temperature as function of the substrate properties. It has been proved that by adding an insulating substrate, e.g a polymeric foil, the total dielectric thickness increase and the discharge intensity decrease, while, in case of conductive samples, the current density could increase enough to reach process temperatures similar to thermal plasmas (“arc” mode). [8] In spite of this, the high energy input released and the possibility to customize the plasma discharge according to several industrial requirements make the use of such “direct” plasma jets very attractive. Moreover, the multiple similarities between a Corona-jet operating in the “DBD-mode” and a common planar DBD configuration makes the studies performed by using this technology easily transferable to “direct” plasma configurations in general.

Some of the few common points between DBD-Jet and Corona-Jet configurations consist in the suitability to perform local treatments of complex 3D surfaces and the possibility of varying the scale of the treatment zone from few square centimeters down to the micrometric range. Moreover, APPJ can easily be moved by automated systems allowing the thin film deposition on larger surfaces. In light of this, APPJ can be used for the deposition of micro-engineered thin films potentially applicable in a broad range of fields such as the biomedical one, for tailoring protein adsorption and controlling stem cell adhesion, or the processing of micro-electronic devices.

In the following section 2.1.1.1 the APPJ device employed in this work will be introduced in detail. The Corona-jet plasma source, developed in our laboratories, was

already used in the past with different kinds of power supplies for a broad range of applications. For example, between 2014 and 2016, a first Corona-jet prototype, slightly different from the device reported in this dissertation and driven by a commercial nano-pulsed DC generator, was used for the plasma-polymerization of acrylic acid (pPAA) and the synthesis and deposition of nanocomposite coatings (pPAA +AgNPs) on Polyethylene (PE) sheets.[9],[10] In the same years a similar set-up was fully characterized by iCCD imaging, OES and Schlieren imaging in order to investigate the fluid-dynamic behaviour, the characteristic temperature, and radiation emission of the plasma device working in He or Ar mixtures. [11] In 2018, the use of the plasma source for the synthesis of copper-based nanostructures in different liquid mediums was also discussed in details.[12] The Corona-jet prototype, excited by a micro-pulsed generator, was then considered by the research group of the University of Bologna for the polymerization of biocompatible amine/amide-rich coatings in a single-step plasma process. This last work, which opens interesting perspectives in the field of biomaterials manufacturing, is presented in the Annex I at the end of this dissertation. Even though the use of the above-mentioned device was already employed for polymerization purposes, the use of such plasma source for Si-based thin films polymerization remained so far unexplored.

2.1.1.1 Plasma deposition system

The layout of the experimental set-up employed in all the studies conducted within this dissertation is shown in **Figure 2.1**. The single-electrode Corona Jet (AlmaJet) is connected to an AC power supply (AlmaPulse, Almaplasma srl) which can provide different voltages (1-20kV) at different frequencies (1-5kHz, 10-20kHz) with a variable duty cycle (1-100%). The set-up also includes a gas console composed of three mass flow controllers (EL-FLOW, Bronkhorst) and a bubbling system for precursor injection.

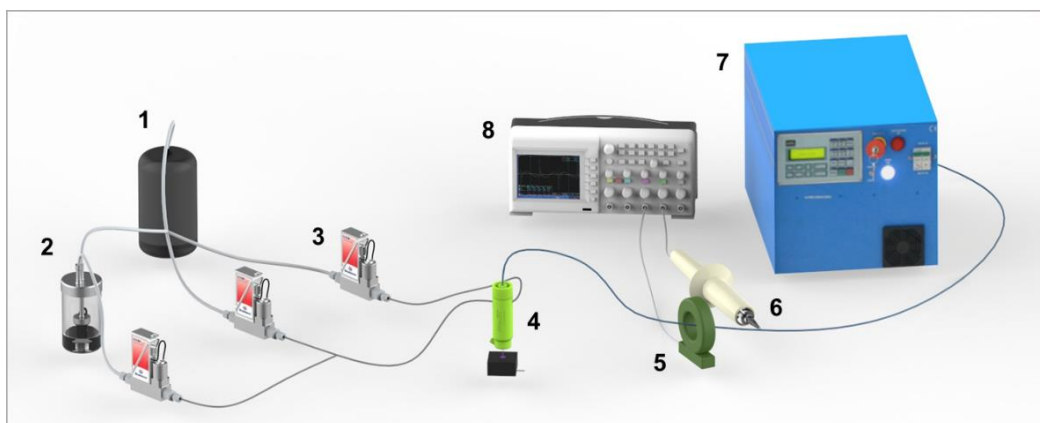


Figure 2.1 –Layout of the plasma deposition set-up: Ar supply (1), bubbling system (2), digital mass flow controller (3), plasma source (4), current probe (5), voltage probe (6), HV generator (7), oscilloscope(8)

The HV single electrode Corona Jet, presented in **Figure 2.2**, is composed by a 19.5 mm long stainless steel sharpened metallic needle with a diameter of 0.3 mm and a main cylindrical body 3D-printed with an ABS-like resin. Such main body is structured as follows:

- Component A → an external casing which directs the process gasses towards the plasma region and allows to fix the plasma source on the head of a CNC system.
- Component B → a diffuser, screwed on the component A, that allows to introduce a primary gas flow in correspondence of the HV tip and a secondary gas flow in the region downstream the metallic HV tip. The outlet orifice size can be modified to adapt to specific applications.

A peculiarity of this source is the possibility of operating with two different gas supplies at the same time. Indeed, a primary gas, which sustain the plasma and allows the precursor injection, and a secondary flow, typically employed as shield gas in order to limit ambient air diffusion into the active plasma discharge, can be introduced simultaneously in the main body through two different inlets.

In this work the plasma source was used in the “DBD-mode” configuration with the HV tip facing a planar ground electrode covered with a 10 mm-thick dielectric PVC barrier. For all the experiments reported in this dissertation the gap between the HV electrode and the dielectric plate was fixed at 15 mm, significantly larger with respect to the typical values (1-2 mm) for the planar DBD configurations due to the corona effect in correspondence of the HV tip.

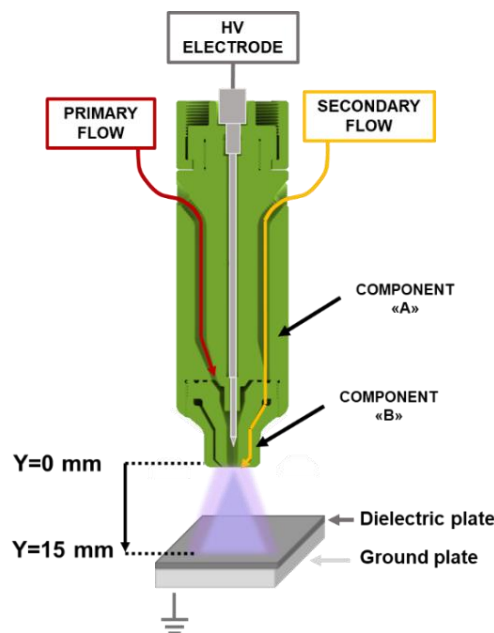


Figure 2.2 – Scheme of the HV single electrode plasma source operating in the “DBD-mode”

The Corona-jet plasma device can be also easily implemented in the fully automated AlmaPLUS (AlmaPlasma srl), which is equipped with a CNC pantograph, a remotely controlled liquid and gas console composed of four mass flow controllers (EL-FLOW, Bronkhorst), a liquid flow meter (miniCORI flow, Bronkhorst), a controlled evaporation mixer (CEM, Bronkhorst) and a remotely controlled high voltage pulsed generator (AlmaPULSE, Almaplasma srl). By using the AlmaPLUS system the plasma source can be handled, thus allowing to perform localized plasma treatments as well as deposition treatments on complex three-dimensional substrates.

2.1.1.2 Operating conditions and electrical characterization

For all the deposition tests, a flow of 2 standard litres per minute (slm) of Ar was injected in the discharge region through the primary channel; while, simultaneously, a second flow of 3 slm of Ar was introduced through the secondary gas channel in the region downstream the HV electrode tip. The amount of precursor content in the system is controlled by setting the flow of carrier gas passing through a bubbling system filled with Tetraethyl orthosilicate (TEOS, $\text{SiO}_4\text{C}_8\text{H}_{20}$, Sigma-Aldrich, $\geq 99\%$). Three different carrier gas flows (40, 65 and 90 ml/min), which correspond to 11, 17 and 24 ppm of TEOS introduced in the primary channel (by assuming 20 °C of gas flow temperature and 1 Torr of TEOS saturation pressure), were used for thin films deposition purposes. The ppTEOS coatings were deposited on Goodfellow Polypropylene (PP) foils (thickness = 0.5 mm, $\text{Ø}=25$ mm) for 60 seconds of deposition time. The plasma device was operating at four different power conditions (6, 8, 10, 12 kV) by keeping the frequency value fixed at 12 kHz. The discharge evolution between electrodes under different operating condition is presented in **Figure 2.3**. The plasma device clearly exhibits two different working modes: the 6 kV-mode (see Figure 2.3(A)), characterized by a stable uniform glow-like discharge that partially covers the PP surfaces and the 12 kV-mode (see figure 2.3(D)) consisting of a filamentary discharge with a larger deposition spot in correspondence of the PP substrate. It is also important to emphasize that the Ar/TEOS plasma discharge is sustained in ambient air and consequently the air back diffusion has to be taken into account during the discussion of the results.

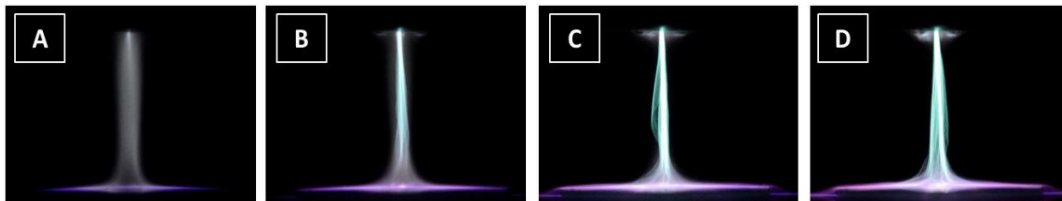


Figure 2.3 - Ar/TEOS plasma discharge generated under four different operating conditions: 6kV-12kHz (A), 8kV-12kHz (B), 10kV-12kHz (C) and 12kV-12kHz (D)

To measure the power applied to the plasma device, voltage and current waveforms were recorded by means of a Tektronix P6015A high voltage probe and a Pearson 6585 current transformer connected to a Tektronix DPO40034 digital oscilloscope. The current transformer was positioned on the ground cable to measure the active power effectively released to the plasma source. The input power results, obtained from the I-V waveforms acquired during the deposition treatment, are shown in **Figure 2.4**.

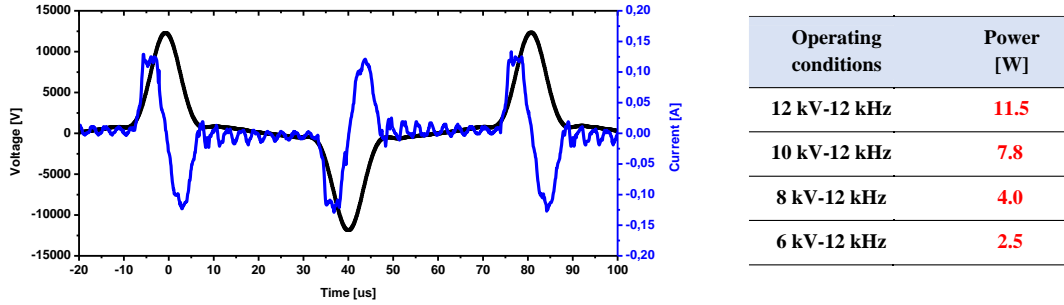


Figure 2.4 – Voltage and current waveforms of the APPJ used in this work (left); input power results obtained under four different operating conditions (right)

2.1.2 ATR-FTIR

Attenuated total reflection (ATR) Fourier-transform infrared spectroscopy (FTIR) technique is a highly effective method for the reliable identification of the functional groups present on the thin film surface. Typically, a Fourier Transform Infrared Spectrometer is composed by an IR source, an interferometer, a sample compartment, a detector and a computer. However, in order to overcome the most challenging aspects of traditional infrared analyses, such as sample preparation and spectral reproducibility, the use of additional sampling tools is very common.[13] Among these, the possibility of recording spectra at various light incidence angles has rapidly made the use of ATR accessories the first choice for thin films characterization. Indeed, unlike the other acquisition modes, the attenuated total reflectance (ATR) spectral mode considers also the internal reflection of the IR beam after the contact with a solid sample. In details, the IR source generates a beam which is focused on the ATR tip by means of an interferometer. In turn, the ATR tip, typically composed by a crystal with a high refractive index, focuses the IR beam on the sample interposed between the ATR accessory and a detector. As shown in **Figure 2.5**, the incident beam is then reflected several times at the interface between the two materials (the ATR crystal and the thin films surface) having different refractive indexes by creating an evanescent wave that extend into the sample with a penetration depth included between $0.5 \mu\text{m}$ - $2 \mu\text{m}$ as defined by the Harrick's equation [14] :

$$d_p = \frac{\lambda}{2\pi (n_1^2 \sin^2 \theta - n_2^2)^{\frac{1}{2}}} \quad (2.1)$$

where λ is the absorption wavelength, θ is the IR beam angle of incidence while n_1 and n_2 are the refractive indexes of the ATR crystal and the thin film analysed respectively. Finally, the detector records the IR beam as an interferogram signal, which can then be used to generate an IR spectrum by applying the Fourier transform.

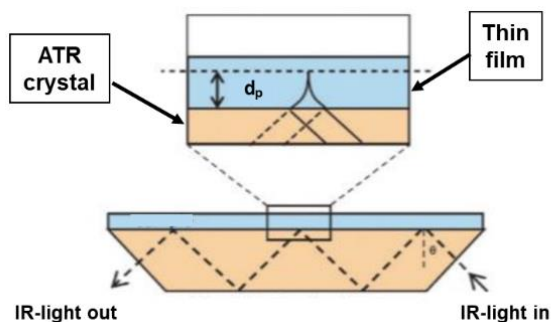


Figure 2.5 – Schematic illustration of an ATR cell

Within the thin film the IR beam excites the ground state molecules which selectively absorb radiation at specific wavelengths depending on their molecular composition, nature of the bonds and structure. A change in terms of dipole moment of the specific excited molecule give rise to the absorption of the infrared radiation and consequently the absorption band intensity increases as larger is this change. Among the several vibration modes possibly excited by the IR beam, stretching modes (ν) and bending modes (δ) are the most important. The stretching vibrations involve a change in the interatomic distance along the axis of the bond and can be classified by the symmetry of the vibration in symmetrical (in-phase) stretching (**Figure 2.6(a)**) or asymmetrical (out-of-phase) stretching (Fig. 2.6(b)); while bending vibrations, which involve a change in the bond angles between atoms, can be classified in scissoring (Fig. 2.6(c)), rocking (Fig. 2.6(d)), wagging (Fig. 2.6(e)), and twisting vibrations (Fig. 2.6 (f)). [15]

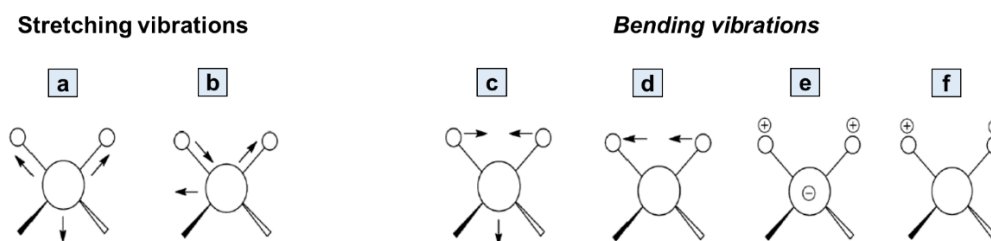


Figure 2.6 –Stretching and bending vibration modes [15]

Although ATR-FTIR is currently the most used technique for thin film characterization, several efforts are required in order to perform a correct spectral assignment. Indeed, the influence of the polymeric target, the interaction between the evanescent wave and the thin film layer and the effect of the angle of incidence on absorption peaks intensities or wavenumbers have to be take into account for a good thin film chemical analysis.

In general, it is important to highlight that the relative intensity of FTIR spectra absorption peaks could be also used to provide preliminary information about thin films thickness. The qualitative analysis of the thin films thickness behaviour as a function of the power input is presented in section 2.2.1.

2.1.2.1 ATR-FTIR measurement settings

FTIR-ATR spectra were recorded by using an Agilent Cary 660 spectrometer working at a spectral resolution of 2 cm^{-1} . The spectrometer was equipped with an ATR sampling accessory, using a diamond crystal as internal reflection element with an incidence angle of 45° with respect to the normal of the thin film surface. All the tests were performed in the center of the sample and a total of 32 scans were recorded for each spectrum.

2.1.3 XPS

In order to complete the chemical characterization of thin films, FTIR results have to be complemented with data obtained with quantitative surface techniques. Among these, X-ray Photoelectron Spectroscopy (XPS) is one of the most widespread techniques thanks to the possibility of providing not only a detailed description of the thin film atomic composition, but also specific details about the chemical bonds present on the surface.[16] The XPS instrumentation, shown in **Figure 2.7**, is composed of a radiation source which generate X-rays with a known energy ($h\nu$), electrostatic lenses aimed at directing photoelectrons from the thin film surface into an electron energy analyser and an electron detector placed at the end of the analyser.[17] In general, the equipment must work in ultra-high vacuum conditions in order to avoid collisions between photoelectrons and gas molecules.

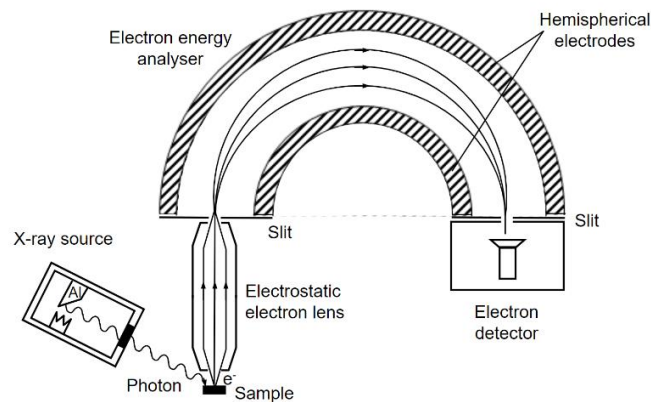


Figure 2.7- Schematic representation of an X-ray analyser [17]

XPS measurements are based on the photoelectric effect: when an X-ray interacts with an atom of the thin film surface, a photoelectron can be emitted. The kinetic energy (E_k) of these photoelectrons, detected by the electron energy analyser, is strictly dependent on the binding energy (E_b) of the atom, the energy of the incident X-ray ($h\nu$) and the work function of the spectrometer (Φ) as defined by the following equation:

$$E_b = h\nu - E_k - \Phi \quad (2.2)$$

Each atom has core electrons (electrons not participating in chemical bonds) whose characteristic binding energies permit the direct identification of each element present on the surface of the thin film analysed. Therefore, different elements can be determined

through identification of XPS peaks at characteristic binding energies and the amount of each element is directly related to the number of electrons detected. [18]

Furthermore, the peak position is influenced by the atomic environment of the probed elements. Indeed, a shift in terms of binding energy take place when the electron density around core electrons increase or decrease due to the presence of specific bonds between atoms. Detailed information about specific chemical bonds and respective concentrations can be obtained by performing deconvolution analysis of the XPS peaks.

In conclusion, it is worth to mentioning that the XPS information depth is roughly in the order of up to 10 nm, but the technique is especially sensitive in the first 4 nm of the thin film surface.

2.1.3.1 XPS measurement settings

XPS surface analysis on ppTEOS thin films were performed by using a Versaprobe II system (Physical Electronics (PHI), USA) with a monochromatic Al K X-ray source ($h\nu = 1486.6$ eV) operating at 23.3W. The photoelectrons were detected with a hemispherical analyser positioned at 45° respect to the normal of the thin film surface while the working pressure is maintained below 10^{-6} Pa during analysis. The atomic composition of samples was identified and quantified from XPS survey scans by using CasaXPS software. C1s spectrum (285.0 eV) was used to calibrate the energy scale. The deconvolution of high-resolution peaks (C1s and Si2p) were performed using Gaussian-Lorentzian (G-L ratio is set between 80% to 100%) peak shapes and the full-width at half maximum (FWHM) of each line shape was constrained below 1.7 eV.

2.1.4 AFM

The microscopically rough surface of ppTEOS thin films is difficult to observe by means of traditional electron microscopy techniques. As a consequence, the use of a profilometer-based technique such as Atomic Force Microscopy (AFM) is very common for an accurate characterization of thin films in terms of surface structure and roughness. [19] The principle of AFM technique is based on the measurement of different forces between a sharp tip and a target surface as shown in **Figure 2.8**.

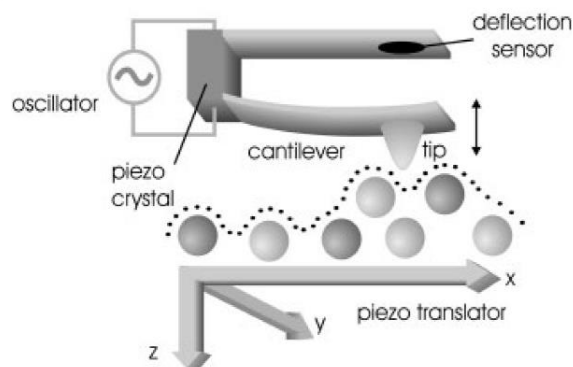


Figure 2.8- Principle of AFM technique [19]

Such interaction forces, measured via deflection of a soft cantilever while the tip is moved across the surface, allow to obtain different quantitative topographic information as a function of the chosen operating mode. In general, although various types of forces (e.g., attractive, repulsive, magnetic, electrostatic, van der Waals) could affect the tip movement during the sample scanning, signal generation in AFM is essentially based on interatomic repulsive forces influenced by the total electron density around an atom and characterized by an extreme short-range nature. For thin films analysis the tapping mode is typically used to image surfaces under non-damaging conditions. In this case, the cantilever is driven near its resonance frequency (typically 200 – 300 kHz) by means of a piezo oscillator, thus providing only an intermittent contact between the tip and sample. The motion of the cantilever, determined by the amplitude, the phase, and the frequency imposed, follows the sample surface morphology and together with the x- and y- coordinates produces a 3D image of the probed surface. By using specific softwares, it is then possible calculate the surface roughness from the generated 3D images.

There are several parameters commonly employed to characterize the surface roughness, among these the root mean square (RMS) roughness value, also called R_q , and the R_z value (Average Maximum Height of the Profile) are the most used to compare different surface morphologies. [20] The function R_q is the root mean square average of the profile heights over the evaluation length (L) while R_z is the average value of the heights of five highest profile peaks and the depths of five deepest valleys within L.

Moreover, the AFM technique can be used to determine the thickness of the thin films by partially covering the polymeric sample with a mask before starting the plasma-polymerization process. After the treatment, the mask must be removed and both the covered and the uncovered zones can be investigated by AFM. Consequently, from the difference between the height of the uncovered area (thin film) and the height of the covered area (untreated polymer), the thickness of the plasma-polymerized films can be deduced.

2.1.4.1 AFM measurement settings

AFM analysis on ppTEOS thin films were performed in ambient conditions with a Multimode scanning probe microscope (Digital Instruments — USA) equipped with a Nanoscope IIIa controller. AFM images were recorded in tapping mode with an OTESPA (Veeco) silicon cantilever in order to preserve the thin film surface. The recorded images are modified with an X and Y Plane Fit Auto procedure, afterwards the Nanoscope software is used for roughness measurements. Scan areas equal to 10 x 10 μm and 30 x 30 μm were used for roughness analysis. For the thickness measurements, the PP sample have been covered with a Kapton tape before the plasma treatment performed by preserving the same operating conditions used for 2D AFM images.

2.1.5 SEM

Plasma deposited thin films are characterized by a complex nano-, micro-, and macro morphological structure and this complexity requires the use of advanced instruments, such as Scanning Electron Microscopy (SEM), for surface imaging. This technique, typically working in high vacuum conditions ($0.1\text{-}10^{-4}$ Pa), can highlight the key structural features of the deposit by focusing an electron beam on the target to analyse. As shown in **Figure 2.9** an electron gun, composed by the electron source and the accelerating anode, typically

accelerates electrons through 1-30 kV of accelerating voltage. [21] These electrons, with a typical energy between 1 and 30 keV, are then collimated and focused by electromagnetic lenses on the target thus producing a primary electron beam. The interaction of the primary electron (PE) beam with the surface generates mainly secondary electrons, backscattered electrons and characteristic X-ray radiations which are collected by three different detectors in order to obtain a several information about thin film morphology, microstructure and chemical composition. In details, the secondary electron (SE) detector collects the SE produced by several inelastic scattering mechanisms between PE and thin films atoms in order to provide information on the surface topography, while the back-scattered electrons (BSE) detector collects primary electrons reflected from the thin film due to electrostatic interaction between atoms and electrons of the surface and primary electrons thus providing both chemical and topographical information. On the other hand, characteristic X-rays are generated by electron transitions within the atoms in the thin film, and their energy is strictly associated to the elements which produce them. The X-rays with different energies reach the detector, forming an energy dispersive X-ray (EDX) spectrum useful to obtain qualitative information about atoms present in the thin films.

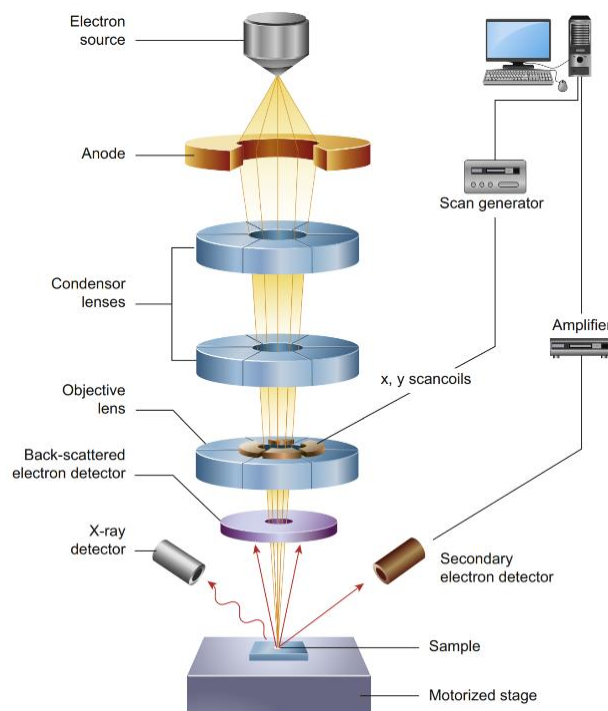


Figure 2.9- Schematic diagram of the core components of a SEM microscope [21]

Furthermore, from a practical point of view, non-conductive polymeric samples have to be coated with a thin layer of electrically conducting material, e.g gold or platinum, in order to avoid the accumulation of electrostatic charges on the surface after the electron beam impact. Details of SEM measurement settings are provided in the following section.

2.1.5.1 SEM measurement settings

The coating morphology was investigated by means of a FEI XL30 Scanning electron microscope by applying an accelerating voltage of 7 kV on samples. Before measurements

the samples have been Au coated with a Baltec SCD005 Sputter Coater (Bal-Tec AG) in order to avoid a charge effect. Thin film morphologies and defects have been observed by using 2000x of magnification in five different points of the sample.

2.2 RESULTS and DISCUSSION

Over these sections the precursor flow and the applied power effect of the on the thin films chemical properties will be discussed by FTIR technique. In addition, the effect of process temperature and power on the structural properties of ppTEOS films deposited onto PP samples will be investigated by XPS, AFM and SEM analyses. Substrate temperature measurements, obtained by using an IR camera, will be also discussed for a complete understanding of the deposition process in terms of thermal stress and coating defects.

2.2.1 Chemical structure

In this section are shown all results obtained by FTIR and XPS analysis on ppTEOS thin films carried out on PP samples. The choice of PP substrates as thermo-sensitive materials have been dictated by two main reasons: the widespread use of this material in the packaging industry and its chemical-morphological features extremely suitable for silica-based thin films characterization. Indeed, from **Figure 2.10** it is clear that the untreated PP sample FTIR spectrum does not present peaks in correspondence of the most significant silica-based thin films absorption regions, namely $400\text{-}1300\text{ cm}^{-1}$ e $3200\text{-}3700\text{ cm}^{-1}$, thereby facilitating the identification of characteristic chemical bonds present in the TEOS coating.

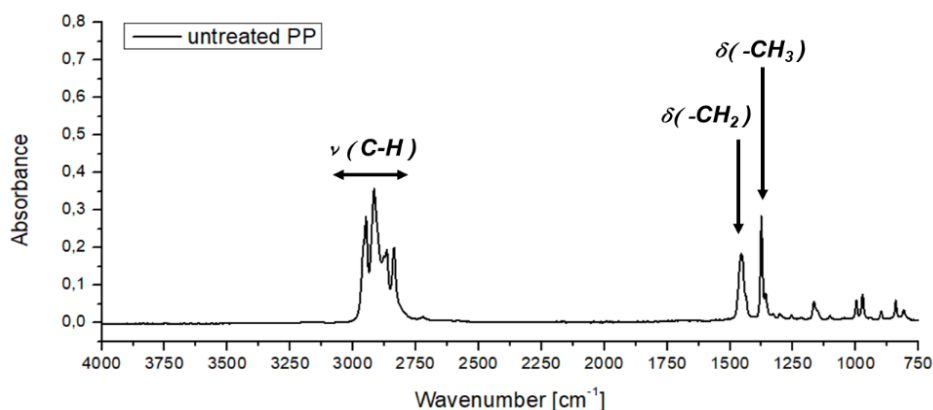


Figure 2.10 –FTIR spectrum of the untreated PP substrate

As a first step, the chemical bonds present in the deposited films are examined by ATR-FTIR spectroscopy. Before describing the most significant absorption peaks detected it's important to remind that FTIR spectra are influenced by both chemical composition and coating thickness and, consequently, it is not possible to obtain quantitative information on thin film chemical bonds. Anyway, as shown in **Figure 2.11**, large differences have been found in the FTIR spectra of the deposited thin films by varying the amount of TEOS

injected inside the plasma source. For a comparative evaluation of the thin film silica-like behaviour several absorption bands are of interest: the peaks related to hydroxyl groups (-OH) vibrations located either at 930 cm^{-1} or in correspondence of the broad band in the $2800\text{--}3700\text{ cm}^{-1}$ region, the inorganic absorption peaks in the region between 1040 and 1250 cm^{-1} (equivalent to the asymmetric stretching (AS) vibrations of the Si-O-Si unit) and the peak centered at 800 cm^{-1} corresponding to symmetric Si-O-Si stretching (SS) vibrations.

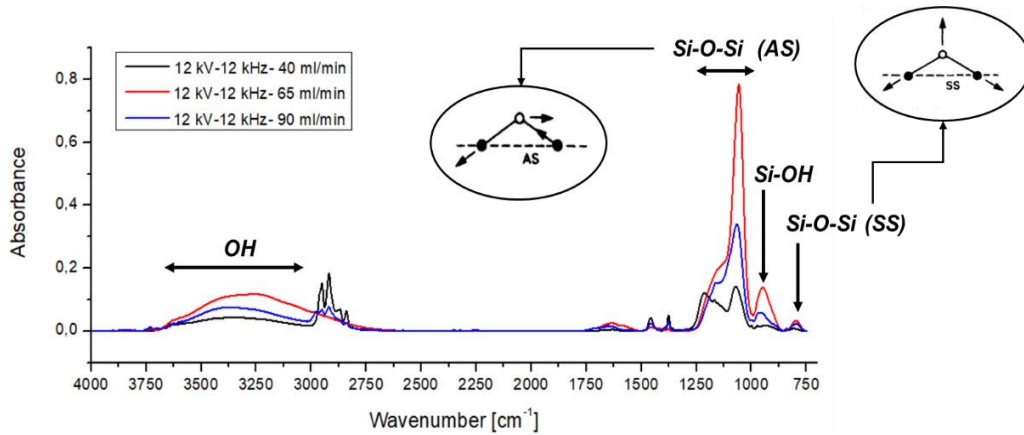


Figure 2.11 –FTIR spectra obtained by varying the carrier gas flow

In this respect, Starostine [22] has reported that the broad absorption feature relative to -OH and AS Si-O-Si unit vibrations can be attributed to an overlapping of different peaks. In details, drawing from literature of thermally grown thin SiO₂ films, the inorganic feature at $1040\text{--}1250\text{ cm}^{-1}$ includes the in-phase asymmetric stretch of Si-O-Si bonds (AS_1) and, at higher wavenumbers, the out-of-phase asymmetric stretching of Si-O-Si (AS_2) bonds (representing the out-of-phase motion of oxygen atoms). [23],[24] In turn, each AS mode can be split into transverse optical (TO) and longitudinal optical (LO) stretching modes which represent a variation in terms of Si-O-Si bond angle (θ) value, highly dependent from the SiO₂ network microstructure. As reported in **Figure 2.12** for the AS_1 case, such bond angle can vary from 120° to 180° by changing the peak position relative to the Si-O-Si bond. From the table, it's also clear that LO modes correspond always to higher wavenumbers respect TO modes.

Band	Maximum position (cm^{-1})	Full width at half-maximum (cm^{-1})	Mode type	Si-O-Si angle
1	1056	58	TO	132°
2	1091	46	TO	144°
3	1147	52	TO	180°
4	1200	68	LO	126°
5	1252	44	LO	142°
6	1300	57	LO	180°

Figure 2.12 – Type modes as function of the Si-O-Si bond angle (θ) [24]

By observing the table and taking into account the AS_1 and AS_2 splitting it is possible to deduce that the peak centered at 1060 cm^{-1} is certainly the result of TO AS_1 vibrations while the peak near 1250 cm^{-1} is probably due to LO AS_1 or TO AS_2 modes which absorbed in the same region. Despite the AS_1 peak shift towards higher wavenumbers have been used in the past to represent silica-like film densification, in our case the 1060 cm^{-1} peak is always in the same position for the three cases tested and consequently no conclusions can be drawn on this point.

Otherwise, the relative intensities of these peaks can be used to deduce interesting information about the film thickness, indeed, as reported by Lisovskii[24], the AS_1 peaks intensity typically increases with the film thickness while the number of peaks contained in the $1040\text{-}1250\text{ cm}^{-1}$ region increases when the thin film thickness decrease. In this respect, the spectra reported in Figure 2.11 show a non-linear trend of AS_1 peaks intensity with the precursor flow increasing and the appearance of the 1250 cm^{-1} peak only for the lowest amount of TEOS (40 ml/min) case. Consequently, it can be concluded that the maximum thin film thickness is achieved by using 65 ml/min of TEOS while, unexpectedly, the thickness decreases by using the highest flow rate (90 ml/min). This reduction could be related to an oversupply of TEOS molecules respect the dissociation efficiency of the plasma source or to the presence of different coatings features such as surface defects which could affect the penetration depth value described in Equation 2.1. On the other hand, the comparable intensities of 1060 and 1250 cm^{-1} absorption peaks in case of 40 ml/min of TEOS confirm a strong reduction in terms of coating thickness respect the 65 ml/min case.

As mentioned before, the broad absorption feature in the region between 2800 and 3700 cm^{-1} can be correlated to hydroxyl group vibrations. However, also in this case, two main peaks have to be taken into account: the first one, at 3350 cm^{-1} , can be attributed to OH bonds present in water molecules adsorbed by the thin film while the second one, centered at 3640 cm^{-1} , is related to the presence of silanol groups (Si-OH). In general, these peaks are used to provide preliminary informations about the thin film mass density since the presence of OH bond is strictly connected to the porosity of the silica-like layer. In our case, it's not possible to compare the peak intensity of the three spectra due to the thickness effect, however a strong contribution of hydroxyl groups is clearly present. The presence of water molecules may be indicated also by the low absorption band at 1650 cm^{-1} . [25]

In conclusion, ATR-FTIR spectra reveal a high inorganic content, while it should be noted from Figure 2.11 that no peaks due to C-H and C-O stretching vibrations are detected, indicating the absence of these organic bonds for all the flow rate examined.

The variation in terms of thin film composition and chemical structure has been evaluated also as function of the power applied to the plasma source. As shown in **Figure 2.13**, by varying the voltage input from 6 kV to 12 kV it is possible to detect only an improvement of thin film thickness while the chemical composition seems unaffected since there are no significant shifts in terms of wavenumbers. For accuracy reasons, the acquisitions have been performed in five different point of the thin films leading to similar results from a chemical point of view.

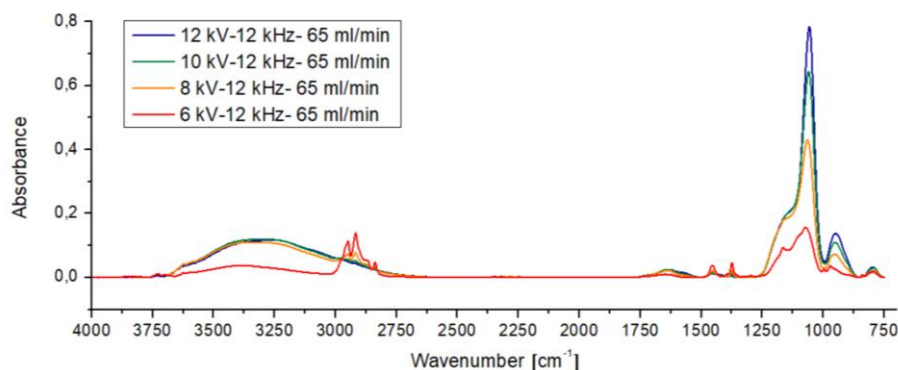


Figure 2.13 –FTIR spectra obtained by varying the power input

Furthermore, the atomic composition the topmost surface layers have been analysed with XPS as shown in **Table 2.1**. XPS measurements have been widely used in the past to elucidate information about the carbon percentage present in the silica-like coating since a chemical composition close to SiO_2 is a fundamental requirement for several applications such as, for example, the improvement of polymeric packaging barrier properties. However, as reported in section 1.3.1, the achievement of this target in pure Ar/TEOS mixture is not obvious even if the chemical structure of TEOS molecules is very similar to the pure silica due to the presence of siloxane (Si-O-Si) bonds. The results reported in Table 2.1, which show the chemical composition in the center of the samples by changing the voltage applied and the precursor gas flow, confirm this outcome for all the tested cases thus proving the presence of similar TEOS gas-phase dissociation pathways and surface reactions for all treatment conditions.

Table 2.1 - Atomic composition of ppTEOS thin films

Operating conditions	C (at%)	Si (at%)	O (at%)
6 kV-12 kHz-65 ml/min	15.15	25.96	59.46
12 kV-12 kHz-65 ml/min	15.73	26.07	58.2
12 kV-12 kHz-40 ml/min	16.35	25.1	58.55
12 kV-12 kHz-90 ml/min	14.52	25.91	59.57

However, even if it is clear that the atomic composition remains almost unchanged for all cases, the organic content of ppTEOS thin films presented in table is significantly reduced in comparison to the atomic composition of the starting monomer (C=61%, Si=8%, O=31%); therefore, in general, the plasma source is able to provide thin films with an improved inorganic behaviour.

As a consequence of the FTIR and XPS results achieved in the center of the sample, the amount of TEOS have been set at 65 ml/min, since the maximum (90 ml/min) and minimum (40 ml/min) gas flow conditions seemed to lead to lower deposition rates without improving the film chemistry in terms of inorganic content.

Moreover, in order to evaluate the chemical uniformity of coatings, XPS analysis were performed in ten different point across the central axis of the PP samples with 2.2 mm distance in between them. In **Figure 2.14** are reported the two different distributions of C_{1s}

and Si_{2p} XPS peaks obtained by using 6 kV and 12 kV at fixed precursor flow rate (65 ml/min).

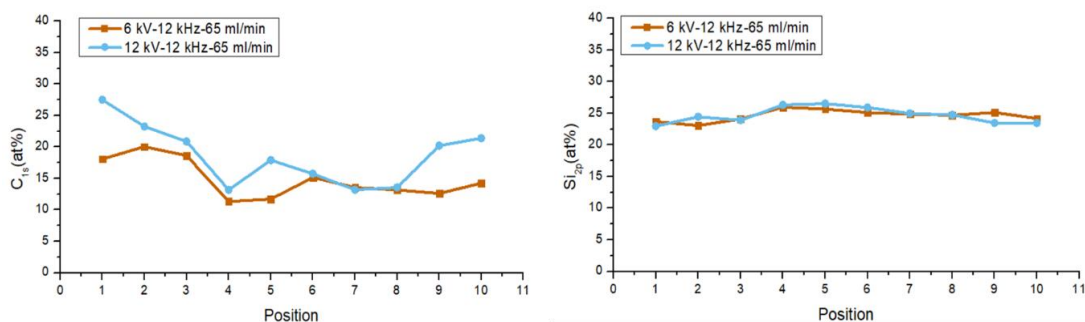


Figure 2.14 –C_{1s} and Si_{2p} intensity profiles across the central axis of the ppTEOS thin films

Despite the spatial distributions obtained in both cases reveals an almost uniform chemical composition across the deposits in terms of inorganic content (Si_{2p}), the graph on the left shows a non-uniform distribution of the carbon atoms percentage. As mentioned in the introduction paragraph, several factors could affect the organic/inorganic behaviour of the deposit. For instance, M. Abbasi-Firouzjah [26] has proven that the organic content decrease by increasing the amount of oxygen in case of low pressure plasmas while Babayan has presented the effect of high substrate temperatures on carbon removal by using the first plasma jet under atmospheric conditions.[27] In our case, the C % slightly increase by approaching the periphery of the sample where the gas-phase oxygen content should be maximum due to ambient air mixing and the substrate temperature should be minimum because of the distance from the HV tip. This result, particularly marked for higher operating conditions, highlights the fact that one or both factors slightly affects the chemical composition of thin films although the most significant gas-phase dissociation reactions, aimed at reducing the organic content, are strictly connected to the presence of Ar metastables and electrons, as confirmed by the almost uniform percentage of Si atoms all over the samples. The relative contribution of atomic oxygen and substrate temperature on the chemical composition will be discussed in the next sections by using OES and LIF techniques to study the gas-phase spatial distribution of excited or ground oxygen atoms and an IR camera for substrate temperature measurements respectively.

Furthermore, deconvolution of high resolution C_{1s} and Si_{2p} peaks have been carried out in order to identify the different chemical bonds present on the thin films surface. **Figure 2.15** shows the Si_{2p} peak deconvolution in case of ppTEOS thin films deposited by using the higher operating condition (12 kV-12 kHz). Detailed analysis have been performed on the center of the sample (equivalent to position 6 in Figure 2.14) and in correspondence of the edge (position 10 in Figure 2.14) in order to compare their chemical composition. In both cases, the Si_{2p} peak can be fitted by taking into account the contribution of four different peaks: the biggest peak at 103.4 eV is due to the pure inorganic SiO₄ content, while the three small peaks at 102.8 eV, 102.5 eV and 101.5 eV correspond to CH₃SiO₃, (CH₃)₂SiO₂ and (CH₃)₃SiO units, respectively. The central part of the deposit shows a low content of organosilicon units and a percentage of SiO₄ higher than 85% thus confirming an almost completely inorganic behaviour; on the other hand, the CH₃SiO₃ and (CH₃)₂SiO₂ contributions increase in correspondence of the external part of the deposit by reducing the SiO₄ content more than 10%. As expected, there is a negligible

amount of $(\text{CH}_3)_3\text{SiO}$ unit (less than 1%) in both cases. These results, reported in **Table 2.2**, highlights the difference in terms of chemical bond over the deposit.

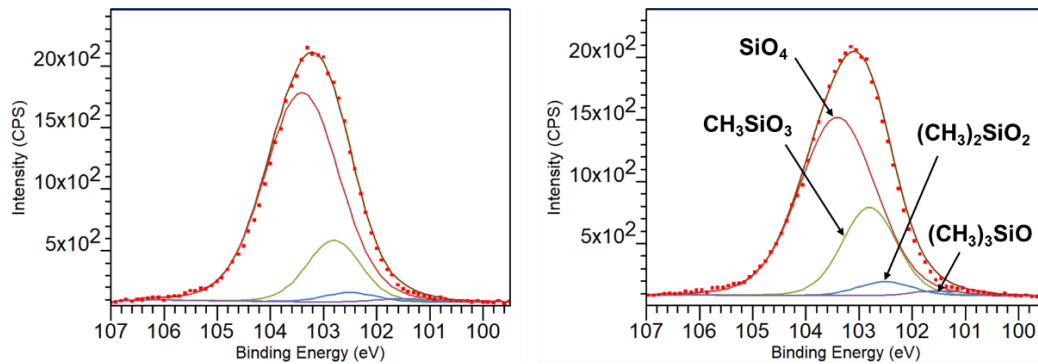


Figure 2.15 – Deconvoluted $\text{Si}2p$ peaks acquired in correspondence of the central point (left) and the edge (right) of the 12 kV-12kHz sample

Table 2.2 – Concentration (in %) of different silicon bonds present in the plasma deposited films

Operating conditions	SiO_4 103.4 eV	CH_3SiO_3 102.8 eV	$(\text{CH}_3)_2\text{SiO}_2$ 102.5 eV	$(\text{CH}_3)_3\text{SiO}$ 101.5 eV
12 kV-12 kHz-65 ml/min (center)	85.09	12.70	1.47	0.75
12 kV-12 kHz-65 ml/min (edge)	69.1	23.1	6.7	0.3
6 kV-12 kHz-65 ml/min (center)	79.35	17.0	2.6	1.03

Table 2.2 shows also clearly the Si-based bonds in case of lower operating conditions (6 kV-12 kHz). The central point of the deposit contains an amount of SiO_4 unit (79.3%) comparable with the previous case (85%) thus confirming that the power applied doesn't affect drastically the chemical composition of the deposit as already demonstrated by FTIR results. The small difference reported in the table could be caused by a different surrounding air diffusion into the active plasma zone or different process temperatures.

The chemical composition of 12 kV-12 kHz ppTEOS thin films have been then determined by performing the $\text{C}1s$ peak deconvolution as shown in **Figure 2.16**. The $\text{C}1s$ high-resolution spectrum can be decomposed into four components: a component at 284.9 eV due to C-C or C-Si-O bonds, a component at 285.9 eV due to C-O or CCO bonds, a component at 287.4 eV due to C=O bonds and a component at 289.4 eV due to the presence of OCO bonds. The main contribution in correspondence of 284.9 eV (69.1%) could be linked to the presence of C-C units due to the fact that the first products of TEOS dissociation, at electron energy values below 8-9 eV, are most likely hydrocarbon fragments containing C-C bonds such as C_2H_4 and C_2H_5 radicals. However, the generation of C-Si-O bonds is also possible because of gas-phase recombination mechanisms between previously dissociated SiO_2 unit and hydrocarbon fragments and therefore both contributions should be considered. On the other hand, all the other peaks are strictly connected to dissociation of H atoms from hydrocarbon fragments and the subsequent recombination of carbon compounds with O atoms. Part of these recombination products take part to production of CO_x gas species as proven by Y. Liu, while another part

contributes to the thin film formation. [28] The same XPS measurements performed on the 6 kV-12 kHz case have highlighted no difference in terms of carbon bonds.

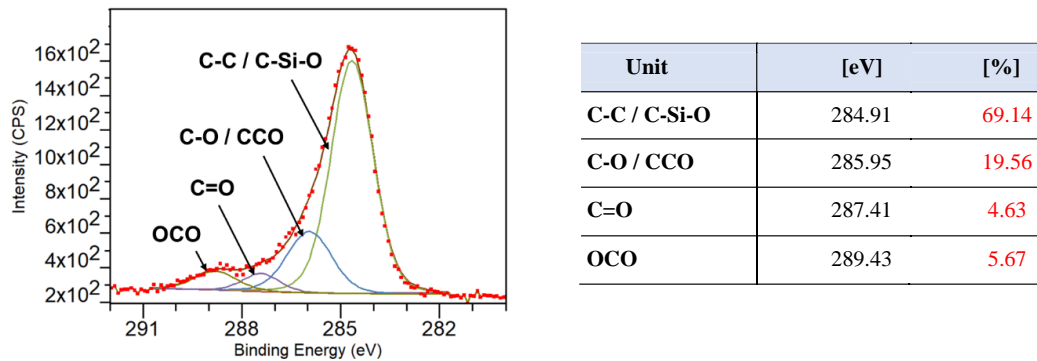


Figure 2.16 – Deconvoluted C1s peaks acquired in correspondence of the central point of the 12 kV-12kHz sample (left) and concentration (in %) of different carbon bonds present in the plasma deposited films (right)

2.2.2 Morphological structure and thickness measurements

This section provides a complete description of the thin films surface structure performed by AFM and SEM analysis. As reported in section 1.3.1, Y. Liu [28] has shown the relative importance of two possible competitive mechanisms that can occur during the plasma treatment, namely the thin film deposition by gas-phase nucleation pathways and gas-surface reactions or etching processes induced by the plasma discharge on the polymeric substrate. In order to check the effect of the Ar plasma treatment on the thermo-sensitive surface, the PP samples have been treated for 60 sec without precursor under maximum operating conditions (12 kV-12 kHz). As shown in **Figure 2.17**, the untreated PP has a rather smooth surface with some parallel trenches probably originated from the manufacturing process, while the plasma exposure seems to create a large number of mount-like structures on the surface. The nodules, up to 49 nm high (ΔY), could be constituted by highly oxidized short polymer fragments, called in the literature low molecular-weight oxidized materials (LMWOMs) or could be ascribed to remaining degradation products due to plasma etching reactions.[29] In any case, the plasma treatment without TEOS have an effect on the polymeric structure of PP foils and this aspect has to be taken into account for thin films analysis performed by AFM.

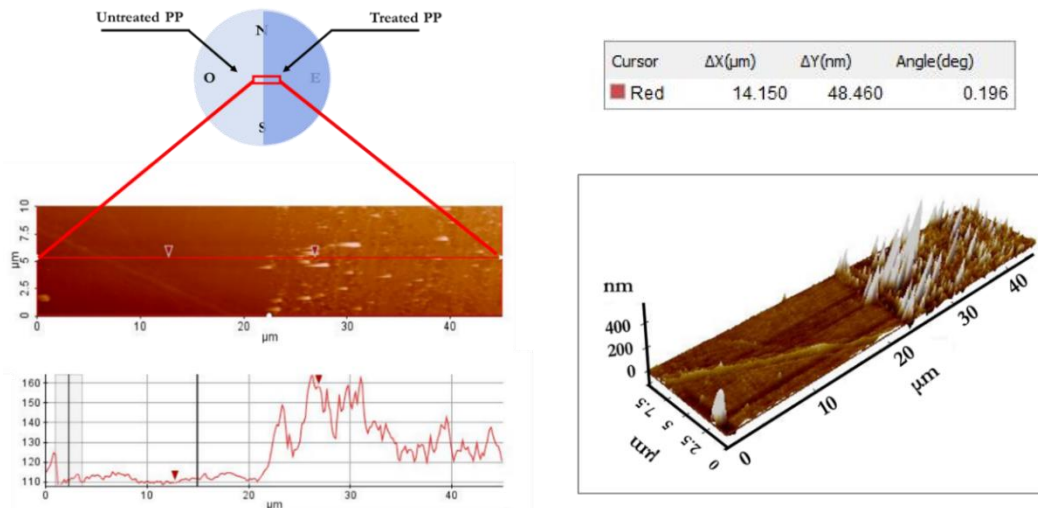


Figure 2.17 – AFM results of the PP samples after 60 seconds of plasma treatment

AFM was used to examine the surface morphology of ppTEOS thin films. **Figure 2.18** depicts the AFM images obtained by using two different deposition conditions, 6 kV-12 kHz and 12 kV-12 kHz, at fixed amount of TEOS (65 ml/min), while the roughness values of the plasma-polymerized films are presented in **Table 2.3**. As described in section 2.1.4, R_{rms} and R_z values indicate the root mean square average of the profile heights and the average of the vertical distance between the five maximum profile peaks and the five maximum profile valleys along the sampling length respectively. From the values reported in Table 2.3 it is possible to deduce that the surface roughness of the deposits decreases by increasing the voltage applied. This result can be explained by two different factors: 1) the presence of agglomerates on the surface of the deposit obtained at lower operating conditions consequent to a lower degree of dissociation and 2) a higher influence of the structures present on the etched PP surface in case of lower thickness values. While the thin film thickness reduction by decreasing the voltage input from 12 kV to 6 kV has been previously demonstrated by ATR-FTIR measurements, a quantitative study of the dissociation degree during the two different gas phase processes require the use of advanced diagnostic techniques, such as Gas Chromatography (GC), not employed in this dissertation. As a consequence, before further examinations, both effects must be taken into account.

Table 2.3- Roughness values (R_{rms} and R_z) of ppTEOS films for different operating conditions

Operating condition	R_{rms} (nm)	R_z (nm)
6 kV-12 kHz-65 ml/min	9.29	156
12 kV-12 kHz-65 ml/min	7.73	87

Moreover, AFM images show a substantial change in morphology by changing the power applied. A low power input results in the appearance of a defect-free surface with few mount-like features whereas higher operating conditions lead to thin film

microstructures characterized by a large amount of powder-like incorporations as well as the presence of cracks (as visible from 30 x 30 μm images). This result could be attributed to different dissociation degrees, as suggested before, resulting in different size of nanoparticles synthesized during the gas phase processes, in combination with a change in terms of polymeric substrate temperatures, as reported in the work of Starostin in case of ppHMDSO thin films.[22] In conclusion, RMS roughness values remain quite low ($R_q=7.7-9.3$ nm) for both cases but the number of small features on the surface clearly grows with an increase in terms of applied power.

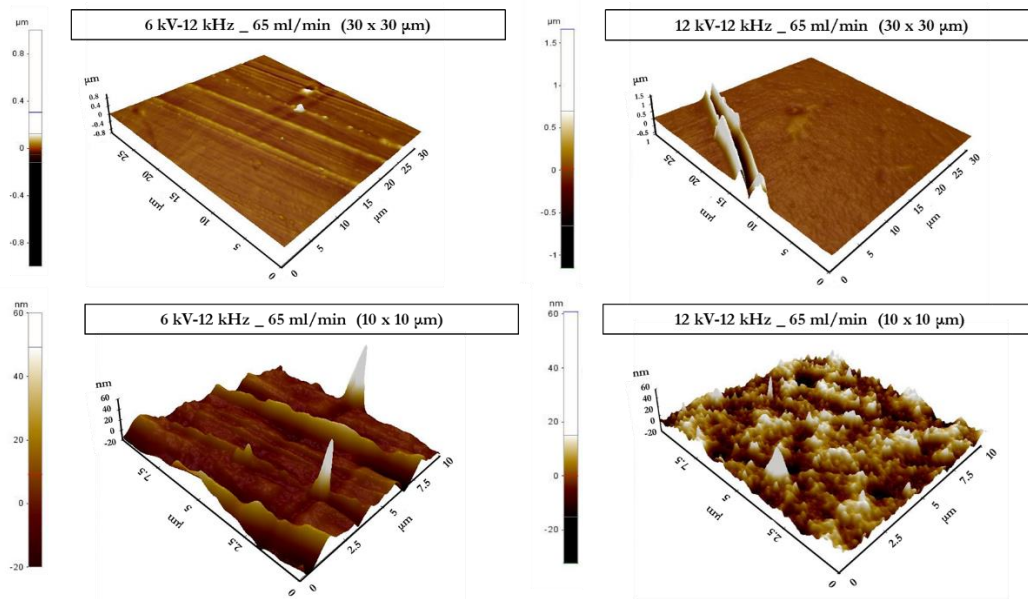


Figure 2.18- AFM images of ppTEOS thin films obtained by using two different scan areas

Besides providing useful information about the surface morphology of ppTEOS thin films, AFM can also be used to perform thickness measurements. In the present work the influence of the applied power on the thin films thickness has not been proved since AFM micrographs of the silica-like coatings deposited at 12 kV-12 kHz (**Figure 2.19**) do not allow to perform any estimation due to the occurrence of a strong heating-up of the PP surface or etching phenomena. Indeed, despite the thin film presence, the level of the deepest valleys detected in the right region of the AFM profile seems much lower than the untreated PP level thus suggesting the presence of competitive ablation process during the plasma treatment. Moreover, the higher gas temperatures lead to a larger ΔY value (≈ 0.8 μm) respect the case without precursor (≈ 0.48 μm) presented in Figure 2.17.

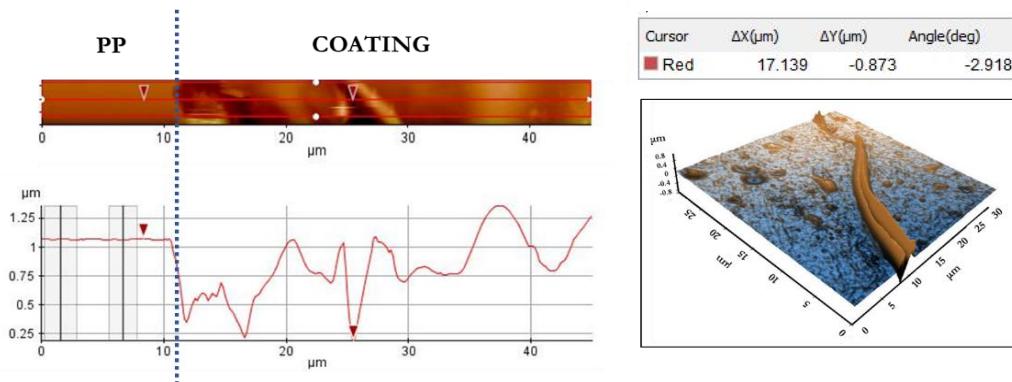


Figure 2.19- AFM results of the 12 kV-12 kHz ppTEOS thin film

On the other hand, the thin films thickness profile obtained at lower operating conditions (6 kV-12 kHz) for 60 seconds of deposition time is presented in **Figure 2.20**. Also in this case the occurrence of strong heating-up phenomena could affect the thickness value measured ($0.115 \pm 0.04 \mu\text{m}$) and, accordingly, the real thickness of the films could be slightly greater of the one measured by AFM. Moreover, taking into account ATR-FTIR results which reveal a thin film thickness increase by increasing the power applied, it is possible to assume a thickness value higher than $0.115 \mu\text{m}$ in case of thin film deposited at a higher operating condition.

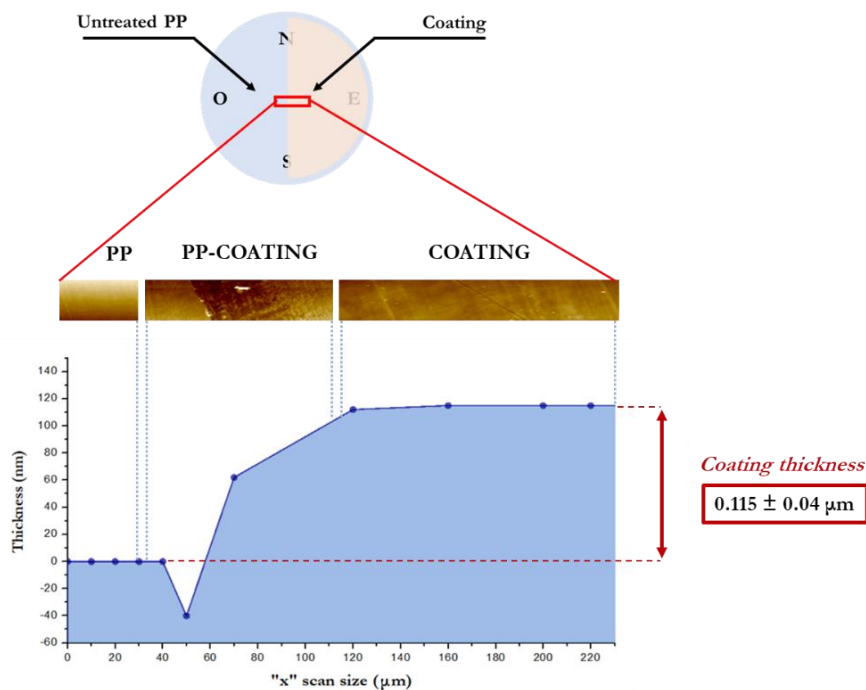


Figure 2.20 - Thickness profile of the 6 kV-12 kHz ppTEOS thin film

The morphological uniformity of deposits and the possible presence of defects have been then analysed by Scanning electron microscopy (SEM) analysis. From top-view SEM images, shown in **Figure 2.21**, it is clear that different values of applied power lead to completely different thin film morphological structures. In particular, the image acquired

in the center of the 12 kV-12 kHz sample (Figure 2.21(A)) highlights a quite smooth surface with several defects, while Figure 2.21(C) shows the presence of small agglomerates on the 6 kV-12 kHz sample surface, thus confirming the previous assumptions of a lower degree of dissociation. By comparing the images acquired on the center (Figure 2.21(A-C)) and the edge (Figure 2.21(B-D)) of the samples it is possible to deduce that the deposits are not perfectly uniform also in terms of morphological structure, in accordance with the chemical consideration discussed above. Moreover, SEM analysis performed on thin films deposited at 8 kV-12 kHz and 10 kV-12 kHz (not presented in this dissertation) show a smooth surface with cracks, so a morphological structure similar to the 12 kV-12 kHz case.

In case of deposition on polymeric substrate high processing temperature may result in crack formation, thereby hampering industrial applicability of the films. In fact, as demonstrated by J. Petersen in case of silica layers deposited on PEN foils, cracks can appear on thin film surfaces due to the thermal stress and the consequent stretching of the polymeric substrate during the deposition process. [30] This problem, which occurs for all cases except the lowest operating condition tested, is the most difficult barrier to overcome and is deeply discussed in the following section.

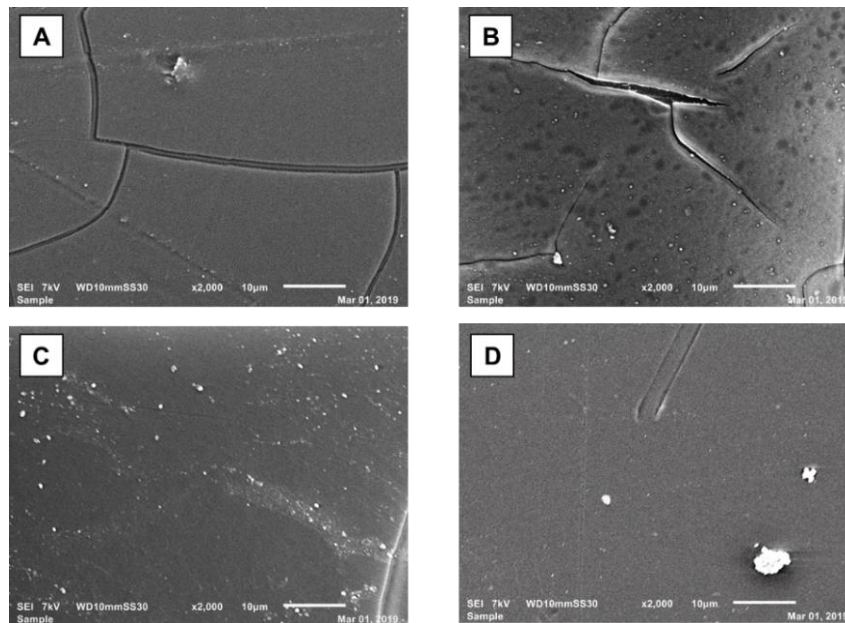


Figure 2.21 – Top-view SEM pictures of ppTEOS thin films at different operating conditions (2000x magnification)

2.2.3 Substrate temperature

The process temperature has a strong influence not only on the polymeric target thermal stress but also on the kinetics of gas-phase reactions, the in-flight particles nucleation and the carbon removal efficacy. Therefore, one of the crucial challenges of the plasma community is to minimise the thermal stress caused by the treatment by preserving the most significant monomer fragmentation pathways or surface reaction mechanisms able to produce Si-based thin films with a low content of organic groups. In this regard, before studying the dominant gas-phase processes by OES, LIF and Rayleigh scattering techniques, it is important to find out the optimal substrate temperature required for the

deposition of defect-free thin films. It is worth mentioning that such substrate temperature will be then correlated to the process gas temperature measured by two different techniques in the following chapter.

Surface temperature analysis on ppTEOS thin films have been performed with a Fluke TIS20 9HZ Thermal Infrared Camera. The Software SmartView 4.3, which allows to calculate the temperature distribution from the generated 2D images, was used for result processing. All the measurements were performed during the deposition process by keeping the IR camera, positioned at 45° respect to the normal of the thin film surface, 30 cm far from the sample. In **Figure 2.22** is presented an example of 2D image acquired during the deposition process.

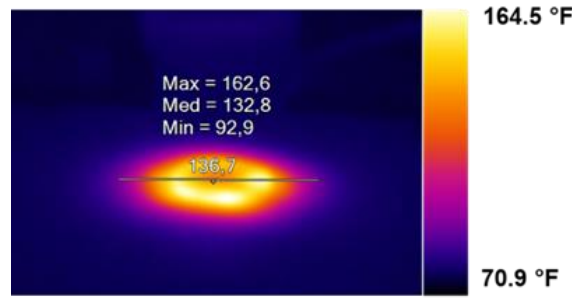


Figure 2.22- 2D map of the substrate temperature after 60 sec of deposition time

Figure 2.21 highlights that the thin films surface is completely free from cracks only when the lowest operating conditions (6 kV-12 kHz) are applied. In order to correlate such defects appearance with the thermal stress of the PP foil, substrate temperature measurements were performed by varying the power applied. As shown in **Figure 2.23** the substrate temperature in low power conditions is more or less equal to 37 °C after 60 seconds of plasma treatment while is more than 70 °C under maximum power conditions. Concerning the other operating conditions (8 kV-12 kHz / 10 kV-12 kHz), the substrate temperatures detected are in both cases over 50 °C after 60 seconds of plasma treatment; accordingly, the PP foil temperature must be maintained below 50°C in order to avoid cracks formation. In each case the temperature gradually increases by increasing the deposition time. In general, these results, which confirm the impact of the thermal stress on the presence of surface defects, can be explained by considering the difference in terms of linear thermal expansion coefficient (α) between the 0.5 mm-thick PP target ($\alpha_s (T_{amb}) = 120 \times 10^{-6} K^{-1}$) and the ppTEOS thin film ($\alpha_c (T_{amb}) = 0.65 \times 10^{-6} K^{-1}$, by assuming a coating of pure silica). The huge difference in terms of linear thermal expansion coefficient leads to an increase in terms of thermal stress (σ_t) in response to a substrate temperature change during the deposition process as proven by the follow Equation [31]:

$$\sigma_t = \frac{E_c}{1-\mu_c} \int_{T_i}^{T_f} \{\alpha_s(T) - \alpha_c(T)\} dT \quad (2.3)$$

where E_c (1-1.6 GPa) and μ_c (~ 0.4) are the Young modulus and the Poisson coefficient of the coating while T_i and T_f are the initial and the final temperature respectively.

To sum up, there are only two possible ways for the obtainment of Si-based thin films with good performances in case of static configuration: the use of shorter deposition times, which is the best solution for industrial applications, or the employment of minimum power

conditions since the thin films chemical structure does not seem significantly affected by the power density applied, as proven in the previous sections. Other improvements are expected from moving the plasma source during the deposition treatment or, if permitted, from employing polymeric substrates with improved thermomechanical resistance.

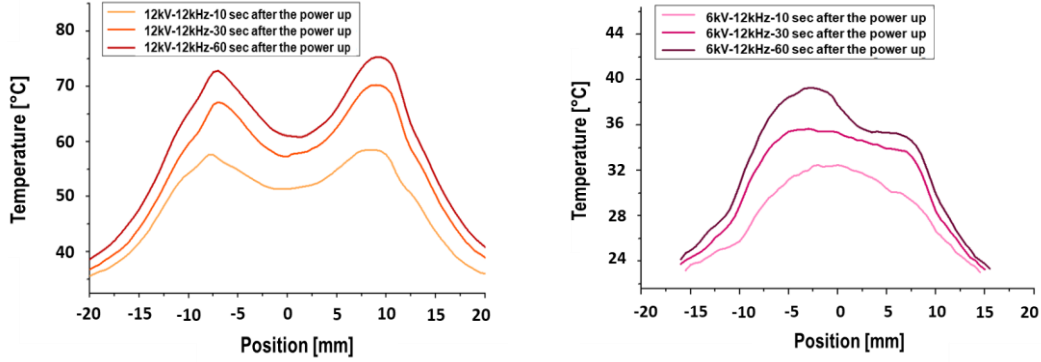
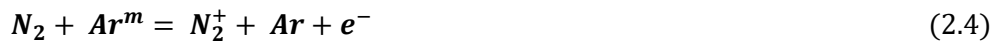


Figure 2.23 – Substrate temperature profiles along the central axis of the PP samples at different deposition times

The substrate temperature profile along the central axis of the PP samples are reported in Figure 2.23. Under high power conditions the surface temperature seems to be higher in correspondence of the edge of the sample (± 13 mm) respect the central zone (± 5 mm) thus generating a “donut shape” behaviour. This expected result is a direct consequence of the “ring shape” gas temperature behaviour, a phenomenon extensively discussed in the work of X. Lu [32] strictly connected to Penning ionization processes which typically occurs in case of APPJ working in ambient air. All the results reported in the above-mentioned scientific review proves that the ambient air diffusion into the plasma discharge increase the gas temperature due to Penning ionization reactions between N_2 molecules and Ar metastable atoms:



This effect is less pronounced in the 6 kV-12 kHz case probably due to the different ambient air mixture caused by a different discharge evolution between the electrodes as showed in Figure 2.3.

As mentioned before, an improvement in terms of substrate temperature could affect also the chemical composition of the deposits by reducing the amount of carbon content. However, by comparing the spatial distribution in terms of carbon atoms percentage, detected by high-resolution XPS analysis (Figure 2.14), and the substrate temperature profile along the central axis of the PP sample (Figure 2.23), it is evident that in our case the substrate temperature does not have a key role in the carbon removal and all the difference in terms of chemical bonds are probably connected to the admixture of oxygen molecules from the ambient air .

2.3 Conclusions

The effect of power density and gas flow mixture on chemical and morphological ppTEOS thin film properties is studied in detail by FTIR, XPS, AFM and SEM analysis. Unexpectedly, it was established that the chemical structure of thin films obtained under different conditions in terms of energy supplied per unit of monomer remains unchanged in contrast to experimental results reported by Morent in case of ppHMDSO thin films on the basis of the Yasuda factor effect. On the other hand, the morphological structure of ppTEOS thin films, obtained under different voltage conditions, seems significantly different and in good agreement with literature results. Moreover, SEM analysis as well as substrate temperature measurements performed by means of an IR camera were used to reveal the maximum substrate temperature acceptable (40 °C) in order to avoid cracks formations.

Despite the good results obtained in terms of roughness and chemical composition under the strongest operating conditions (12 kV-12 kHz), it was concluded that 6 kV-12 kHz is the best operating condition for the achievement silica-like thin films completely free from defects. However, considering the almost identical chemical structure, huge differences in terms of gas-phase fragmentation mechanisms between the two cases are unexpected.

In general, this chapter highlights the importance of a poly-diagnostic approach for thin films characterization, since the informations obtained by means of a single technique could provide misleading results and could not be enough for an exhaustive thin films surface characterization. Each surface techniques used in the current study has provided a small but crucial step towards an in-depth understanding of the thin film structure.

2.4 References

- [1] O. V Penkov, M. Khadem, W. S. Lim, and D. E. Kim, "A review of recent applications of atmospheric pressure plasma jets for materials processing," *J. Coatings Technol. Res.*, vol. 12, no. 2, pp. 225–235, 2015.
- [2] T. C. Tsai and D. Staack, "Low-temperature polymer deposition in ambient air using a floating-electrode dielectric barrier discharge jet," *Plasma Process. Polym.*, vol. 8, no. 6, pp. 523–534, 2011.
- [3] F. Barletta, A. Liguori, C. Leys, V. Colombo, M. Gherardi, and A. Nikiforov, "Novel method for NH-rich coatings engineering by means of aerosol assisted atmospheric pressure plasma deposition," *Mater. Lett.*, vol. 214, pp. 76–79, 2018.
- [4] X. Lu, M. Laroussi, and V. Puech, "On atmospheric-pressure non-equilibrium plasma jets and plasma bullets," *Plasma Sources Sci. Technol.*, vol. 21, no. 3, 2012.
- [5] M. Laroussi and T. Akan, "Arc-free atmospheric pressure cold plasma jets: A review," *Plasma Processes and Polymers*, vol. 4, no. 9, pp. 777–788, 2007.
- [6] J. Schäfer, R. Foest, A. Quade, A. Ohl, J. Meichsner, and K. D. Weltmann, "Carbon-free SiO_x films deposited from octamethylcyclotetrasiloxane (OMCTS) by an atmospheric pressure plasma jet (APPJ)," *Eur. Phys. J. D*, vol. 54, no. 2, pp. 211–217, 2009.
- [7] R. Reuter, K. Rugner, D. Ellerweg, T. De Los Arcos, A. Von Keudell, and J.

- Benedikt, "The role of oxygen and surface reactions in the deposition of silicon oxide like films from HMDSO at atmospheric pressure," *Plasma Process. Polym.*, vol. 9, no. 11–12, pp. 1116–1124, 2012.
- [8] F. Massines, C. Sarra-Bournet, F. Fanelli, N. Naudé, and N. Gherardi, "Atmospheric pressure low temperature direct plasma technology: Status and challenges for thin film deposition," *Plasma Processes and Polymers*, vol. 9, no. 11–12. pp. 1041–1073, 2012.
- [9] A. Liguori *et al.*, "Deposition of Plasma-Polymerized Polyacrylic Acid Coatings by a Non-Equilibrium Atmospheric Pressure Nanopulsed Plasma Jet," *Plasma Process. Polym.*, vol. 13, no. 3, pp. 375–386, 2016.
- [10] A. Liguori *et al.*, "Co-Deposition of Plasma-Polymerized Polyacrylic Acid and Silver Nanoparticles for the Production of Nanocomposite Coatings Using a Non-Equilibrium Atmospheric Pressure Plasma Jet," *Plasma Process. Polym.*, vol. 13, no. 6, pp. 623–632, 2016.
- [11] M. Boselli *et al.*, "Schlieren high-speed imaging of a nanosecond pulsed atmospheric pressure non-equilibrium plasma jet," *Plasma Chem. Plasma Process.*, vol. 34, no. 4, pp. 853–869, 2014.
- [12] A. Liguori *et al.*, "Synthesis of Copper-Based Nanostructures in Liquid Environments by Means of a Non-equilibrium Atmospheric Pressure Nanopulsed Plasma Jet Synthesis of Copper - Based Nanostructures in Liquid Environments by Means of a Non - equilibrium Atmospheric Pressure," *Plasma Chem. Plasma Process.*, vol. 38, no. 6, pp. 1209–1222, 2018.
- [13] G. Laroche, J. Fitremann, and N. Gherardi, "Applied Surface Science FTIR-ATR spectroscopy in thin film studies : The importance of sampling depth and deposition substrate," *Appl. Surf. Sci.*, vol. 273, pp. 632–637, 2013.
- [14] M. Milosevic, "Internal reflection and ATR spectroscopy," *Appl. Spectrosc. Rev.*, vol. 39, no. 3, pp. 365–384, 2004.
- [15] C. Berthomieu, C. B. Ae, and R. Hienerwadel, "Fourier transform infrared (FTIR) spectroscopy," *Photosynth. Res.*, vol. 101, no. July 2009, pp. 157–170, 2009.
- [16] D. A. Jaeger, "Interface Investigations on Titanium Nitride Bilayer Systems," *Phd*, vol. 5509, 2012.
- [17] F. Benitez, "Functional properties and applications of plasma polymerized hexamehtyldisiloxane (ppHMDSO) thin films," 2015.
- [18] H. Konno, *Chapter 8 - X-ray Photoelectron Spectroscopy*. Tsinghua University Press Limited, 2016.
- [19] G. Friedbacher, "Atomic Force Microscopy (AFM)," pp. 443–464, 2011.
- [20] R. R. L. De, D. A. C. Albuquerque, T. G. S. Cruz, F. M. Yamaji, and F. L. Leite, "Measurement of the Nanoscale Roughness by Atomic Force Microscopy: Basic Principles and Applications," in *Atomic Force Microscopy - Imaging, Measuring and Manipulating Surfaces at the Atomic Scale*, 2012.
- [21] B. J. Inkson, "Scanning Electron Microscopy (SEM) and Transmission Electron Microscopy (TEM) for Materials Characterization," in *Materials Characterization Using Nondestructive Evaluation (NDE) Methods*, Elsevier Ltd, 2016, pp. 17–43.
- [22] S. A. Starostin, M. Creatore, J. B. Bouwstra, M. C. M. Van De Sanden, and H. W. De Vries, "Towards roll-to-roll deposition of high quality moisture barrier films on polymers by atmospheric pressure plasma assisted process," *Plasma Process. Polym.*, vol. 12, no. 6, pp. 545–554, 2015.
- [23] C. T. Kirk, "Quantitative analysis of the effect of disorder-induced mode coupling,"

Physcal Rev. B, vol. 38, no. 2, p. 1255, 1988.

- [24] I. P. Lisovskii, V. G. Litovchenko, V. G. Lozinskii, and G. I. Steblovskii, “IR spectroscopic investigation of SiO₂ film structure,” *Thin Solid Films*, vol. 213, no. 2, pp. 164–169, 1992.
- [25] J. Ružbarský and A. Panda, “Plasma jet,” in *SpringerBriefs in Applied Sciences and Technology*, vol. 10, no. 9783319462721, 2017, pp. 1–12.
- [26] M. Abbasi-firouzjah, S. Hosseini, M. Shariat, and B. Shokri, “The effect of TEOS plasma parameters on the silicon dioxide deposition mechanisms,” *J. Non. Cryst. Solids*, vol. 368, pp. 86–92, 2013.
- [27] S. E. Babayan, J. Y. Jeong, V. J. Tu, J. Park, G. S. Selwyn, and R. F. Hicks, “Deposition of silicon dioxide films with an atmospheric-pressure plasma jet,” vol. 7, pp. 286–288, 1998.
- [28] Y. Liu, S. Welzel, S. A. Starostin, M. C. M. Van De Sanden, R. Engeln, and H. W. De Vries, “Infrared gas phase study on plasma-polymer interactions in high-current diffuse dielectric barrier discharge,” *J. Appl. Phys.*, vol. 121, no. 24, 2017.
- [29] K. G. Kostov, T. M. C. Nishime, L. R. O. Hein, and A. Toth, “Surface & Coatings Technology Study of polypropylene surface modification by air dielectric barrier discharge operated at two different frequencies,” *Surf. Coat. Technol.*, vol. 234, pp. 60–66, 2013.
- [30] J. Petersen, J. Bardon, A. Dinia, D. Ruch, and N. Gherardi, “Organosilicon coatings deposited in atmospheric pressure townsend discharge for gas barrier purpose: Effect of substrate temperature on structure and properties,” *ACS Appl. Mater. Interfaces*, vol. 4, no. 11, pp. 5872–5882, 2012.
- [31] Y. Leterrier, “Durability of nanosized oxygen-barrier coatings on polymers,” *Progress in Materials Science*, vol. 48, no. 1. pp. 1–55, 2003.

3

INSIGHTS OF Ar/TEOS GAS-PHASE PROCESSES: EXCITED-STATE SPECIES

As reported in the introductory chapter, the lack of clarity related to the dominant gas-phase reactions and the complete absence of reference data about monomer fragmentation pathways in case of Ar/TEOS plasma atmospheric deposition is currently one of the main barriers to an adequate control over the process and coatings properties.

As a first step towards a detailed study of gas-phase processes having a key role in thin films features definition, the use of integrated time- and space-resolved discharge diagnostics is strongly demanded. Up to now, most of research has been performed with the use of optical emission spectroscopy (OES), mainly due to its non-intrusiveness as well as its easy setup features.[1],[2] Even if OES provides information about the excited plasma species and the density of emitters in plasma is much lower than the density of species in the ground state, the use of such diagnostic technique is an important first step in order to clarify the most significant excited species production mechanisms.[3],[4]

In this chapter the TEOS influence on the plasma gas temperature, electron density and spatial-temporal behavior of excited species in an Ar/TEOS atmospheric pressure plasma jet is investigated. High resolution spectra of the OH(A-X), N₂(C-B) and CH(A-X) emission bands have been used for rotational temperature measurements and the conditions for which these temperatures can be assumed equal to the gas temperature (T_{gas}) in case of an Ar/TEOS mixture are discussed. The applicability of the Rayleigh scattering method for T_{gas} measurements during a deposition process is further analyzed and the time- and space- resolved behavior of the excited species have been used to discuss possible mechanisms involved in the excited states generation.

In view of the surface results reported in Chapter 2, which highlight similar thin film chemical structures under different energies per unit of monomer, the fundamental gas-phase study presented in the following sections reports only the most significant results achieved at fixed operating conditions. For simplicity's sake, the highest power input conditions have been selected in order to maximise the emission signal. It's important to highlight that OES results obtained for the case of the lowest operating conditions differ from high-power results only in terms of signal

intensity without providing any additional informations about excited species production mechanisms.

3.1 MATERIALS and METHODS

The plasma deposition system used for the gas-phase study is the same previously employed for thin films deposition purposes presented in Fig. 2.1 (chapter 2). In the experiments here reported, the input power has been kept constant at 11.5 W (12 kV-12 kHz) with a carrier gas flow equal to 65 ml/min; the gap between the HV electrode and the dielectric plate has been fixed at 15 mm.

The filamentary Ar and Ar/TEOS plasma discharges, shown in **Figure 3.1(A)** and 3.1(B) respectively, are sustained in ambient air, so the air back diffusion has to be taken into account in the analysis of obtained results.

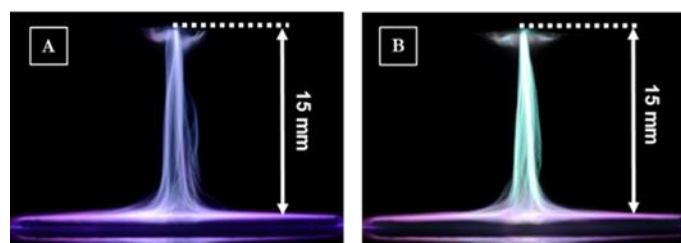


Figure 3.1 - Plasma discharge in Ar (A) or Ar/TEOS mixture (B) (no optical filtering)

3.1.1 OES and fast imaging set-up

A schematic view of the set-up used in this work is shown in **Figure 3.2**. The OES measurements were performed along the discharge axis at 7.5 mm from the APPJ head ($y=0$) using an Andor Shamrock-750 spectrometer equipped with a 1800 or 3600 gr mm^{-1} diffraction grating and an Andor iStar 740 intensified charge coupled device (ICCD) camera used as a detector. The plasma emission was guided to the spectrometer by a UV-VIS optical fiber. The wide range spectra were measured with a resolution of 0.05 nm FWHM (full width at half maximum), while time-resolved spectra were recorded with a resolution of 0.03 nm except for the case of H_{α} lines used for electron density calculation (0.048 nm). In all cases, time-resolved OES spectra have been acquired with a time step of 1 μs .

The ICCD camera, equipped with a CERCO 100mm $f/2.8$ UV lens transparent in 220-900 nm range, was also used to capture time-resolved 2D OES images by applying five different band pass filters with the central wavelength at 696, 780, 340, 309 and 430 nm in order to detect Ar, O, N_2 , OH and CH emission lines/bands, respectively. Single shot CH and OH images have been obtained with a gate time of 1 μs while 5 μs have been used in the O atom case (due to low intensity). Radiation patterns of Ar I and N_2^* have been acquired at 2 μs of the gate time. The ICCD camera was synchronized with the AC generator by means of a Stanford Research DG645 digital delay generator and a TTL signal generator (represented as synchronization unit in Figure 3.2). The time delay (starting from the positive

voltage peak) was set at 2, 22 and 42 μs to reflect the discharge appearance during the positive and negative voltage half cycles, as well as between the peaks.

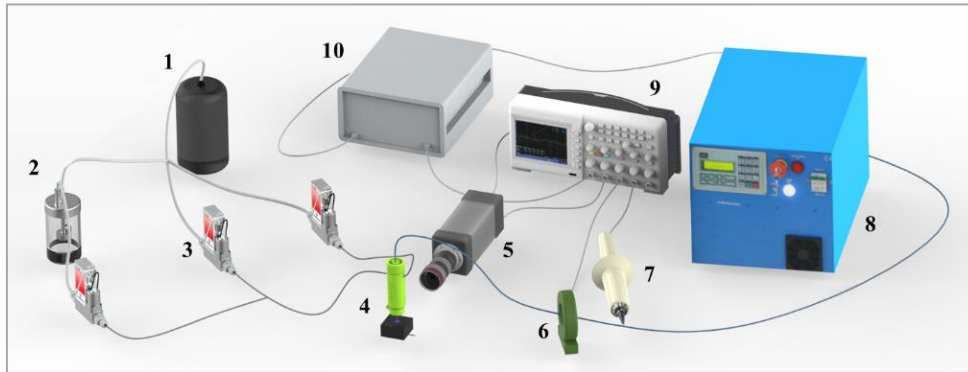


Figure 3.2 - Layout of the plasma deposition set-up: Ar supply (1), bubbling system (2), digital mass flow controller (3), plasma source (4), ICCD camera (5), current probe (6), voltage probe (7), HV generator (8), oscilloscope (9), synchronization unit (10)

3.1.2 Gas temperature and electron density measurements

One of the most widespread methods for gas temperature (T_{gas}) measurements is the calculation of rotational temperature (T_{rot}) of excited diatomic molecules assuming that $T_{\text{gas}} \approx T_{\text{rot}}$. In the atmospheric pressure plasmas, however, the rotational level population of rotational states is often characterized by a prominent non-Boltzmann shape. Thus, in these cases T_{rot} only reflects formation of the specific excited states, not giving a reliable solution for gas temperature.[5],[6] In this respect, various simulation software, such as Lifbase, are based on the assumption that rotational states are Boltzmann-distributed and, as a consequence, a careful results analysis is strongly required. In the current work rotational temperatures of the excited OH(A), $\text{N}_2(\text{C})$ and CH(A) states are determined by using two different software. Regarding the rotational temperature of OH(A) state, it is known that only rotational states with small rotational numbers allow a reliable estimate of the gas temperature.[7] For this reason, T_{rot} of OH radicals was obtained using MassiveOES software which calculates T_{gas} taking into account only rotational states with $J < 9$. These measurements were performed with and without precursor in order to verify how its presence affects T_{gas} . On the other hand, T_{rot} of N_2 and CH excited molecules were determined by fitting method using the Lifbase software in a single T_{rot} approximation.

Numerous research groups have estimated T_{gas} from the rotational temperature of OH and N_2 excited states for different high-pressure plasmas so far. Bruggeman [8] has shown that, in case of DC-excited discharges generated in water, OH cannot be used as a good estimate of T_{gas} as high H_2O density leading to a significant overestimation with respect to the values obtained with the $\text{N}_2(\text{C-B})$ band. In addition, a similar study performed by Nikiforov [7] using an APPJ generated in Ar/water mixtures has proven that the T_{rot} of N_2 molecules is much higher than the expected temperature while T_{gas} is equivalent to the temperature determined by the first slope of the Boltzmann plot of OH radicals. In this work the same issue has been checked

also in case of Ar/TEOS mixture in order to identify which of the two chosen molecules provides the best estimation for T_{gas} .

Considering TEOS fragmentation, accompanied by CH radical formation, T_{gas} measurements via high-resolution CH emission spectra are discussed in this paper for the first time. Although CH radicals are common byproducts during the atmospheric pressure deposition of organosilicon precursors and CH band emission intensity is commonly used for estimation of the conversion rate towards Si-based thin films, the appearance of a distorted rotational distribution is very likely a result of complex CH formation process in Ar plasmas.[9] Proper analysis of CH emission can provide a convenient way to control deposition processes through the T_{rot} (CH) estimation and clarify the excitation mechanisms in the presence of TEOS in general.

It is known that precursor fragmentation strongly depends on plasma properties, such as the ionization degree. For electron density measurements under the atmospheric pressure, Stark broadening of the hydrogen or hydrogen-like atomic spectral lines is the most widely used method.[8],[10] In this work, a time-resolved H_α has been used to obtain the electron density evolution during the positive and negative voltage peaks for a case of Ar/TEOS APPJ. As known, in the case of atmospheric discharges, the experimentally measured H_α line broadening represents convolution of different broadening mechanisms (corresponding to either Gaussian or Lorentzian lineshapes). The Stark broadening estimation formula in this case is well known, as described in the previous works.[11],[12] It is important, however, to highlight that in the case of APPJs the natural and resonance broadening contributions are almost negligible as reported in the critical review of Nikiforov *et al.*[10] Doppler broadening, on the other hand, has been estimated in our case to be rather low as well (about 1.3 pm), which cannot affect considerably electron density calculation. Consequently, all broadening mechanisms with a Gaussian profile were neglected in this work and only a convolution of several Lorentzian profiles was taken into account:

$$\Delta\lambda_{\text{exp}} [\text{nm}] \cong \Delta\lambda_s + \Delta\lambda_{\text{vdw}} + \Delta\lambda_{\text{ins}} \quad (3.1)$$

where $\Delta\lambda_s$, $\Delta\lambda_{\text{vdw}}$ and $\Delta\lambda_{\text{ins}}$ are the FWHM of Stark, Van der Waals and instrumental broadening respectively. $\Delta\lambda_{\text{ins}} = 0.048$ nm in our case (measured by an Hg line in a low-temperature plasma source). For $\Delta\lambda_{\text{vdw}}$ calculation, the formula suggested by S. Hofmann *et al.* was used.[13] Lastly, electron density values were calculated as function of $\Delta\lambda_s$ using the data tabulated by M. A. Gigos *et al.* in case of H_α line.[14]

3.1.3 Rayleigh scattering experiment

The experimental set-up used in this study for Rayleigh scattering measurements is shown in **Figure 3.3**. As described in the previous works [15],[16], this active spectroscopic method is typically used for gas temperature measurement, as the Rayleigh scattering signal (I) is proportional to the density of heavy scattered particles (n^i) which is in turn inversely proportional to the T_{gas} value at a constant pressure (p), as defined by the ideal gas law:

$$I \sim \sum_i \sigma^i n^i = \sum_i \sigma^i \frac{p}{T_g k_B} \quad (3.2)$$

where k_B is the Boltzmann constant and σ^i is the Rayleigh scattering cross section of heavy species at 532 nm.[17] Although in our case the APPJ works in ambient air, the Rayleigh scattering signal can be considered independent from the percentage of air in the gas mixture since the scattering cross sections of Ar ($5.4 \times 10^{-32} \text{ m}^2$), N₂ ($6.2 \times 10^{-32} \text{ m}^2$) and O₂ ($5.3 \times 10^{-32} \text{ m}^2$) are all comparable.[18] By using the relation $T_{gas} I = T_{ref} I_{ref}$, it is possible to deduce T_{gas} in the plasma area from the Rayleigh scattering signal (I) and a reference measurement (I_{ref}) obtained with the Ar gas flow on and the plasma discharge off at a known ambient gas temperature ($T_{ref} = T_{amb}$). Correspondingly, laser scattering method suits well for validation of the emission spectroscopy results, namely the T_{rot} values obtained using OH, CH and N₂ excited states.

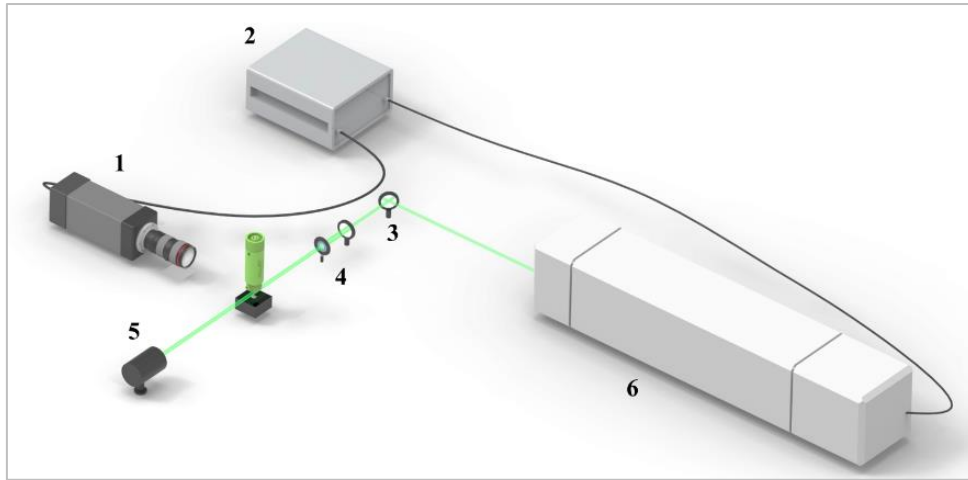


Figure 3.3 - Rayleigh scattering spectroscopy set-up including: ICCD camera (1), synchronization unit (2), prism (3), sheet forming optics (4), beam dump (5), Nd:YAG laser at 532 nm (6)

In our experiments, the laser scattering measurements were done by using a pulsed Nd:YAG laser (Litron nano-S), operating at 532 nm with a pulse energy of 8 mJ, a repetition rate of 10 Hz and 8 ns of pulse duration. The scattered light is collected, perpendicularly to the laser beam, by a fast imaging gated Hamamatsu digital camera with a 532 nm filter ($\Delta\lambda_{FWHM}=10 \text{ nm}$) and 500 ns of exposure time in order to obtain a superior image quality and compensate jitter. The set-up used to synchronize the ICCD camera with laser is similar to the one used for time-resolved OES measurement. For all T_{gas} measurements the laser beam, characterized by size $8 \text{ mm} \times 0.1 \text{ mm}$, was passing through the plasma discharge at a distance of 7.5 mm from the gas outlet in order to avoid the beam reflection from either the dielectric plate or the APPJ head. The Rayleigh scattering method has higher sensitivity compared to the rotational analysis resulting in T_{gas} accuracy of $\pm 15 \text{ K}$.

3.2 RESULTS and DISCUSSION

3.2.1 Emission spectra analysis and T_{gas} measurements

TEOS Injection in the discharge region does not drastically perturb the emission spectrum (compared to the pure Ar discharge case), as shown in **Figure 3.4**. For the sake of clarity, the low-resolution spectrum here is divided in two wide spectral ranges (300–670 and 690–850 nm), by using an exposure time of 200 ms and 5 ms respectively. Most of the emission lines located between 690 and 850 nm (Figure 3.4(B)), corresponding to the Ar $4p \rightarrow 4s$ transitions, are characteristic of atmospheric pressure Ar plasma; while a significant emission from the nitrogen second positive system ($N_2(C-B)$) and hydroxyl radicals (OH (A-X)) band are observed between 300 and 650 nm (Figure 3.4(A)), due to the presence of surrounding air and water vapor traces.[19] Moreover, the addition of TEOS leads to the appearance of the CH, CN and C_2 emission bands, as a result of its fragmentation by electron impact or Ar metastable collisional processes.[20] The detailed line and rotational band assignments for the mentioned atoms and molecules are given in **Table 3.1**.

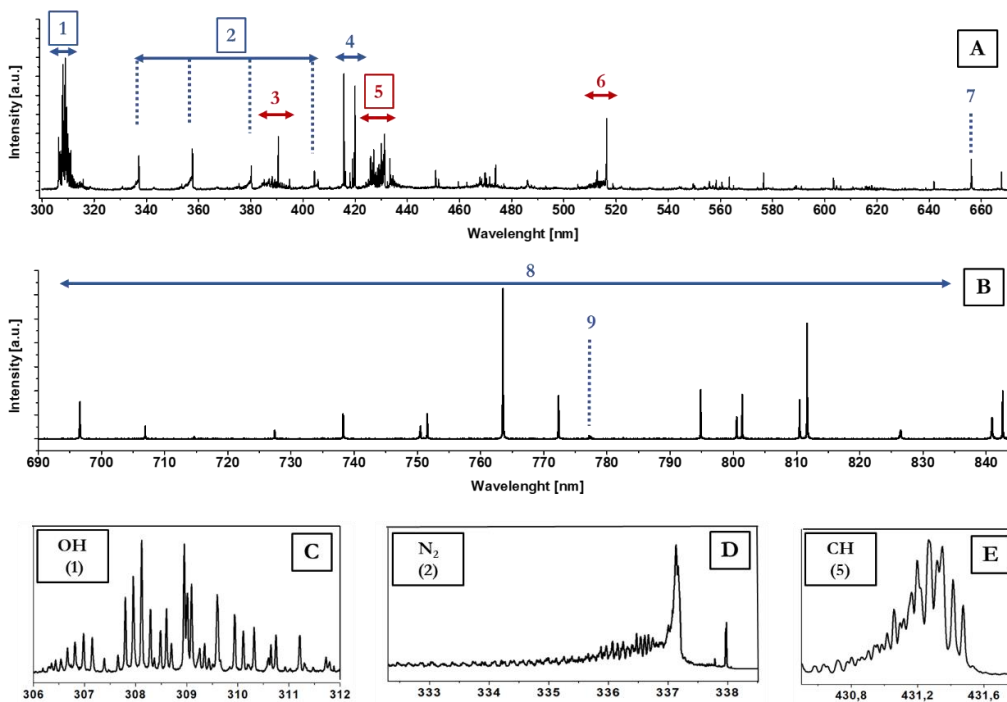


Figure 3.4 - Overview and high resolution spectra in Ar/TEOS mixture: (A) 300-650 nm, (B) 690-840 nm, (C) 306-312 nm \rightarrow OH(A-X), (D) 332-338 nm \rightarrow N₂(C-B), (E) 430-432 nm \rightarrow CH(A-X) measured at the negative voltage peak at 42 μ s time delay

Table 3.1- Detailed spectra assignments in Ar/TEOS mixture

n.	Species	Transition	λ [nm]
1	OH	$A^2\Sigma^+ \rightarrow X^2\Pi$	308.9
2	N ₂	$C^3\Pi_u \rightarrow B^3\Pi_g$	337.1
3	CH CN	$B^2\Delta \rightarrow X^2\Pi$ $B^2\Sigma \rightarrow X^2\Sigma$	388.9 386.2, 387.1
4	Ar I	$3p_5 \rightarrow 1s_4$ $3p_9 \rightarrow 1s_5$	419.83 420.06
5	CH	$A^2\Delta \rightarrow X^2\Pi$	431.3
6	C ₂	$d^3\Pi_g - a^3\Pi_u$	518.0
7	H _{α}	2p -3d	656.28
8	Ar I	$2p_2 \rightarrow 1s_5$ $2p_1 \rightarrow 1s_2$ $2p_6 \rightarrow 1s_5$ $2p_2 \rightarrow 1s_3$ $2p_4 \rightarrow 1s_3$ $2p_9 \rightarrow 1s_5$	696.54 751.46 763.51 772.42 794.81 826.45
9	O I	$3p \rightarrow 3s$	777.41

Among various physical plasma properties, gas temperature is one of the key parameters for an adequate control of the deposition process. Apart from having a strong influence on the kinetics of gas-phase reactions and in-flight particle nucleation, T_{gas} has a central role in the definition of thin film properties. As demonstrated in several studies, in case of deposition on polymeric substrates high processing temperature may result in severe morphological defects, such as crack formation, thereby hampering industrial applicability of the films.[21] Thus, this key parameter should be carefully controlled to maintain an appropriate temperature of the heat-sensitive surfaces.

In order to address this point, two different spectroscopic methods for T_{gas} measurement have been applied. As a first step, OES has been used for rotational temperature calculation of the OH $A^2\Sigma^+ \rightarrow X^2\Pi_i$ (0,0), N₂ $C^3\Pi_u \rightarrow B^3\Pi_g$ (0,2) and CH $A^2\Delta \rightarrow X^2\Pi$ (0,0) molecular emission bands. The OH, N₂, CH high resolution spectra acquired at the negative voltage peak (42 μ s) in Ar/TEOS mixture are reported in Figure 5 and results of measurements are summarized in **Table 3.2**. As expected, taking into account the low percentage of TEOS introduced as well as the measurement accuracy, the precursor injection has non-significant impact on T_{rot} of the abovementioned N₂ and OH molecules. On the other hand, from Table 3.2 it is clear that T_{rot} obtained using N₂ and CH bands (~550-590 K) are considerably higher than the value estimated from OH transition (~ 410 K).

Table 3.2 - OH, N₂ and CH rotational temperature mean values calculated in Ar or Ar/TEOS mixture by using 0.03 nm of spectral resolution

Primary gas flow	Excited species	T _{rot} [K]
Ar	OH (A-X)	382 ± 50
Ar	N ₂ (C-B)	549 ± 50
Ar/TEOS	OH (A-X)	409.7 ± 50
Ar/TEOS	N ₂ (C-B)	551.6 ± 50
Ar/TEOS	CH (A-X)	590 ± 50

These experimental results corroborate with several previous studies claiming overestimation of T_{gas} obtained by N₂ emission bands in the case of Ar plasma generated in ambient air, due to the presence of Ar metastables (Ar^m) leading to production of N₂(C) excited molecules by a quasi-resonance process (see Equation 3.6 in section 3.2.3).[7]

The T_{rot} results obtained with CH band are very similar to those obtained with N₂ contradicting at the same time to the OH-based T_{rot} values. Since the use of CH emission for T_{gas} estimation has never been discussed for atmospheric pressure deposition processes with TEOS as precursor, further efforts are required to understand the observed disagreement. It is well known that the rotational distribution of excited diatomic molecules formed by direct electron impact from the respective ground state normally correspond to rotational distribution in the ground state.[6] Nevertheless, the presence of TEOS-related dissociation reactions, electron impact dissociative excitation and Penning reactions have to be taken into account in order to understand the pathways of CH radical formation and the resulting rotational distribution.

The simplified model for CH radical formation in our case is given in **Figure 3.5**. As reported by K. Okimura *et al.*[22], at electron energy below 8-9 eV, the first products of TEOS dissociation are most likely hydrocarbon fragments such as C₂H₄ and C₂H₅, while at energy around 15 eV (which exceeds the energy of Ar 1s₅ state), CH₃ and Si_x(C₂H₅O)_y stable fragments are the main products. Moreover, during the deposition process several ionized fragments, produced by dissociative ionization of TEOS molecules, can further affect the CH(A) radicals production. For example, as shown by Kawaguchi *et al.*[23], the highest partial ionization cross sections corresponding to SiO₄C₆H₁₅⁺ (8×10⁻¹⁶ cm²) and OC₂H₅⁺ (3×10⁻¹⁷ cm²) ionized fragment pathways require about 11-12 eV of electron energy, which is close to Ar^m energy level. Moreover, despite the absence of detailed information about products and rate coefficients in case of Ar^m-TEOS reactions, L. Le Brizoual [24] has shown that TEOS molecules quenches Ar metastable atoms about as fast as oxygen. Therefore, by assuming the same quenching rate constant reported by L.G.Piper [25] for Ar^m-O₂ collisions (2.1×10⁻¹⁰ cm² s⁻¹), it is possible to hypothesize a dominant role of Ar^m in TEOS dissociation processes due to very fast reaction kinetics.

Nevertheless, in general, it can be stated that the primary products of TEOS fragmentation induced by electron impact and collisions with Ar^m are the C₂ hydrocarbons and Si- containing fragments. These species can be further dissociated

contributing to CH(A) radicals production. Several authors have shown that C₂H₅ and C₂H₄ fragments can be in turn defragmented into CH, CH₂ and CH₃ radicals. For instance, the work of M. Steinbauer *et al.* reported that about 4.67 eV is required for dissociation of C₂H₅ to CH₃ (²A₂'') and CH₂ (³B₁'a₁), while only 1.57 eV is required for dissociation of C₂H₅ leading to C₂H₄ (X¹A_g) and H atoms.[26] The latter mechanism is a very probable dominant pathway in case of Ar-based plasma jets with mean electron energy of about 1 eV.[7] As a consequence, CH₃-CH radicals are likely the main products of TEOS fragmentation and the primary source of CH(A) radical production, visible in our OES spectra (see Figure 3.4).

In general, the CH(A) excited state can be populated by electron impact dissociative excitation of hydrocarbons, such as CH₃-CH, by high energy electrons (around 14 eV) or by direct excitation of previously dissociated ground state CH by low energy electrons.[27]

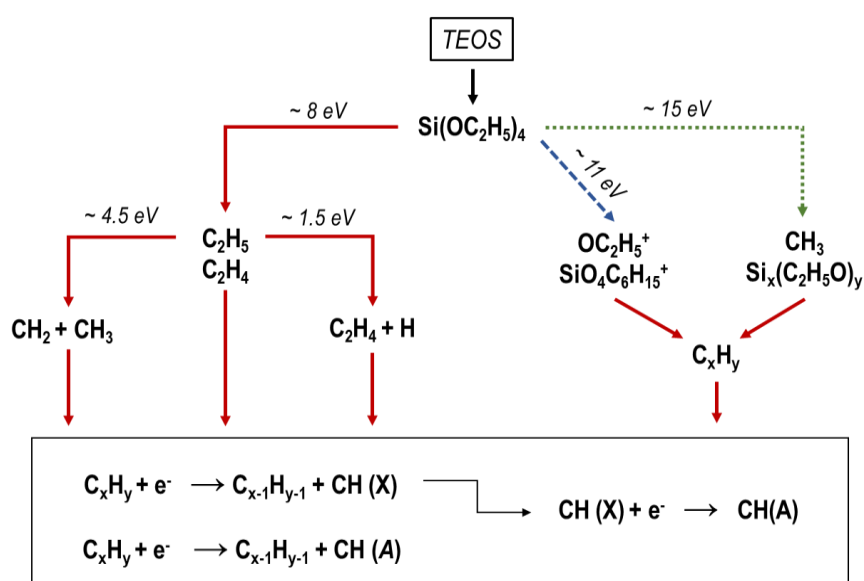


Figure 3.5 - Main formation pathways of CH(A) radicals; — electron impact dissociative reactions, --- Ar metastables collisions, dissociative reactions

Despite these suggestions, the exact mechanisms of CH₃-CH radicals defragmentation into CH(A) and CH(X) radicals in case of Ar/TEOS plasmas remain hidden. Assuming the C-C bond dissociation energy of about 3.6-3.9 eV and a required excitation energy of ~4-6 eV for CH(X) to CH(A) excitation, there is a large number of possible mechanisms which could influence the rotational distribution of CH(A) state through reactions with OH radicals, Ar^m and other excited particles.[28] Moreover, this distribution might also be non-thermal, resulting in considerably higher values of T_{rot} compared to those observed in our case. Unfortunately, the suggested non-Boltzmann distribution cannot be directly confirmed experimentally since the CH(A-X) spectra obtained in this work, even under maximum spectral resolution, possess a rather complex structure due to the partial overlap of the Q, R and P branches for rotational numbers J>9.

It is known that, for Ar plasma in a humid environment T_{rot} = T_{gas} in the case of OH band only if the lowest rotational levels are taken into account.[6] The presence of TEOS precursor in the gas phase, however, may strongly influence T_{rot} values and

TEOS dissociation itself have to be taken into account. In order to investigate this effect, T_{rot} obtained (using OH band) with and without precursor, has been analyzed. The temperature calculated from the OH spectrum in Ar is 382 ± 50 K which is in reasonable agreement with the results obtained for Ar/TEOS mixtures (see Table 3.2).

It is possible to assume $T_{\text{rot}}(\text{OH}) \approx T_{\text{gas}}$ also in the presence of low amount of precursor, as its dissociation does not affect generation and excitation of OH radicals due to very low concentration. Obviously, due to a strong discrepancy in between T_{rot} obtained with different emitting species, an independent measurement of the gas temperature by Rayleigh scattering technique is required for cross-validation. Rayleigh scattering, despite of its high accuracy, has its own limitations, e.g. interference with Mie-scattering signal in dust-containing plasmas[29], as shown in **Figure 3.6(B)** for the case of the actual deposition process. As a consequence, in case of Ar/TEOS mixture it is impossible to measure T_{gas} by Rayleigh scattering due to the Mie scattering signal appearing during the nucleation process in the gas phase. Correspondingly, laser scattering was only used in pure Ar plasma.

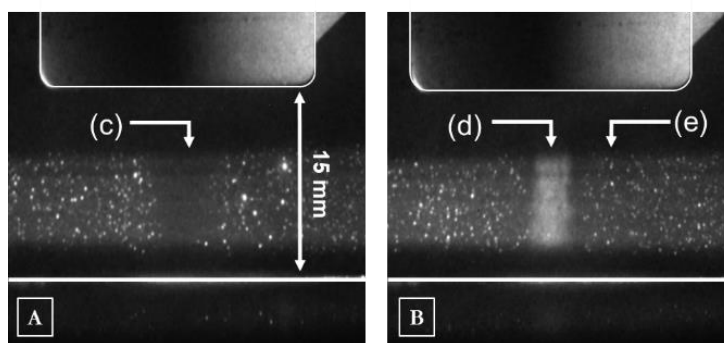


Figure 3.6 - Rayleigh scattering images in pure Ar (A) or Ar/TEOS mixture (B) without synchronization. Scattering was induced by the laser light at 532 nm: (c) Rayleigh scattering region, (d) Mie scattering of nanoparticles nucleated during the gas-phase process, (e) Mie scattering on dust in ambient air

By taking into account the respective experimental errors, results show that T_{gas} measured by Rayleigh scattering at the time positions corresponding to the positive and negative voltage peak (see **Table 3.3**) is close to the values estimated by OH(A-X) band.

In conclusion, the rotational distribution of OH(A) in Ar/TEOS plasmas could be used for T_{gas} measurement taking into account the limitation relevant to filamentary Ar plasmas, while a strong overestimation of T_{gas} has been revealed in the case of N_2 and CH emission. As a result, in the latter cases the rotational temperature is only representative of the different production processes and cannot be used to obtain a good estimation of T_{gas} .

Table 3.3 - Comparison of gas temperature results obtained by OES (T_{rot}) and Rayleigh scattering at different time delays (see Fig 2.4).

Time delay [μs]	T_{rot} (OH band) [K]	Rayleigh scattering [K]
5	410 ± 50	390 ± 15
25	320 ± 50	310 ± 15
45	390 ± 50	340 ± 15

3.2.2 Electron density measurements

TEOS fragmentation and reactive species production are known to be controlled by electron impact reactions and argon metastables collisions during the positive and negative current peaks of a pulsed Ar discharge.[28],[29] To correlate the APPJ discharge behavior with electron kinetics and shed the light on the complexity of the gas-phase mechanisms in Ar/TEOS plasmas, time-resolved measurements of electron density have also been performed using Stark broadening approach. Indeed, Stark broadening of H_{α} and H_{β} lines remains one of the most suitable method for electron density determination in case of relatively dense plasmas ($n_e > 10^{20} \text{ m}^{-3}$).[10]

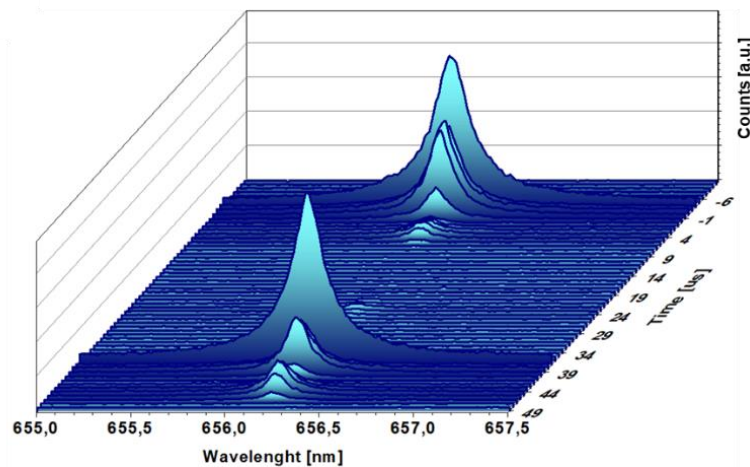


Figure 3.7- Time-resolved H_{α} emission peak at 655.28 nm with a time-step of 1 μs and 0.048 nm of spectral resolution

Even though the most reliable way to estimate electron density implies H_{β} emission line (486.14 nm), the suitability of H_{α} line (656.28 nm) has also been demonstrated by several authors.[8],[10] **Figure 3.7** shows an example of time resolved H_{α} line evolution used for electron density calculations in case of Ar/TEOS plasma, starting from $t = -8 \mu\text{s}$ (i.e. before the beginning of the positive voltage pulse) to $t = 49 \mu\text{s}$ (end of the negative voltage pulse). As illustrated in Figure 3, at $t = -6 \mu\text{s}$ the discharge current rise begins and consequently (see Figure 3.7) the H_{α} intensity reaches the maximum. Afterwards, its intensity decreases by approximately 50% during the subsequent 3 μs most likely due to electron-ion recombination [30],[31],

and further decreases by about 90% until the end of the positive voltage pulse. The H_α emission after the falling edge of the positive voltage pulse appears too weak for reliable Stark broadening calculation and was excluded from analysis. On the other hand, the H_α intensity at $t=37\ \mu\text{s}$ (negative peak) is stronger compared to the positive peak case decreasing more than 50% during the subsequent $3\ \mu\text{s}$. H_α intensity increases again after the voltage falling edge (see **Figure 3.8 (c)**) pointing out on a rather strong secondary discharge taking place during the negative half period. As a consequence, the negative half period ($n_{e,\text{max}} \sim 10^{23}\ \text{m}^{-3}$) is characterized by higher n_e values compared to the positive one ($n_{e,\text{max}} \sim 10^{22}\ \text{m}^{-3}$), which is also reflected in the temporal dynamics of n_e . The Stark broadening method introduce an error of about 10% in n_e estimation for relatively high-density results ($n_e > 10^{20}\ \text{m}^{-3}$), while an error of at least 20% is found in case of low electron density values ($n_e < 10^{20}\ \text{m}^{-3}$).[12]

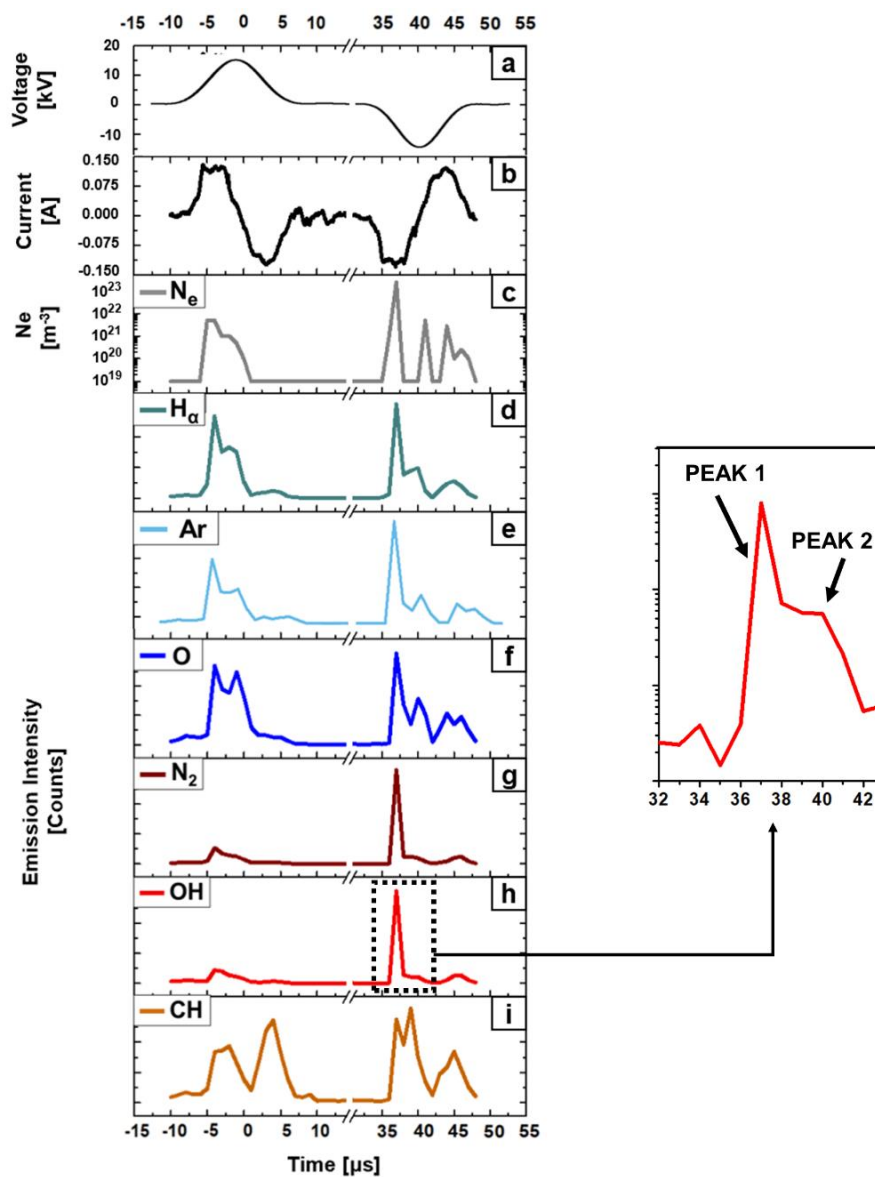


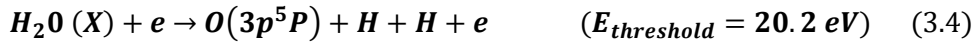
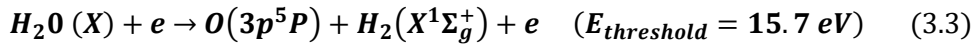
Figure 3.8 - Time-resolved reactive species emission: (a) Applied voltage, (b) Current, (c) Electron density, (d) H_α emission lines at 655.28 nm, (e) Ar emission lines at 696.6 nm, (f) O atom emission lines at 777.41 nm, (g) N_2 emission lines at 337.1 nm, (h) OH emission lines at 308.9 nm, (i) CH emission lines at 431.3 nm

3.2.3 Phase-resolved measurements

From **Figure 3.8** it is clear that the n_e dynamics described above (Figure 3.8(c)) clearly correlates with excited species production in Ar/TEOS plasmas (Figure 3.8(e-i)). The time-resolved emission profiles of the excited species, such as O atoms, N₂ molecules, and OH and CH radicals, could provide additional information to understand which excitation processes are dominant during the plasma evolution.

Few phase-resolved emission intensity patterns can be observed in Figure 9, namely the “multi- peak” behavior of $3p \rightarrow 3s$ O I and CH $A^2\Delta \rightarrow X^2\Pi$ (0,0) transitions at 777.4 nm and 431.3 nm is presented in Figure 3.8 (f,i) while the “double- peak” behavior of N₂ $C^3\Pi_u \rightarrow B^3\Pi_g$ (0,0) and OH $A^2\Sigma^+ \rightarrow X^2\Pi_i$ (0,0) transitions (appearing at 337.1 and 308.9 nm respectively) is shown in Figure 3.8 (g,h). In the first case, the relative intensities at $t = -6 \mu s$ (positive half period) and at $t = 37 \mu s$ (negative half period) are comparable despite the previously described discrepancy detected in terms of n_e . On the other hand, the “double- peak” behavior resembles the n_e profile in terms of relative intensities ratio between the peaks. A short discussion suggesting possible reasons for such behaviors is given below.

It is well known that the presence of O($3p$) excited state (the upper state for the observed O emission in Figure 3.8) in the atmospheric pressure Ar discharges can be ascribed to O₂ molecular dissociation by electron impact ($O_2 + e \rightarrow O + O^* + e$), Penning ionization of O₂ involving Ar metastables ($Ar^m + O_2 \rightarrow Ar + O_2^+ + e$), direct excitation process of ground state O ($O + e \rightarrow O^* + e$) or dissociative excitation of the water molecules (see Equation 3.3 – 3.4).[34] The O₂ electron impact dissociation or Penning processes, subsequent to ambient air diffusion into the plasma discharge, do not contribute to O($3p$) excited state production, therefore, the most probable explanation of the “multi- peak” behavior is the presence of water vapor traces in the Ar flow. In this regard, as suggested by Beenakker *et al.* [35], O($3p$) excited atoms are produced by the dissociative excitation of H₂O:



Hence, the O ($3p$) state production is likely limited by the dissociation rate of H₂O molecules reaching a saturation level at the time delay corresponding to both peaks due to the very low amount of water in the discharge, as confirmed by time-resolved fast imaging of the excited O atoms.

On the other hand, due to diffusion of the surrounding air molecules, the maximum N₂ emission appears at 37 μs time period as a double-peak which is generated because of electron or Ar^m collisions with N₂ ground state molecules:

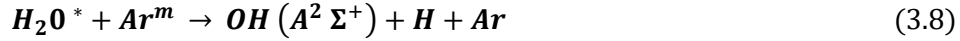


and further electron impact reactions between the pre-excited N₂ ($B^3\Pi_g$) and N₂ ($A^3\Sigma_u^+$) states.[36]

A “double- peak” behavior has also been identified for OH(A-X) emission. In Ar plasmas the excited OH(A) radicals can be produced either by dissociative electron excitation of water molecules



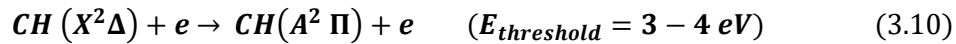
or by Ar^m-H₂O reactions [37]:



If the mechanism (3.7) is dominant, OH(A) radicals would present a “multi peak” behavior reaching a saturation level; while, the second pathway should result in a “double-peak” emission profile, which takes place in our case. This dominant process, confirmed in Figure 3.8(h), does not preclude the presence of the other mechanisms, such as direct electron impact excitation of dissociated OH(X) radicals which contributes widely to the population of excited OH at rotational levels with $J < 12$.



To discuss the CH temporal behavior (Figure 3.8(i)), it is necessary to take into account the main TEOS dissociation products generated during the deposition process. As mentioned above, the TEOS molecules after their collisions with electrons and Ar^m may produce stable fragments, such as CH₃-CH, which can be further dissociated forming ground state CH(X) or excited CH(A) radicals. In our case, the found CH(A) emission possesses a “multi- peak” behavior since the CH(A) state population is probably limited by the dissociation rate of CH₃-CH fragments considering the low amount of precursor injected to the APPJ. Single-step dissociative excitation processes of CH₃-CH fragments or collision with Ar^m are unknown, however, considering that the typical electron energy is close to 1 eV in case of Ar APPJ it is probable that most of the CH(A) emission occurs due to the electron impact:



In addition, unlike the other radicals, the CH(A) emission intensity also form secondary peaks, corresponding the second current pulses, which confirms that the CH(A) time-resolved behavior is caused mainly by low threshold energy reactions or collisions with other excited radicals such as OH.

In addition, as shown in Figure 3.8(i), the phase-resolved emission intensity pattern of CH is also slightly delayed in time with respect to the other excited species. This delay of about 1-2 μ s could be related to the occurrence of simultaneous CH ground state excitation processes induced by electron or Ar^m collisions and consequent multi-step depopulation processes. Indeed, different CH states, such as CH(B) or CH(C), or CH(A) radicals with higher vibrational numbers can populate

the CH ($A, v=0,0$) state before reaching the ground state thus retarding the 431.3 nm transition time-evolution. However, further experimental tests are required in order to prove this suggested mechanism.

3.2.4 Time-resolved discharge imaging

Spatial distribution of the excited species in the active plasma region may further clarify the most important nucleation and thin film growth processes occurring both in the gas phase and at the gas-substrate interface. In order to understand the main formation mechanisms involved in an atmospheric pressure deposition process, a detailed study of the evolution of streamers formed between the jet electrodes is necessary, which is described in this section. The phase-resolved 2D spatial emission of Ar, atomic O, N₂, OH and CH excited species is presented in **Figure 3.9** during the positive/negative pulses and between the current peaks in case of Ar/TEOS mixture. As can be seen from the voltage waveform, all images were obtained after the voltage falling edge, corresponding to the second current peak.

As shown in Figure 2.2, the APPJ configuration used in this work is composed by an HV single electrode Corona-Jet facing a grounded plate covered with a dielectric layer. Accordingly, the discharge is characterized by an intensive plasma region located close to the tip of the HV electrode as confirmed by the Ar I emission at the top of the Figure 3.9. In addition, a strong Ar line emission, induced by the charges deposited on the surface of the dielectric plate during the primary discharge, occurs also next to the ground electrode in analogy with classical DBD configuration. The image acquired between the peaks confirms the presence of Ar excited species only during the active discharge phase characterized by high electron density, as shown in Figure 3.8.

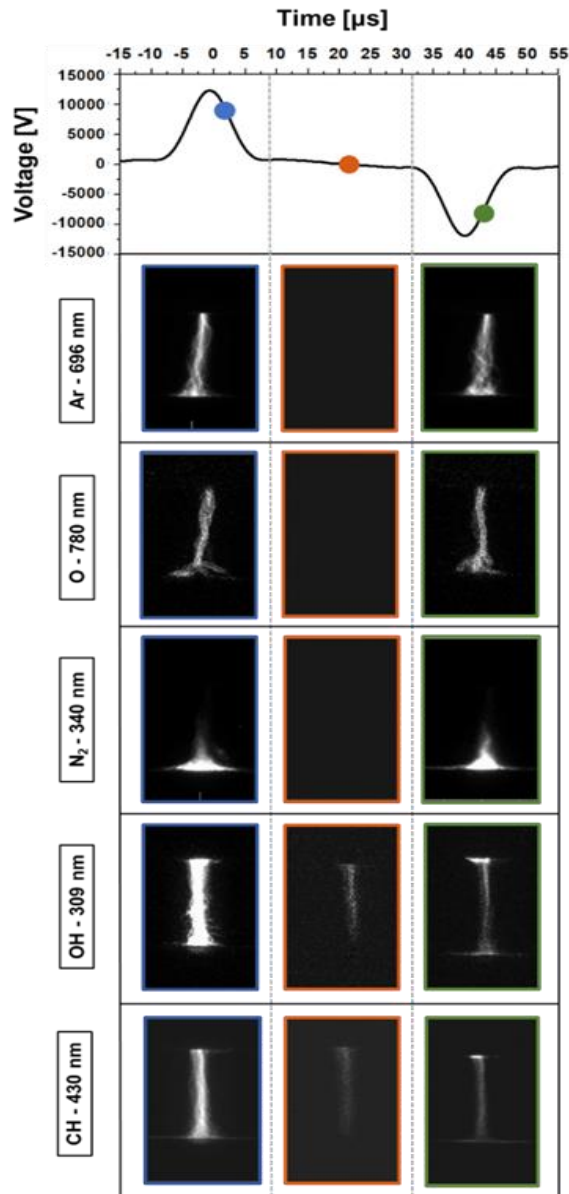


Figure 3.9 - Time-resolved fast imaging of the excited: Ar atoms (20 accumulations), O atoms (single shot), N₂ molecules (20 accumulations), OH and CH radicals (20 accumulations).

As mentioned previously, in case of open-air argon plasma discharges the influence of the ambient air diffusion on the excited species distribution must be taken into account. From the phase-resolved 2D images of the excited N₂ it is possible to deduce that the air back diffusion and admixing is maximum near the ground electrode, probably due to turbulence induced by Ar gas flow pointed toward dielectric surface.[38] As shown in the section 3.2.3, the N₂ emission is strictly related to the diffusion of the surrounding air, while the O atom emission seems to be mostly dependent on the dissociative excitation of the water molecules present in Ar flow. The 2D images of excited O atom and N₂ (Figure 3.9) confirm these different particles sources since the O atom emission appears constant over the entire discharge whereas N₂^{*} emission is localized nearby the bottom plate.

The effect of TEOS admixing on the discharge structure has been also studied by 2D imaging of the OH(A) emission band (as shown in **Figure 3.10**). The data

were acquired in this case during the negative voltage peak with and without precursor. We observed that, TEOS injection reduces OH emission intensity all over the plasma discharge except the region downstream the HV tip. This effect is correlated with the fact that the addition of a complex chemical compounds, like TEOS, results in electron temperature reduction in the discharge due to a change in the energy transfer efficiency between electrons and heavy species.

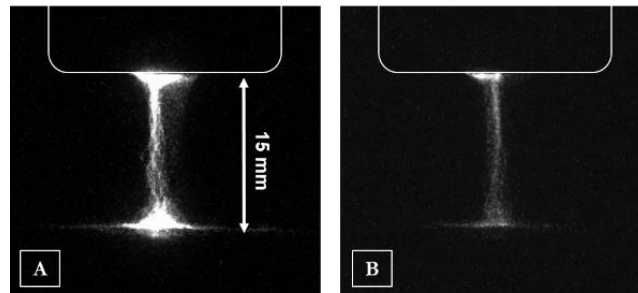


Figure 3.10 - Single shot OH images gained at 42 μ s of delay time (negative peak) in Ar (A) or Ar/TEOS mixture (B).

By comparing the data shown in Figure 3.9 and Figure 3.10 it is clear that OH(A) and CH(A) radicals show almost identical distributions in terms of the streamer shape, emission spatial distribution, and relative intensities. This similarity in the presence of high-emission zones near the HV tip confirms that in both cases both OH(A) and CH(A) radical generation happens via strong influence of Ar metastables. Moreover, the CH(A) and OH(A) emission is detectable between the current peaks confirming key role of Ar metastable production of both radicals.[39]

3.3 Conclusions

The effect of TEOS addition on physical and chemical properties of an APPJ source operating in Ar is studied in detail by optical emission spectroscopy, 2D optical imaging, and Rayleigh scattering techniques. It was confirmed that the rotational temperature of $N_2(C-B)$ transition, equal to 550 K, cannot be used for reliable estimation of the gas temperature also in case of Ar/TEOS plasmas, due to quasi-resonance processes with Ar metastables. On the other hand, the rotational temperature of OH excited radicals, obtained in the assumption of non-Boltzmann rotational distribution, is significantly lower than the one obtained with N_2 molecular bands and its mean value (409 K) is in a good agreement with the Rayleigh scattering results.

For the first time the possibility of using the CH(A-X) transition for gas temperature measurement in an atmospheric pressure Ar/TEOS plasma is investigated. In this case, the Ar metastables as well as the electron impact reactions with TEOS fragments are presumably playing a key role in the CH(A) radical formation in non-thermal equilibrium leading to an overestimation of the gas temperature (590 K) by CH emission bands in the investigated type of discharges.

The phase-resolved measurements as well as the 2D imaging data of the excited species, along with the time-resolved electron density behavior were used to reveal

the predominant production mechanisms of the O($3p$), N $_2$ (C), OH(A), CH(A) excited states in the discharge. It was concluded that the O atom emission is determined mostly by the dissociative excitation of water molecules contained in Ar gas flow, whereas N $_2$ (C) is the product of Ar^m and electron reactions with N $_2$ ground state molecules appearing due to the diffusion of the surrounding air into the active plasma zone. As expected, in the case of atmospheric pressure deposition, Ar metastables also play a dominant role in OH and CH excited radical generation. Finally, from the spatial distribution of CH(A) and Rayleigh scattering images, it has been proven that the most important nucleation processes take place in the gas-phase.

3.4 References

- [1] G. Dilecce, "Optical spectroscopy diagnostics of discharges at atmospheric pressure," *Plasma Sources Sci. Technol.*, vol. 23, no. 1, p. 15011, 2014.
- [2] C. O. Laux, T. G. Spence, C. H. Kruger, and R. N. Zare, "Optical diagnostics of atmospheric pressure air plasmas," *Plasma Sources Sci. Technol.*, vol. 12, no. 2, p. 125, 2003.
- [3] M. Goujon, T. Belmonte, and G. Henrion, "OES and FTIR diagnostics of HMDSO/O $_2$ gas mixtures for SiO $_x$ deposition assisted by RF plasma," *Surf. Coatings Technol.*, vol. 188, pp. 756–761, 2004.
- [4] A. Granier, C. Vallée, A. Goulet, K. Aumaille, and G. Turban, "Experimental investigation of the respective roles of oxygen atoms and electrons in the deposition of SiO $_2$ in O $_2$ /TEOS helicon plasmas," *J. Vac. Sci. Technol. A Vacuum, Surfaces, Film.*, vol. 17, no. 5, pp. 2470–2474, 1999.
- [5] P. Bruggeman, D. C. Schram, M. G. Kong, and C. Leys, "Is the rotational temperature of OH (A--X) for discharges in and in contact with liquids a good diagnostic for determining the gas temperature?," *Plasma Process. Polym.*, vol. 6, no. 11, pp. 751–762, 2009.
- [6] P. J. Bruggeman, N. Sadeghi, D. C. Schram, and V. Linss, "Gas temperature determination from rotational lines in non-equilibrium plasmas: a review," *Plasma Sources Sci. Technol.*, vol. 23, no. 2, p. 23001, 2014.
- [7] A. Sarani, A. Y. Nikiforov, and C. Leys, "Atmospheric pressure plasma jet in Ar and Ar/H $_2$ O mixtures: Optical emission spectroscopy and temperature measurements," *Phys. Plasmas*, vol. 17, no. 6, p. 63504, 2010.
- [8] P. Bruggeman, D. Schram, M. Á. González, R. Rego, M. G. Kong, and C. Leys, "Characterization of a direct dc-excited discharge in water by optical emission spectroscopy," *Plasma Sources Sci. Technol.*, vol. 18, no. 2, p. 25017, 2009.
- [9] R. Morent *et al.*, "Deposition of HMDSO-based coatings on PET substrates using an atmospheric pressure dielectric barrier discharge," *Prog. Org. Coatings*, vol. 64, no. 2–3, pp. 304–310, 2009.
- [10] A. Y. Nikiforov, C. Leys, M. A. Gonzalez, and J. L. Walsh, "Electron density measurement in atmospheric pressure plasma jets: Stark broadening of hydrogenated and non-hydrogenated lines," *Plasma Sources Sci. Technol.*, vol. 24, no. 3, p. 34001, 2015.
- [11] Q. Xiong, A. Nikiforov, N. Britun, R. Snyders, C. Leys, and X. Lu, "A simple profile-fitting method to determine the metastable and resonant densities in a

- cold atmospheric pressure argon plasma jet,” *J. Appl. Phys.*, vol. 110, no. 7, p. 73302, 2011.
- [12] H. R. Griem, “Spectral Line Broadening by Plasmas Academic Press,” *New York*, 1974.
- [13] S. Hofmann, A. F. H. Van Gessel, T. Verreycken, and P. Bruggeman, “Power dissipation, gas temperatures and electron densities of cold atmospheric pressure helium and argon RF plasma jets,” *Plasma Sources Sci. Technol.*, vol. 20, no. 6, p. 65010, 2011.
- [14] M. A. Gigosos, M. Á. González, and V. Cardeñoso, “Computer simulated Balmer-alpha,-beta and-gamma Stark line profiles for non-equilibrium plasmas diagnostics,” *Spectrochim. Acta Part B At. Spectrosc.*, vol. 58, no. 8, pp. 1489–1504, 2003.
- [15] M. Sneeep and W. Ubachs, “Direct measurement of the Rayleigh scattering cross section in various gases,” *J. Quant. Spectrosc. Radiat. Transf.*, vol. 92, no. 3, pp. 293–310, 2005.
- [16] R. B. Miles, W. R. Lempert, and J. N. Forkey, “Laser rayleigh scattering,” *Meas. Sci. Technol.*, vol. 12, no. 5, p. R33, 2001.
- [17] P. Bruggeman and R. Brandenburg, “Atmospheric pressure discharge filaments and microplasmas: physics, chemistry and diagnostics,” *J. Phys. D. Appl. Phys.*, vol. 46, no. 46, p. 464001, 2013.
- [18] A. F. H. Van Gessel, E. A. D. Carbone, P. J. Bruggeman, and J. der Mullen, “Laser scattering on an atmospheric pressure plasma jet: disentangling Rayleigh, Raman and Thomson scattering,” *Plasma Sources Sci. Technol.*, vol. 21, no. 1, p. 15003, 2012.
- [19] P. J. Cullen and V. Milosavljević, “Spectroscopic characterization of a radio-frequency argon plasma jet discharge in ambient air,” *Prog. Theor. Exp. Phys.*, vol. 2015, no. 6, 2015.
- [20] M. Abbasi-firouzjah, S. Hosseini, M. Shariat, and B. Shokri, “The effect of TEOS plasma parameters on the silicon dioxide deposition mechanisms,” *J. Non. Cryst. Solids*, vol. 368, pp. 86–92, 2013.
- [21] J. Petersen, J. Bardon, A. Dinia, D. Ruch, and N. Gherardi, “Organosilicon coatings deposited in atmospheric pressure townsend discharge for gas barrier purpose: Effect of substrate temperature on structure and properties,” *ACS Appl. Mater. Interfaces*, vol. 4, no. 11, pp. 5872–5882, 2012.
- [22] K. Okimura and N. Maeda, “Dissociation processes in plasma enhanced chemical vapor deposition of SiO₂ films using tetraethoxysilane,” *J. Vac. Sci. Technol. A Vacuum, Surfaces, Film.*, vol. 16, no. 6, pp. 3157–3163, 1998.
- [23] S. Kawaguchi, H. Higuchi, H. Li, K. Denpoh, K. Takahashi, and K. Satoh, “Dissociative reactions induced by electron impact and electron transport in TEOS vapor,” *Jpn. J. Appl. Phys.*, vol. 58, no. 6, p. 66003, 2019.
- [24] L. Le Brizoual, A. Granier, and P. Briaud, “Argon metastable density in Ar-0 2 and Ar-TEOS helicon plasmas,” *Proc. XXIII Int. Conf. Phenom. Ioniz. Gases*, vol. 15, pp. 863–872, 1975.
- [25] L. G. Piper, J. E. Velazco, and D. W. Setser, “Quenching cross sections for electronic energy transfer reactions between metastable argon atoms and noble gases and small molecules,” *J. Chem. Phys.*, vol. 59, no. 6, pp. 3323–3340, 1973.
- [26] M. Steinbauer, J. Giegerich, K. H. Fischer, and I. Fischer, “The

- photodissociation dynamics of the ethyl radical, C₂H₅, investigated by velocity map imaging,” *J. Chem. Phys.*, vol. 137, no. 1, p. 14303, 2012.
- [27] J. Luque, M. Kraus, A. Wokaun, K. Haffner, U. Kogelschatz, and B. Eliasson, “Gas temperature measurement in CH₄/CO₂ dielectric-barrier discharges by optical emission spectroscopy,” *J. Appl. Phys.*, vol. 93, no. 8, pp. 4432–4438, 2003.
- [28] G. Dinescu, A. De Graaf, E. Aldea, and M. C. M. Van De Sanden, “Investigation of processes in low-pressure expanding thermal plasmas used for carbon nitride deposition: I. Ar/N₂/C₂H₂ plasma,” *Plasma Sources Sci. Technol.*, vol. 10, no. 3, p. 513, 2001.
- [29] L. Mangolini, “Monitoring non-thermal plasma processes for nanoparticle synthesis,” *J. Phys. D: Appl. Phys.*, vol. 50, no. 37, p. 373003, 2017.
- [30] M. Ducrepin, J. Dike, R. B. Siegel, V. Tarnovsky, and K. Becker, “Optical emissions from electron-impact-excited tetra-ethoxysilane,” *J. Appl. Phys.*, vol. 73, no. 11, pp. 7203–7206, 1993.
- [31] C. P. Klages, A. K. Czerny, J. Philipp, M. M. Becker, and D. Loffhagen, “DBD-based plasma polymerization from monomer-argon mixtures: Analytical model of monomer reactions with excited argon species,” *Plasma Process. Polym.*, vol. 14, no. 12, 2017.
- [32] N. Y. Babaeva and G. V Naidis, “On streamer dynamics in dense media,” *J. Electrostat.*, vol. 53, no. 2, pp. 123–133, 2001.
- [33] S. Hübner, S. Hofmann, E. M. Van Veldhuizen, and P. J. Bruggeman, “Electron densities and energies of a guided argon streamer in argon and air environments,” *Plasma Sources Sci. Technol.*, vol. 22, no. 6, p. 65011, 2013.
- [34] G. Y. Park, Y. J. Hong, H. W. Lee, J. Y. Sim, and J. K. Lee, “A Global Model for the Identification of the Dominant Reactions for Atomic Oxygen in He/O₂ Atmospheric-Pressure Plasmas,” *Plasma Process. Polym.*, vol. 7, no. 3–4, pp. 281–287, 2010.
- [35] C. I. M. Beenakker, F. J. De Heer, H. B. Krop, and G. R. Möhlmann, “Dissociative excitation of water by electron impact,” *Chem. Phys.*, vol. 6, no. 3, pp. 445–454, 1974.
- [36] Q. Xiong *et al.*, “Temporal and spatial resolved optical emission behaviors of a cold atmospheric pressure plasma jet,” *J. Appl. Phys.*, vol. 106, no. 8, p. 83302, 2009.
- [37] T. Shirafuji, Y. Ogura, and Y. Himeno, “Time-resolved optical emission spectroscopy on three-dimensionally integrated micro-solution plasma,” *Jpn. J. Appl. Phys.*, vol. 53, no. 1, p. 10211, 2013.
- [38] E. Traldi *et al.*, “Schlieren imaging: a powerful tool for atmospheric plasma diagnostic,” *EPJ Tech. Instrum.*, vol. 5, no. 1, p. 4, 2018.
- [39] D. Merche, N. Vandencastele, and F. Reniers, “Atmospheric plasmas for thin film deposition: A critical review,” *Thin Solid Films*, vol. 520, no. 13, pp. 4219–4236, 2012.

4

INSIGHTS OF Ar/TEOS GAS-PHASE PROCESSES: GROUND-STATE SPECIES

For a complete understanding of the most significant APPJ initiated gas-phase processes, a detailed analysis of the plasma ground state population is strongly required. Those species cannot be measured directly by OES, previously used for qualitative detection of excited species, and require the employment of advanced active spectroscopy techniques. Among these, Laser Induced Fluorescence (LIF) and two-photon absorption laser induced fluorescence (TALIF) spectroscopy, well-established techniques in which particles are excited to higher energy levels by the absorption of laser light followed by spontaneous emission of a fluorescence signal, stand out for two main advantages:

- the fluorescence signal is species-selective since the narrow-bandwidth of the laser permits the specific selection of a single ground species and its specific level of excitation;
- LIF can be defined as spatially resolved methods since the fluorescence photon emission comes only from the plasma region crossed by the laser beam, rather than the plasma as a whole as in case of emission spectroscopy.[1]

Such features allow to detect the spatial distribution of a considerable number of radicals and atoms typically produced during the plasma treatment under atmospheric conditions, making also possible to correlate the physics of ground state particles with spatially-resolved OES observations discussed in the previous chapter. On the other hand, despite the fluorescence quantum yield reflects the fraction of ground state molecules excited by the laser beam, which spontaneously decay back to a lower quantum level, the particular complexity of laser-excited levels depopulation processes makes a correct interpretation of the experimental results one of the most difficult task behind the method. Moreover, concerning atmospheric pressure plasmas, due to the effect of collisional de-excitation processes which considerably reduce the fluorescence signal detected, a "reasonable" fluorescence quantum yield demands the presence of a large absorbing ground state population in order to achieve measurable LIF signal levels.[2]

Despite these drawbacks, several authors have reported the use of active spectroscopy techniques for ground species absolute density measurements in atmospheric pressure non-thermal plasmas. In this respect, except few works at the end of the '90s regarding the LIF-assisted detection of OH radicals in high-pressure discharges[1], most of the scientific production on this topic dates to the early 2000s. In those years in fact, non-thermal plasmas

were extensively studied for pollutant gasses removal and the spatial-temporal distribution of some dominant reactive species have been detected by laser techniques to understand the dominant reaction mechanisms involved in the process. Among many others examples, R. Ono and T. Oda [3] have reported the temporal behaviour of OH radicals in the post-discharge region of a pulsed arc plasma source by providing fundamental informations about OH production and reaction processes under various water vapor and oxygen concentrations. In the same context, R. Ono [4] measured for the first time the decay rate of atomic oxygen atoms in an O₂/N₂ pulsed DBD plasma source by using TALIF spectroscopy.

In 2011, on the basis of previous results, A. Nikiforov [5] used LIF for the first time to determine the absolute densities of OH radicals in case of atmospheric pressure glow discharges in contact with liquids. The calculated ground-state OH absolute density, between $1.3 \times 10^{21} \text{ cm}^{-3}$ and $1.7 \times 10^{22} \text{ cm}^{-3}$ depending on the discharge current applied and the water electrode polarity, was found to be similar to absorption technique results thus confirming the huge potential of LIF technique for quantitative measurements. From then on, a disparate number of APPJ configuration, typically employed for biomedical applications and the treatment of thermo-sensitive surfaces in general, have been studied in detail by using LIF spectroscopy. For example, in 2012 the OH absolute density produced by an air/He APPJ was measured by S. Yonemori providing useful information about OH radicals production from water vapour traces contained in the He gas flow.[6] Afterward, the effect of water addition on the generation of OH radicals as well as the influence of fluorescence generation processes after the OH laser excitation on quantitative LIF results have been discussed in detail by L. Li *et al.*[7] The same set-up were then employed by A. Nikiforov *et al.* to determine the influence of air diffusion on the atomic O spatial distribution by using TALIF spectroscopy.[8] In this work the authors highlighted the presence of fast recombination processes between O atoms and N₂ or O₂ ambient air molecules by comparing the measurements performed in ambient air with measurements obtained in a pure Ar atmosphere as shown in **Figure 4.1**.

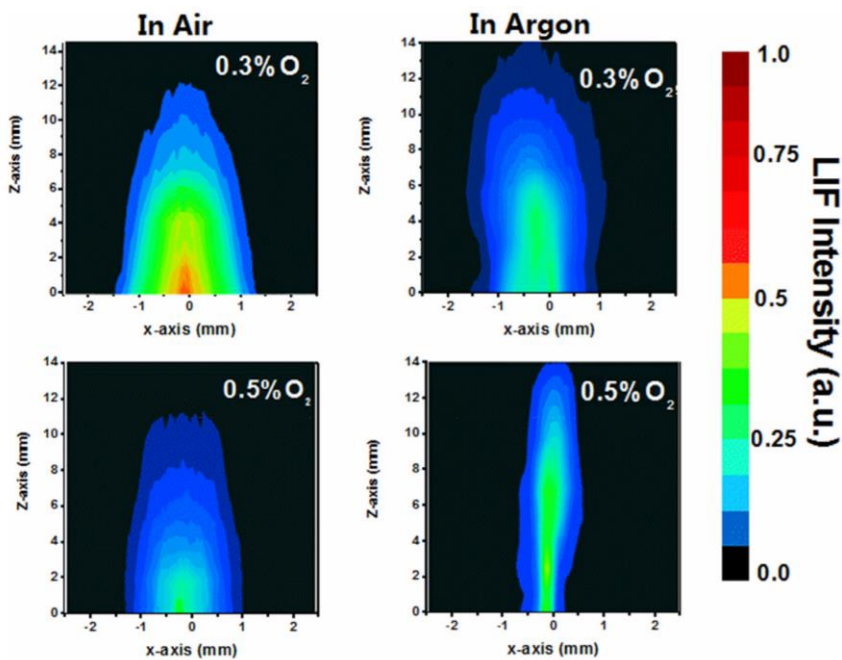


Figure 4.1 – O atoms spatial distribution in case of APPJ working in ambient air or in pure Ar at different admixtures of O₂ in the feed gas [8]

Moreover, during the late 1990s, LIF technique was being widely used also for quantitative measurements of carbon-based radicals, such as hydrocarbon fragments, produced by dc arc-jet plasmas typically employed for the chemical vapor deposition of diamond thin films starting from CH₄. Among several common intermediates yielded during the process, CH radicals have always played a fundamental role in the study of the conversion rate of CH₄ into C₂H₂. In that regard, J. Luque *et al.* used LIF for CH radical absolute density measurements, revealing an exponential decrease of ground state CH at increasing distances from the nozzle.[9],[10] Thereafter, C. Gibaud *et al.*[11] showed spatially resolved profiles of CH radicals in atmospheric pressure air/CH₄ flames while, more recently, planar laser-induced fluorescence (PLIF) were used by J.Kiefer [12] for the study of the arc-jet turbulent behaviour through the simultaneous detection of CH and OH radicals.

In general, even if many efforts have been made to characterize ground state hydrocarbon fragments produced by arc-jets device, there is no evidence of experimental studies reporting in situ detection of ground state CH radicals in case of non-thermal plasmas. Moreover, from the brief overview of the most significative results obtained by active spectroscopy techniques in terms of OH radicals and O atoms, it is clear that the major part of the aforementioned researches are focused on the study of plasma sources commonly used for thermo-sensitive/biological surface treatments or pollutant gasses removal applications, even if the determination of such active species concentrations and their spatial distribution could be of great interest also for other plasma-assisted processes.

Indeed, as extensively discussed in the previous chapters, it is well known that the presence of oxidant species has a significant impact on the removal of the organic content from both gas-phase and adsorbed thin film fragments.[13] In particular, hydroxyl radicals and oxygen atoms are some of the most interesting species due to their key role in the achievement of high-quality SiO₂ thin films. In the past several authors have performed a detailed investigation of the atomic oxygen role in several deposition processes starting from organosilicon precursors by methods of mass-spectroscopy, emission spectroscopy and others, but very few works have reported the use of active spectroscopy techniques for oxygen atoms detection. Among these, R.P. Cardoso pointed out the possibility to employ TALIF measurements for determining the variation of O atoms as a function of the gas mixture composition and the distance from the plasma generation region in a microwave plasma working in Ar/O₂/HMDSO mixtures.[14] Even though the results obtained (shown in **Figure 4.2**) have defined the best conditions for the O atoms production, it is evident that in this case the TALIF signal have been used only for a relative estimation of the O atoms behaviour without providing an in-depth understanding of the reaction mechanisms involved.

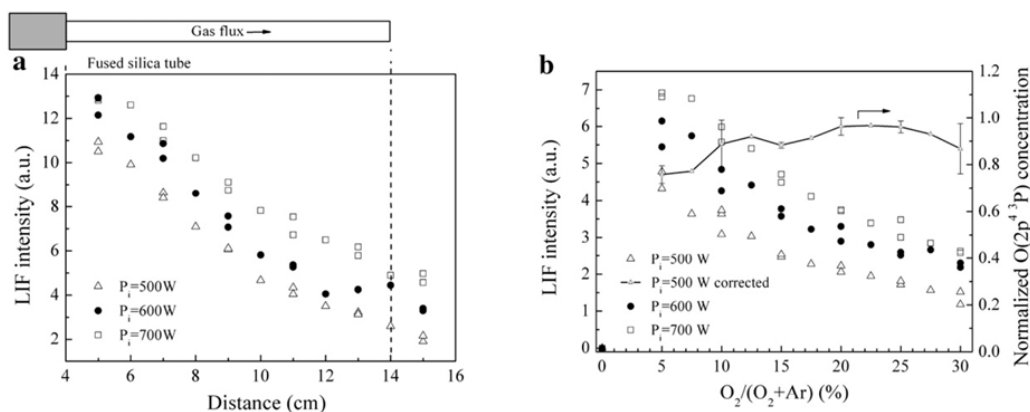


Figure 4.2 – TALIF signal behaviour in Ar/O₂/HMDSO mixtures as a function of the distance from the plasma generation region (left) and the gas mixture composition (right) [14]

Concerning OH radical absolute density measurements for deposition purposes, systematic analysis of the mechanisms are even more limited. Indeed, despite the presence of OH bonds on the thin film surface that could influence the silica-like layer structure and possible impact of OH radicals on the gas-phase precursor dissociation reactions [15], there is only one scientific work reporting the use of active spectroscopy techniques for hydroxyl radicals detection during deposition process. In this work, Bogart et al. [16] combine the spatially-resolved LIF technique with a molecular beam to record two-dimensional images of OH radicals during the surface treatment. This method, also called Radicals Interacting with Surfaces (IRIS) method, was used to study the surface reactivity of OH radicals during the plasma-assisted deposition of SiO₂ thin films starting from TEOS/O₂ mixtures. The results obtained have shown that OH radicals are directly involved in the removal of hydrocarbon contaminants from the thin film surface, but did not provide information about gas-phase mechanisms potentially involved in SiO₂ units formation.

To sum up, there are no evidences of studies reporting the use of LIF/TALIF for OH radicals, CH radicals and O atoms detection in case of atmospheric pressure Ar/TEOS polymerization process, although additional gas-phase characterizations by means of such active techniques are clearly needed to further clarify the mechanism behind the thin film formation as well as establish a clear correlation between the chosen plasma parameters and the surface features of the plasma-deposited films.

Over this chapter, the influence of TEOS admixture on ground-state OH, CH and O spatial distribution is discussed in detail by LIF and TALIF imaging. For the first time the dominant OH, CH and O production and recombination mechanisms are identified in Ar/TEOS mixture. The effects of carrier gas flow injected and the voltage applied on the ground state species distribution are also investigated in order to identify possible differences in terms gas-phase composition.

4.1 MATERIALS and METHODS

A detailed description of the laser spectroscopy system employed in this work for LIF detection of CH and OH radicals and TALIF measurements of O atoms is here provided. The working principle behind the methods and the selected laser-excited levels are also

presented and discussed. As in the previous chapter, the plasma deposition system used for the gas-phase study is the same presented in Fig. 2.1 (chapter 2).

4.1.1 OH-LIF measurements

As outlined in the introduction paragraph, laser-induced fluorescence spectroscopy (LIF) is a widespread active laser technique able to provide quantitative information about the ground state population and suitable for the spatially resolved measurements of these highly populated states involved in many gas-phase reactions. The present technique requires the use of a narrow bandwidth tuneable radiation which excites ground state species into higher states by absorption of a single laser photon. The intensity of the fluorescence signal, caused by the excited particles transition to an energetically lower state, is then measured to provide an estimate of the ground state population. The LIF detection arrangement used in the current work for OH radical measurements is presented in **Figure 4.3**.

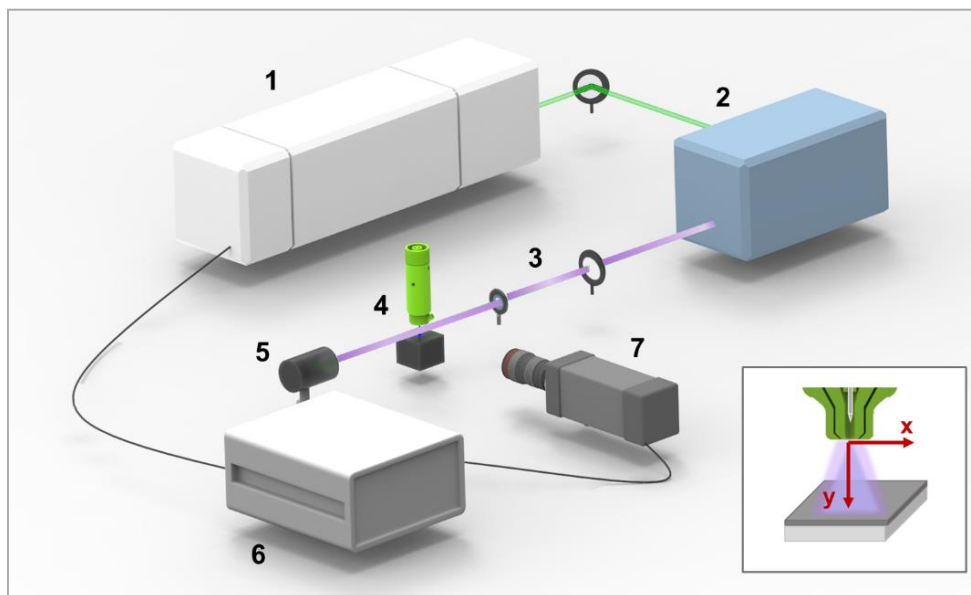


Figure 4.3 – LIF set-up including: Nd:YAG pump laser (1), Dye laser (2), sheet forming optics (3), plasma source (4), beam dump (5), synchronization unit (6) ICCD camera (7)

In detail, the laser spectroscopy system is composed by a Sirah Cobra-Stretch dye laser equipped with a second harmonic generation (SHG) unit and pumped by a Nd:YAG laser working at 532 nm. The Pyrromethene 580 dye was used to produce an UV radiation at 283.463 nm able to excite ground-state OH radicals from the OH ($X^2\Pi, v'' = 0$) state to the OH ($A^2\Sigma^+, v' = 1$) excited state by the $P_1(4)$ excitation transitions. For all OH LIF experiments the laser energy per pulse, monitored by an Ophir PE-9 energy meter, was kept fixed at approximately 2.5 mJ inside the discharge in order to operate in a “linear mode”, thus obtaining a LIF signal linearly proportional to the applied laser energy as shown in **Figure 4.4**.

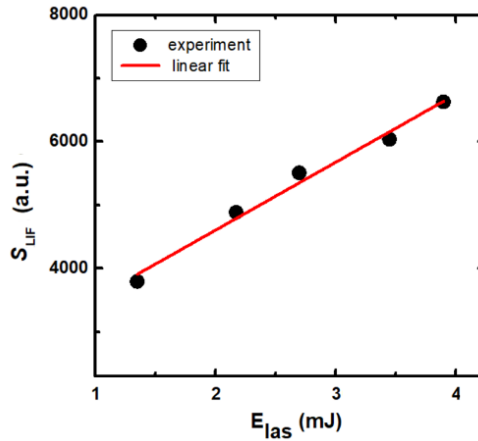


Figure 4.4 – LIF signal intensity as function of the laser energy in Ar/TEOS mixture at 2 μ s of delay time.

The laser beam was focused using a focal lens ($f = 50$ cm) combined with a $f = 10$ cm cylindrical lens and spatially cleaned by an optical diaphragm, in order to avoid the beam reflection from the dielectric plate and the APPJ head, placed 15 cm away from the plasma discharge. The fluorescence signal was then detected, perpendicularly to the laser beam, by an Andor iStar 740 ICCD camera placed at 17.5 cm from the plasma source. 241 x 241 pixels of resolution was used to record the images with a magnification ratio of 16 pixel/mm. An optical band-pass interference filter centred at 309 nm (FWHM = 10 nm) was applied for the OH radical fluorescence signal detection. The laser frequency and pulse duration used for OH radical detection was set at 10 Hz and 5 ns (FWHM) respectively.

The ICCD camera was synchronized with the Nd:YAG laser. Moreover, as described in section 3.1.1, the ICCD camera was synchronized with the AC generator by means of a Stanford Research DG645 digital delay generator and a TTL signal generator (represented as synchronization unit in Fig. 4.3) in order to gain the LIF signal during the positive (2 μ s) and negative (42 μ s) voltage half cycles as well as between the peaks (22 μ s) (voltage and current waveforms of the APPJ used in this work are shown in Fig. 2.4).

The schematic diagram summarising the energy levels involved in OH LIF measurements is presented in **Figure 4.5**. The fluorescence signal wavelength differs from the excitation wavelength because of vibrational energy transfer (VET) processes, induced by collisions with the surrounding species and already discussed in detail by Q. Xiong *et al.* [17] in case of Ar/H₂O plasma.

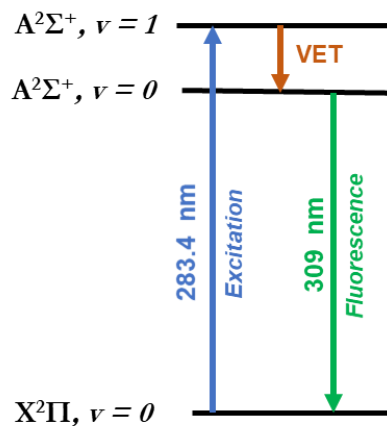


Figure 4.5 – The schematic diagram of energy levels involved in OH LIF measurements

4.1.2 CH-LIF measurements

The LIF set-up presented in section 4.1.1 was used also for ground state CH radical detection. By means of the Nd:YAG laser working at 355 nm and the dye laser containing the Coumarin 120 dye, a laser wavelength near 433.943 nm was selected for CH(X) radical excitation. The wavelength scans, presented in **Figure 4.6(A)**, were performed in order to identify the maximum LIF intensity corresponding to the P₁(5) line of the CH(A-X) system. The CH fluorescence signal was isolated by applying an optical band-pass interference filter centred at 430 nm (FWHM = 10 nm) on the ICCD camera. The laser energy per pulse, selected for all CH LIF experiments, was kept fixed around 1.6 mJ inside the discharge in order to operate in a “linear mode” thus obtaining a LIF signal always linearly proportional to the applied laser energy as shown in Figure 4.6 (right).

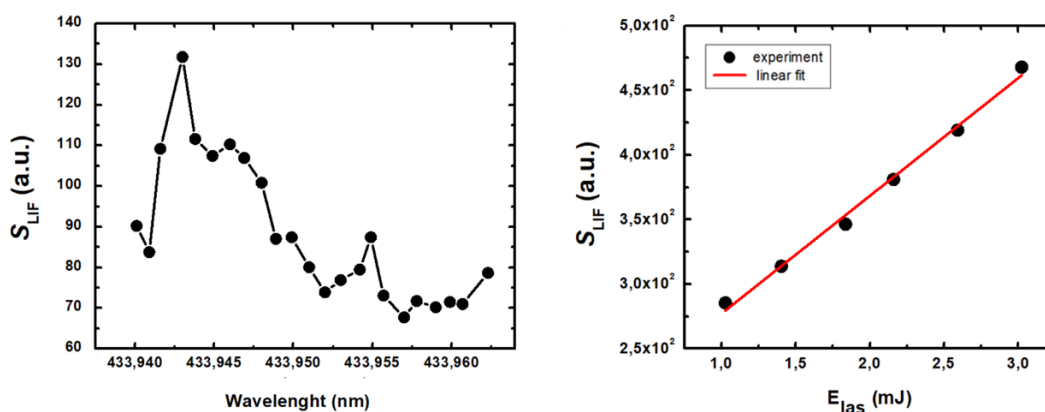


Figure 4.6 –LIF signal wavelength scan (left), LIF signal intensity as function of the laser energy gained at 2 μ s of delay time in Ar/TEOS mixture (right)

The schematic diagram representing the energy levels involved in CH LIF measurements is presented in **Figure 4.7**.

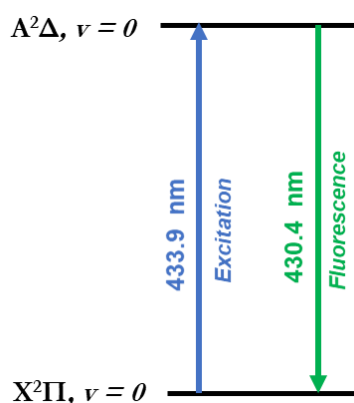


Figure 4.7 –The schematic diagram of energy levels involved in CH LIF measurements

4.1.3 O-TALIF measurements

Two-photon absorption laser-induced fluorescence spectroscopy (TALIF) is a laser technique typically used for quantitative measurements of ground state oxygen atoms.

TALIF is based on a two-photon absorption process in which the atom ground state reaches an excited state by the simultaneous absorption of two ultraviolet (UV) photon. Then, the excited state spontaneously decays to a lower state (not directly back to the ground state) by emitting light in the infrared (IR) region. Also in this case the fluorescence signal emitted from that excited state is proportional to the ground state atoms density. For these experiments the laser wavelength was fixed at 225.654 nm, equivalent to the two-photon excitation energy gap required for the O atom transition from the triplet state atomic oxygen $2p^4 (^3P)_{J=0,1,2}$ to the excited level $3p (^3P)_{J=0,1,2}$.

All oxygen atom measurements have been performed using the same experimental set-up presented in section 4.1.1. However, in this case, the dye laser was pumped by the Nd:YAG laser at 355 nm by using the Coumarin 450 dye in order to obtain the laser emission at around 225.6 nm by means of the SHG unit. The laser energy inside the plasma discharge was kept within the range of 0.3-0.5 mJ. The output laser beam was focused by a $f=50$ cm fused silica lens to produce a spot of about 1.2×1.6 mm inside the plasma region, while the fluorescence signal from the atomic oxygen transition $3p \ ^3P_2 \rightarrow 3s \ ^3S$ ($\lambda= 844.6$ nm) was collected by the ICCD camera equipped with an interference filter centred at 854 ± 12 nm. As shown in **Figure 4.8**, the TALIF signal was preliminary measured along the x-axis ($y= 7$ mm), as defined in **Figure 4.3**, in order to identify the maximum O-atoms fluorescence intensity.

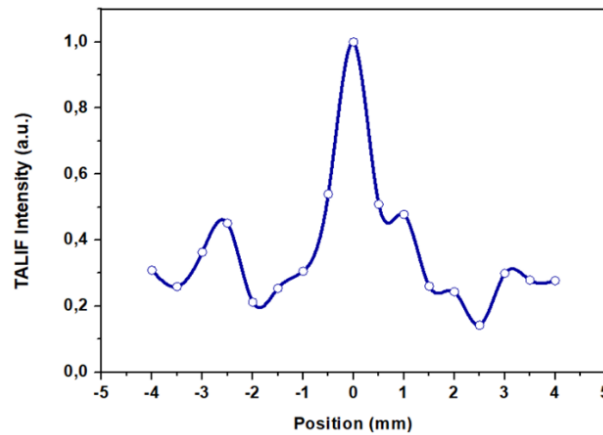


Figure 4.8 –TALIF signal intensity along the x-axis in Ar plasma with 12 kV of voltage applied (22 μ s of delay time and 20 accumulations)

The highest signal has been detected in correspondence of the HV tip ($x= 0$ mm) and, therefore, TALIF measurements have been performed along the y-axis of the plasma discharge (11 different points) by moving the plasma source with respect to the fixed position of the laser beam.

The schematic diagram reporting the energy levels involved in O atoms TALIF measurements is presented in **Figure 4.9**

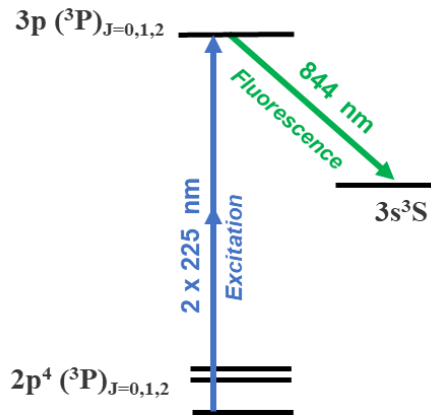


Figure 4.9 –The schematic diagram of energy levels involved in O TALIF measurements

4.2 RESULTS & DISCUSSION

In **Figure 4.10** an example of O atom TALIF signal measured at two different position of the plasma discharge, namely $y= 1.5$ mm (first acquisition point) and $y=11.5$ mm (last acquisition point), which are the closest points to the APPJ head and to the dielectric plate not affected by beam reflection, is presented. The TALIF signal reported in Fig. 4.7 have been acquired at $22 \mu\text{sec}$ of delay time in order to avoid excited atoms emission signals as previously demonstrated in Fig. 3.9 by time-resolved fast imaging results. The pictures, besides showing preliminary informations about the O signal intensity decrease over the y -axis, highlight a non-linear dependence of atomic O concentration on the distance from the x -axis. Indeed, despite the LIF intensity seems to decrease by increasing the distance from the y -axis, namely by passing from region (1) to region (2) in Fig. 4.10, a stronger LIF signal with respect to the region (2) appears also far from the discharge zone (region (3)) probably due to air molecules photodissociation reactions induced by the laser beam crossover. The photodissociation process was confirmed by testing different secondary Ar gas flows: an increase of LIF signal in correspondence of the region (2) was detected by reducing the secondary Ar flow due to the improvement of ambient air back diffusion. The results obtained allow to neglect photodissociation reactions inside the active plasma region thanks to the Ar shield gas barrier effect towards considerable ambient air mixing.

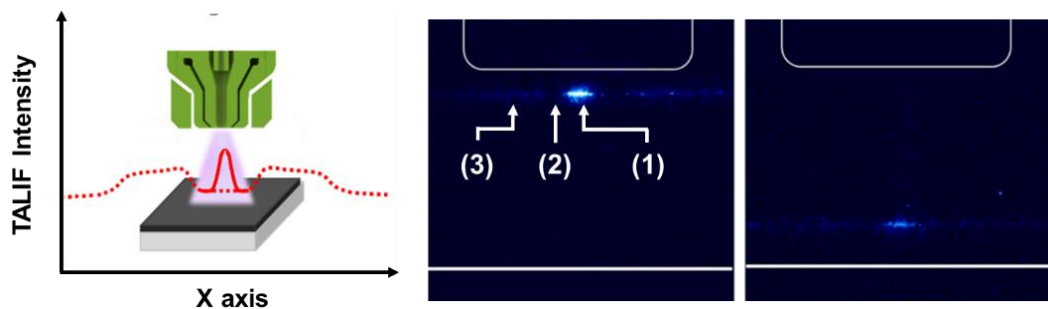


Figure 4.10- TALIF signal behaviour along the x -axis (left), TALIF signal gained at $y= 1.5$ mm and $y=11.5$ mm (right) in Ar plasma with 12 kV of voltage applied ($22 \mu\text{s}$ of delay time and 20 accumulations).

On the other hand, the optical set-up employed for OH and CH radical detection allows to capture the total LIF emission between electrodes without moving the plasma source with respect to the fixed position of the laser beam. The typical appearance of the OH and CH LIF signal in Ar/TEOS mixture is shown in **Figure 4.8(B)** and **4.8(D)** respectively.

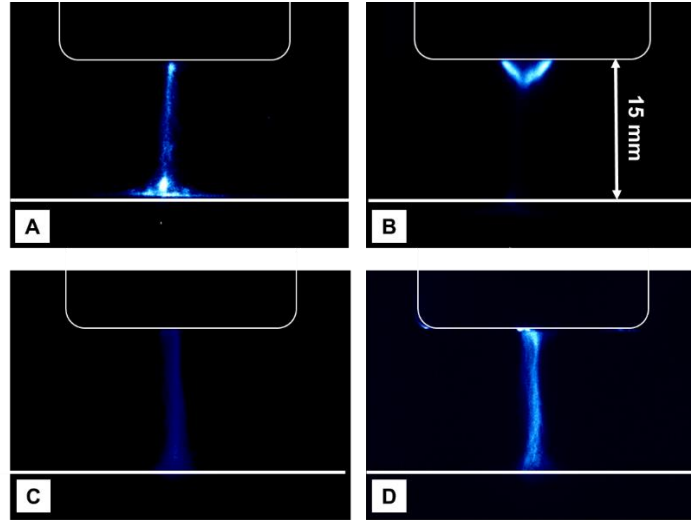


Figure 4.11- Emission and LIF signal detected in Ar/TEOS mixture at 2 μ s of delay time (10 accumulations): A) OH emission signal at 308.9 nm, B) OH LIF signal at 309 ± 5 nm, C) CH emission signal at 431.3 nm and D) CH LIF signal at 430 ± 5 nm

All the LIF images have been corrected by subtracting, as background, the emission signal of the plasma at the corresponding wavelength, measured under identical operating conditions (**Figure 4.11(A)** and **4.11(C)**).

By analogy with the O atom case, the OH and CH LIF signal intensity seems highest near the HV tip, thus revealing the presence of significant gas-phase loss mechanisms involving the detected species and quenchers. Indeed, despite the fluorescence intensity is proportional to the ground state radicals concentration, the influence of different quenching processes has to be taken into account for an accurate discussion of the LIF signal spatial distribution.[17] In light of this, the most significant recombination mechanisms of O atom, OH and CH radical in case of Ar/TEOS plasmas working in ambient air are also presented and discussed in the next sections.

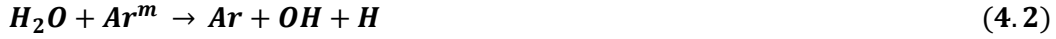
4.2.1 O atoms: precursor and voltage effect

Even if, typically, in case of atmospheric pressure Ar discharges the presence of ground state O atoms can be ascribed to ambient air back diffusion, as suggested by W. Van Gaens *et al.* on the basis of their kinetic model for APPJs working in Ar/humid air mixtures [18], in our case the most probable explanation for O atom production is the presence of water vapor traces in the primary/secondary Ar gas flows. Indeed, as disclosed in Chapter 3 by time resolved imaging and OES measurements, in the present work most of O($3p$) excited atoms are produced by dissociative excitation of water molecules contained in the Ar flow and, correspondingly, H₂O can be considered the dominant initiator also in case of ground state O atoms production. In light of this, most of O atom

population is generated due to dissociation of water molecules by electron impact as described in Equation 4.1,



or by collisions between Ar^m atoms and water molecules:



The indicated pathways are confirmed also by the TALIF spatially resolved profile along the x-axis (plotted in **Figure 4.10**), since the maximum TALIF intensity were detected in correspondence of the HV tip ($x=0$) which is the point characterized by the highest H_2O content and the lowest air admixing due to its proximity to the primary Ar flow outlet.

On the other hand, the exponential decrease of the signal intensity along the y-axis (presented in **Figure 4.12**) can be attributed to O atoms loss reactions related to an increase of air mixing into the discharge by approaching the dielectric plate ($y=15$ mm). In our case, the diffusion of surrounding air inside the discharge, detected by means of 2D images of excited N_2 molecules (Figure 3.9), has been identified as maximum nearby the bottom plate probably due to turbulence events induced by the Ar gas impact on the dielectric surface. From the blue line in Fig. 4.12 it is clear that, at a distance of about 2.5 mm from the HV tip, the TALIF recombination processes start to be dominant with respect to O generation processes thus reducing considerably the signal intensity. A similar TALIF signal profile along the discharge axis has already been observed by D. Schröder [19] in case of a He/ O_2 RF plasma jet operating in air as well as by A. Nikiforov [8] in the post-discharge region of an open-air Ar APPJ.

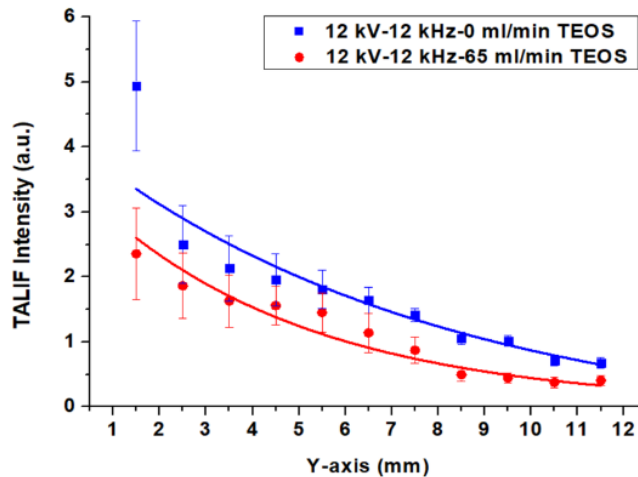


Figure 4.12- Spatial profile of the O TALIF signals along the y-axis with Ar (blue line) and Ar/TEOS mixture (red line) as process gas. The jet was operated in ambient air with 12 kV of voltage applied.

In order to explain the fast signal decay presented in Figure 4.9 (blue line), the most significant recombination reactions of O atoms in pure Ar/air mixture are reported in **Table 4.1** [8]:

Table 4.1- Recombination processes involving atomic O in Ar/air mixture and corresponding rate constants

Reactions	Rate constants	
$O + O_2 + Ar \rightarrow O_3 + Ar$	$5.7 \times 10^{-34} (T_g/298)^{-2.6} \text{ cm}^6 \text{ s}^{-1}$	(4.3)
$O + O_2 + O_2 \rightarrow O_3 + O_2$	$7.3 \times 10^{-25} \text{ cm}^6 \text{ s}^{-1}$	(4.4)
$O + O + Ar \rightarrow O_2 + Ar$	$1.1 \times 10^{-34} \exp(-530/T_g) \text{ cm}^6 \text{ s}^{-1}$	(4.5)
$O + O + O_2 \rightarrow O_2 + O_2$	$2.56 \times 10^{-34} (300/T_g)^{0.63} \text{ cm}^6 \text{ s}^{-1}$	(4.6)
$O + O_3 \rightarrow O_2 + O_2$	$1.5 \times 10^{-11} \exp(-2250/T_g) \text{ cm}^3 \text{ s}^{-1}$	(4.7)
$O + O_2 + N_2 \rightarrow O_3 + N_2$	$2.88 \times 10^{-33} \text{ cm}^6 \text{ s}^{-1} (T_g=300 \text{ K})$	(4.8)
$O + O + N_2 \rightarrow O_2 + N_2$	$2.56 \times 10^{-33} \text{ cm}^6 \text{ s}^{-1} (T_g=300 \text{ K})$	(4.9)

In particular, the three-body reactions with O₂ (Eq. 4.4 and 4.6) or N₂ molecules (Eq. 4.8- 4.9) start to be dominant near the dielectric plate where the Ar gas shielding effect is weaker and the air mixing is substantial.

The influence of TEOS admixture on the spatially resolved profile of O TALIF signals is also presented in Figure 4.12. The exponential decrease detected along the y-axis in case of Ar (blue line) and Ar/TEOS discharge (red line) seems very similar thus proving a low-impact of TEOS molecules in O atoms recombination reactions over the region far from the tip. Differently, the signal intensity near the HV electrode (y=1.2 mm) in case of pure Ar is considerably higher with respect to the case with precursor, confirming the effect of complex chemical compounds, like TEOS, in electron temperature reduction due to a change in the energy transfer efficiency between electrons and heavy species.

On the other hand, the spatial profiles detected under the lowest operating conditions (6 kV-12 kHz) present exactly the same TALIF signal intensity with and without precursor along the discharge axis (data not shown). In this case, it is not possible to identify any substantial effect of TEOS fragments on O density probably due to very low TEOS fragmentation.

In order to confirm this result, the voltage effect on the O TALIF signal profile have been then investigated in case of Ar/TEOS mixture as shown in **Figure 4.13**. The decrease in atomic O concentration follows two different exponential decays along the y-axis probably due to different TEOS fragmentation rates and so different amounts of quenchers formed at low and high voltage operation mode. Notably, by assuming the presence of the same loss mechanism reported in Eq. 4.3-4.9 near the ground electrode, an increase of applied voltage leads to higher precursor fragmentation and in turn the number of O atoms which react with TEOS fragments thus resulting in a faster signal decay in the region downstream the HV tip (up to 6 mm).

On the other hand, in term of deposition purposes, it is important to highlight the fact that the O atoms effluent affecting the target under the two different values of voltage applied is almost the same thereby excluding difference in terms of gas-surface reactions between O atoms and thin films organic compounds.

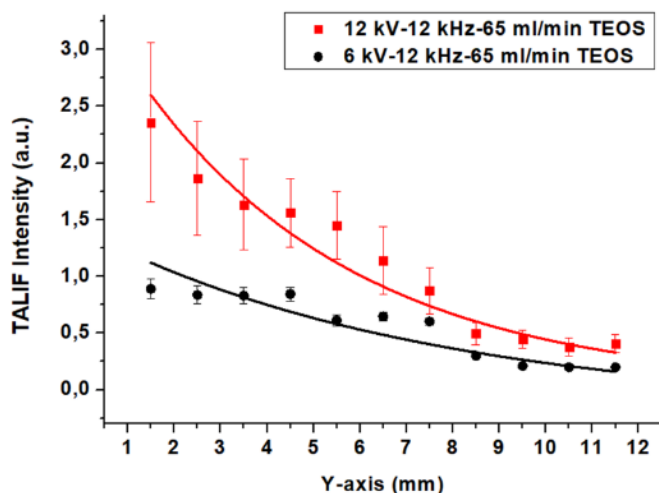


Figure 4.13- Spatial profile of the O TALIF signals along the y-axis in Ar/TEOS mixture with 12 kV (red line) and 6 kV (black line) of voltage applied

Taking into account the TALIF results obtained in Ar/TEOS mixtures and the most significative TEOS fragmentation pathways (described in Chapter 3) reporting hydrocarbon fragments as first products of TEOS dissociation, the dominant recombination reactions of O atoms in the region downstream the HV tip are summarized in **Table 4.2**.

Table 4.2- Recombination processes involving atomic O in Ar/TEOS mixture and corresponding rate constants

Reactions	Rate constants [$\text{cm}^3 \text{s}^{-1}$]	Ref.
$\text{TEOS} + \text{O} \rightarrow \text{Products}$	4.5×10^{-15} ($T_g=300 \text{ K}$)	(4.10) [20]
$\text{O} + \text{C}_2\text{H}_6 \rightarrow \text{OH} + \text{C}_2\text{H}_5$	$1.66 \times 10^{-15} (T_g)^{1.5} \exp(-2920/T_g)$	(4.11) [21]
$\text{O} + \text{C}_2\text{H}_5 \rightarrow \text{CH}_2\text{CHO} + \text{H}$ $\rightarrow \text{HCHO} + \text{CH}_3$	1.1×10^{-10} ($T_g=300 \text{ K}$)	(4.12) [21]
$\text{O} + \text{C}_2\text{H}_4 \rightarrow \text{CH}_2\text{CHO} + \text{H}$ $\rightarrow \text{HCO} + \text{CH}_3$ $\rightarrow \text{HCHO} + \text{CH}_2$ $\rightarrow \text{CH}_2\text{CO} + \text{H}_2$	$2.25 \times 10^{-17} (T_g)^{1.88} \exp(-90/T_g)$	(4.13) [21]
$\text{O} + \text{CH}_3 \rightarrow \text{HCHO} + \text{H}$	1.4×10^{-10} ($T_g=300 \text{ K}$)	(4.14) [21]
$\text{O} + \text{CH} \rightarrow \text{CO} + \text{H}$	6.6×10^{-11} ($T_g=300 \text{ K}$)	(4.15) [21]

The presence of very fast quenching reactions with hydrocarbon fragment such as C_2H_5 (Eq. 4.12), CH_3 (Eq. 4.14) and CH (Eq. 4.15) radicals explains the faster decay of the O signal at in case of Ar/TEOS mixture .

Lastly, the TALIF signal intensity at 1.5 mm of distance from the HV tip was gained as function of the amount of TEOS injected into the plasma discharge. **Figure 4.14**

illustrates that the O atoms content decrease rapidly by passing from 0 to 52 ml/min of carrier gas thus confirming the dominant recombination reactions of O atoms presented above (table 4.2). Otherwise, an almost constant TALIF intensity was detected between 52 ml/min and 90 ml/min of precursor flow probably due to an oversupply of TEOS molecules with respect to the dissociation efficiency of the plasma source at fixed operating conditions (12 kV-12 kHz).

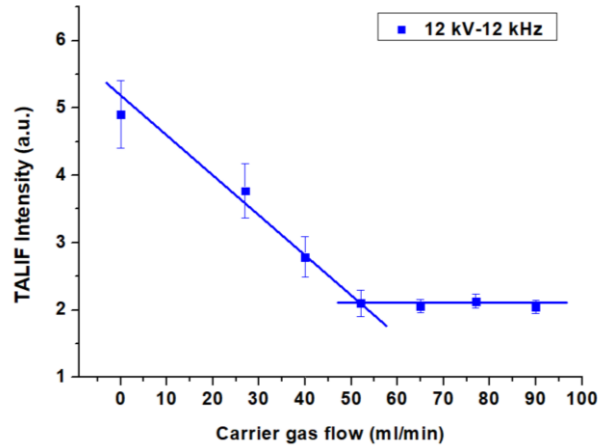


Figure 4.14- Carrier flow effect on O TALIF signal intensity

4.2.2 Two-dimensional LIF imaging of OH radicals in Ar/TEOS plasmas

Typical two-dimensional LIF maps in case of pure Ar plasma and Ar/TEOS plasma are presented in **Figure 4.15(A)** and **4.15(B)** respectively. As previously disclosed by several authors, the presence of ground state OH radicals in atmospheric pressure Ar discharges can be mainly ascribed to water molecules dissociation reactions induced by electron and Ar^m impact and the most significative mechanisms for OH(X) production are reported in **Table 4.3** [17]

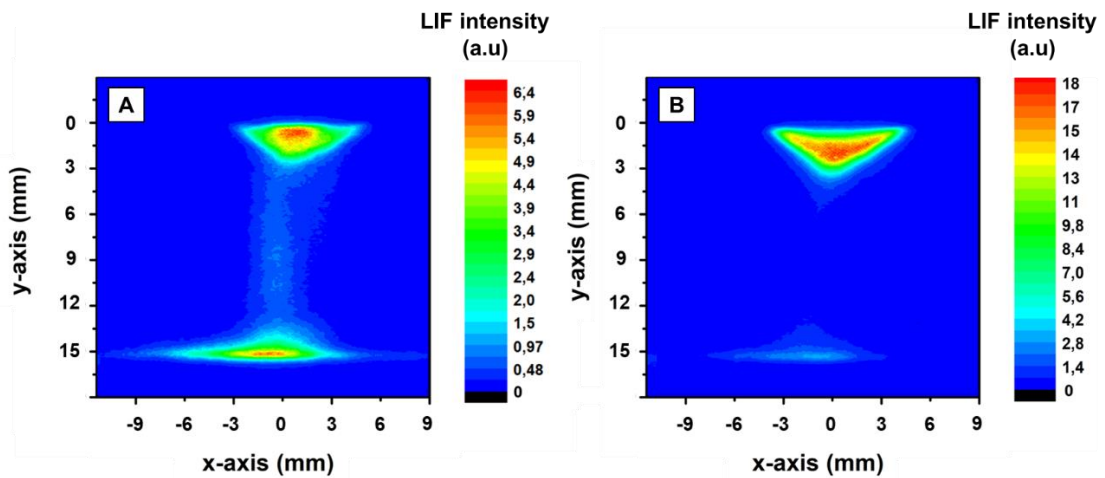


Figure 4.15 – OH spatial distribution in Ar (A) and Ar/TEOS (B) mixtures (two different LIF intensity scales have been used for a full representation of both signal distributions)

Table 4.3- Dominant reactions for OH(X) radicals production in Ar

Reactions	Rate constants [cm ³ s ⁻¹]	
$e^- + H_2O \rightarrow OH + H + e^-$	$10^{-12} - 10^{-10}$ ($T_e = 1-2$ eV)	(4.16)
$Ar^m + H_2O \rightarrow OH + H + Ar$	4.5×10^{-10}	(4.17)
$e^- + H_2O^+ \rightarrow OH + H$	2.6×10^{-8} (T_e) ^{0.5}	(4.18)

These production mechanisms, in accordance with excited OH results shown in Chapter 3, are confirmed in Figure 4.15 where the signal intensity near the HV tip is the highest, probably because of the highest n_e and T_e values in that region. Moreover, the similarity of the LIF images shown in Figure 4.16(A) and 4.16(B) confirms that the spatial distribution and relative intensity of laser-excited OH radicals in correspondence of the positive current peak (2 μ s) and between the peaks (22 μ s) respectively is almost the same thus confirming the key role of long living species, such as Ar metastable in OH(X) radicals production. Indeed, as described by Q. Xiong *et al.*[22], the lifetime of OH radicals in case of Ar/humid air mixture is typically lower than 100 ns due to the quenching of excited OH radicals by H₂O, Ar, O₂ and N₂ and, consequently, the OH radical presence far from the positive current peak is directly related to local Ar^m-H₂O reactions (Eq. 4.17).

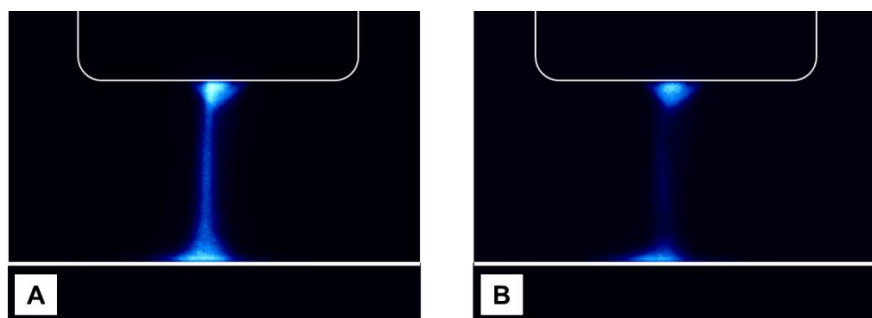


Figure 4.16 – OH LIF imaging of the plasma jet working in Ar. The signal has been acquired in correspondence of the positive voltage peak (A) and between the peaks (B) with 20 accumulations.

In our case, small traces of H₂O are contained both in the Ar gas flow and in the surrounding air diffusing into the plasma discharge. Accordingly, a strong LIF signal was detected also near the dielectric plate (Figure 4.15(A)) due to the maximum air mixing and the DBD behavior of the plasma device, already discussed in previous chapters. In addition, taking into account the high rate constant (cm³s⁻¹) values reported in Table 4.3, the dissociative recombination of water ions (Eq. 4.18) can also play a crucial role in the OH(X) generation in the central zone of the plasma discharge, characterized by lower electron temperature values with respect to the HV and ground electrode regions. [8],[23]

Figure 4.15(B) illustrates the spatial distribution of OH radicals in Ar/TEOS mixtures. In this case, the LIF signal intensity near the bottom plate ($y=15$ mm) is clearly lower in respect to a case of the pure Ar discharge because of the presence of heavy species which considerably reduce the electron temperature value along the plasma discharge axis. Conversely, in Ar/TEOS mixture, the OH(X) intensity is the highest at 2-3 mm of distance

from the HV tip, where the concentration of precursor fragments is maximum, thus revealing the presence of further production mechanism respect those proposed in Table 4.3. Indeed, near the HV tip where the atomic oxygen content is maximum (Fig. 4.12), the following fast and very effective OH production processes between oxidant species and hydrocarbon fragments become dominant:

Table 4.4- Dominant reactions for OH(X) radicals production in Ar/TEOS mixture

Reactions	Rate constants [cm ³ s ⁻¹]	Ref.
$O + CH \rightarrow OH + C$	9.05×10^{-15} (T _g =300 K)	(4.19) [24]
$O + CH_2 \rightarrow OH + CH$	1.33×10^{-10} (T _g =300 K)	(4.20) [25]
$O_2 + CH \rightarrow OH + CO$	8.0×10^{-11} (T _g =300 K)	(4.21) [26]

Additionally, OH radicals can be produced by atomic O recombination reaction with C₂H₆ fragments as proposed in Eq. 4.11. A more detailed investigation of the proposed mechanism is presented in section 4.2.3 as function of the CH LIF signal behaviour under the same operating conditions.

An accurate knowledge of dominant OH quenchers is strongly required for a good understanding of the LIF signal distribution between the plasma jet electrodes. In case of Ar discharge (Fig. 4.15(A)) the lowest OH radical concentration has been observed in the middle region (between y=3 and y=12 mm) where T_e and n_e values drops down and OH(X) loss processes become dominant. On the basis of absolute density results obtained by A. Nikiforov *et al.*, the most significative OH radical recombination mechanisms in Ar plasmas working in ambient air are summarized in **Table 4.5**.

Table 4.5- Recombination processes of OH radicals in Ar and corresponding rate constants

Reactions	Rate constants	
$OH + OH \rightarrow H_2O + O$	$6.2 \times 10^{-14} (298/T_g)^{2.6} \exp(945/T_g) \text{ cm}^3 \text{ s}^{-1}$	(4.22)
$OH + OH + Ar \rightarrow H_2O_2 + O$	$6.94 \times 10^{-31} \text{ cm}^6 \text{ s}^{-1}$	(4.23)
$Ar + OH + H \rightarrow Ar + H_2O$	$10^{-31} \text{ cm}^6 \text{ s}^{-1}$	(4.24)
$OH + O \rightarrow O_2 + H$	$2.4 \times 10^{-11} \exp(-109/T_g) \text{ cm}^3 \text{ s}^{-1}$	(4.25)
$OH + O_2 \rightarrow HO_2 + O$	$3.7 \times 10^{-11} \exp(-26506/T_g) \text{ cm}^3 \text{ s}^{-1}$	(4.26)
$OH + O_3 \rightarrow HO_2 + O_2$	$1.7 \times 10^{-12} (298/T_g)^2 \exp(-945/T_g) \text{ cm}^3 \text{ s}^{-1}$	(4.27)
$OH + HNO \rightarrow H_2O + NO$	$8 \times 10^{-11} \exp(-500/T_g) \text{ cm}^3 \text{ s}^{-1}$	(4.28)
$OH + NO_2 + Ar \rightarrow HNO_3 + Ar$	$2.5 \times 10^{-30} (T_g/298)^{-4.4} \text{ cm}^6 \text{ s}^{-1}$	(4.29)

In our case, at 15 mm of distance from the HV tip, despite reactions 4.25-4.29 are mainly caused by surrounding air diffusion and the maximum air mixing was detected near the bottom plate, the OH production pathways proposed in Table 4.3 are dominant respect recombination mechanism (Table 4.5) due to an intensive plasma located close to the ground electrode (Fig 3.9). On the other hand, the yield of the reactions 4.22-4.29 is maximum in the central region of the discharge, conferring a distinctive “hourglass” shape to the LIF signal.

Further recombination mechanisms between OH(X) radicals and TEOS fragments could occur in case of Ar/TEOS plasmas. The most significative OH radical reactions with hydrocarbon fragments, proposed here for the first time in case of Ar/TEOS APPJ, are reported in **table 4.6**. These reactions should become dominant in the plasma region far from the HV tip thus explaining the faster decrease of OH radicals along the y-axis in case of precursor.

Table 4.5- Recombination processes of OH radicals in Ar/TEOS mixtures and corresponding rate constants

Reactions	Rate constants [cm ³ s ⁻¹]		Ref.
$OH + C_2H_5 \rightarrow C_2H_4 + H_2O$	1.1×10^{-10}	(T _g =300 K)	(4.30) [27]
$OH + CH_3O \rightarrow CH_2O + H_2O$	3×10^{-11}	(T _g =300 K)	(4.31) [27]
$OH + CH_3 \rightarrow CH_2O + H$	1.2×10^{-10}	(T _g =300 K)	(4.32) [28]
$OH + CH_2 \rightarrow CH_2O + H$	5×10^{-11}	(T _g =300 K)	(4.33) [27]

Similar production and recombination mechanisms can be assumed also under the lowest operating conditions (6 kV-12 kHz). In fact, despite the LIF signal intensity is uniformly reduced along the discharge axis respect the relative signal intensity presented in Fig. 4.15, the OH radical spatial distribution and the TEOS influence on the fluorescence signal is exactly the same.

As a conclusion, both air diffusion and TEOS injection play a key role in the production and recombination of OH radicals. On the basis of the mechanisms and the quenching rates of the main colliders reported above, absolute density measurements will be performed in the future to further clarify difference in terms of OH radical concentration under different operating conditions.

4.2.2 Two-dimensional LIF imaging of CH radicals in Ar/TEOS plasmas

As discussed in section 3.2.1 (Chapter 3), the first products of TEOS dissociation are most likely hydrocarbon and Si-O containing fragments. Among these, CH(X) radicals are of particular interest since they can provide preliminary information about the fragmentation efficiency of complex organosilicon compounds.[9] In this regard, the spatial distribution of CH has been explored in detail in this work in order to define the most significant production and recombination gas-phase mechanisms as well as discuss the influence of process parameters on the CH LIF signal intensity.

Two-dimensional LIF maps of ground state CH obtained in Ar/TEOS mixture with different precursor gas flows and voltage conditions are presented in **Figure 4.17**. The LIF signal behaviour as a function of the TEOS amount injected into the APPJ working at 12 kV (Fig. 4.17(A)-(B)) and 6 kV (Fig. 4.17(C)-(D)) is totally different and contrasting. Indeed, at 6 kV of voltage applied the fluorescence signal decrease by increasing the carrier gas flow from 40 ml/min to 90 ml/min thus highlighting an oversupply of TEOS molecules respect the dissociation efficiency of the plasma source. On the other hand, increasing the TEOS content at 12 kV the LIF signal intensity increases proving a higher fragmentation efficiency and consequently greater potentiality in terms of deposition rate.

In general, by comparing Fig. 4.17(D) and Fig. (4.17(B)) it is clear that higher values of voltage applied, which correspond to higher n_e and T_e values, leads to faster CH(X) production rates. The same results can be deduced by the spatial distribution of CH radicals along the y-axis, since the highest signal intensity for all tested cases was detected near the HV tip where T_e values and, consequently, TEOS dissociation are maximum. Moreover, differently from OH radicals, the CH LIF signal detected in correspondence of the dielectric plate is lower respect all the other regions of interest thereby proving that gas-surface reactions, which typically have an active role in the removal of the thin film organic content, don't affect significantly the fluoresce signal. As a consequence, in our case, the most important nucleation processes take place in the gas-phase as already demonstrated by Rayleigh scattering images reported in Fig. 3.6.

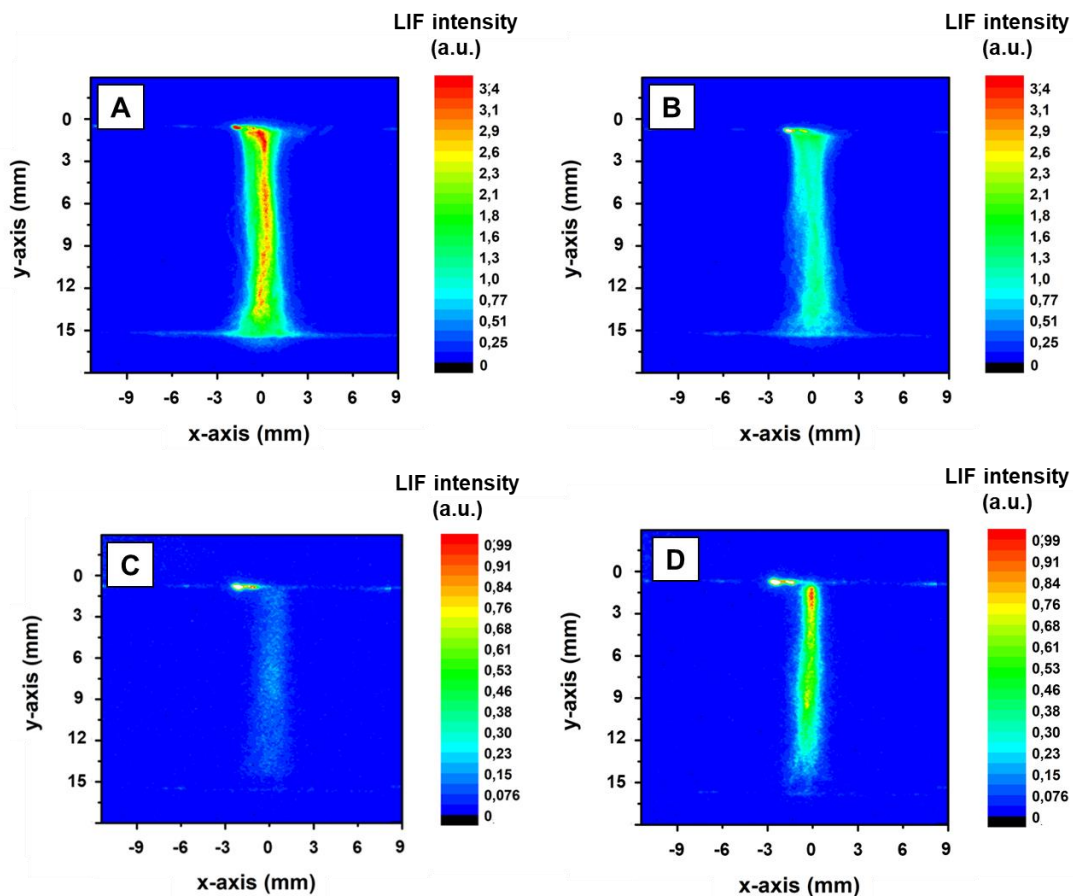


Figure 4.17 – CH spatial distribution in Ar/TEOS mixture: (A) 12 kV – 90 ml/min of carrier flow, (B) 12 kV – 40 ml/min of carrier flow, (C) 6 kV – 90 ml/min of carrier flow, (D) 6 kV – 40 ml/min of carrier flow

The CH LIF signal have been then used to further shed the light on the complexity of gas-phase mechanisms between active species and hydrocarbon fragments. Indeed, as shown in **Figure 4.18** for the 12-kV case, the O atoms, OH and CH radical behaviours at 1.5 mm from the HV tip have been plotted as a function of the precursor content injected into the plasma source. As expected, the increase of TEOS content results in a significant drop of the O TALIF signal while a large signal increase has been detected in case of CH and OH radical. Moreover, for carrier gas flows greater than 52 ml/min (14 ppm of TEOS), the O atoms and OH intensity seem unaffected by a further TEOS increase, whereas the CH signal keeps growing exponentially. Such results prove that the OH production near the HV tip is not only due to electron impact or Ar^m reactions, but is also related to the presence of O atoms (as shown in Table 4.4). These very fast and effective processes (Eq. 4.19-4.21) are significant exclusively in presence of high content of TEOS fragments and O atoms, while common OH production mechanisms such as water molecules dissociation reactions described in Eq. 4.16 - 4.18, are dominant near the dielectric plate in line with pure Ar discharge experimental findings.

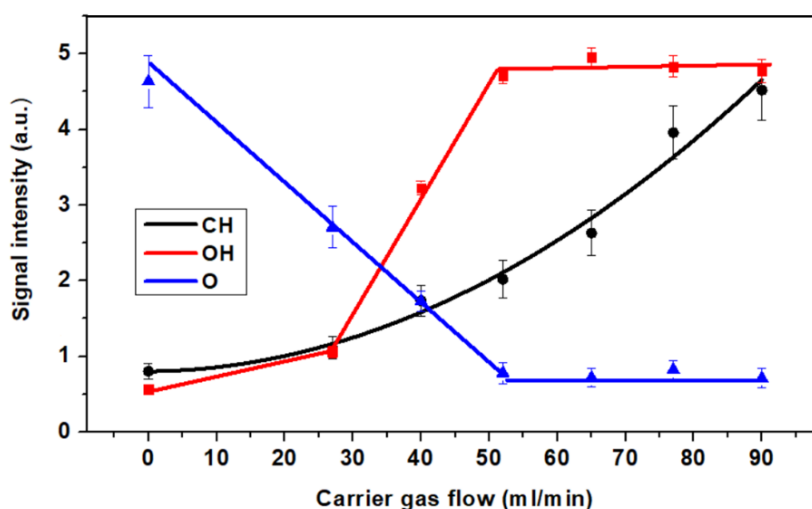


Figure 4.18 –Carrier flow effect on O atoms, OH and CH radicals (12 kV-12 kHz)

4.3 Conclusions

The effect of TEOS admixture on ground state O, OH and CH production and recombination processes during an atmospheric pressure deposition process is investigated in this work for the first time. LIF and TALIF techniques are used to determine the spatial distribution of such active species along the plasma discharge under different gas flow and power conditions and to get first insights in physical and chemical mechanisms of precursor fragmentation.

In line with previous findings, most of O atom production in pure Ar and Ar/TEOS mixtures is provided by dissociation of water molecules contained in Ar gas flow due to electron and Ar metastable impact. On the other hand, the presence of TEOS fragments affect the recombination rate of O atoms along the y-axis, thus increasing the loss of O atoms in respect to the pure Ar case.

Moreover, it is found that the OH radical production in presence of a high content of hydrocarbon fragments is dominated by recombination processes between O atoms and CH radicals. While, dissociative reactions of water molecules by Ar^m and electron impact play a crucial role in the OH(X) production near the ground electrode, as already demonstrated by several author in case of Ar/air mixture. Recombination reactions with TEOS product and air molecules are maximized in the central region of the discharge by conferring a distinctive “hourglass” shape to the OH LIF signal.

Lastly, based on the 2D LIF imaging results, the presence of gas-surface reactions capable of improving the thin film inorganic content is excluded due to the very low CH signal detected in the proximity of the dielectric plate.

The present results pave the way to O, OH and CH radical absolute density measurements in case of atmospheric pressure Ar/TEOS plasma. The evaluation of absolute density of radicals will require a knowledge of quenching rates of TOES fragments with excited states of the radicals generated during the LIF process. The rates of TEOS are mostly unknown at the moment and additional research will be required in future.

4.4 References

- [1] L. Li, “Diagnostics of Reactive Species in Atmospheric Pressure Non-Thermal Plasmas,” 2015.
- [2] T. Freearge and G Hancock, “A Guide to Laser-Induced Fluorescence Diagnostics in Plasmas,” 1997.
- [3] R. Ono and T. Oda, “Measurement of hydroxyl radicals in an atmospheric pressure discharge plasma by using laser-induced fluorescence,” *IEEE Trans. Ind. Appl.*, vol. 36, no. 1, pp. 82–86, 2000.
- [4] R. Ono, Y. Yamashita, K. Takezawa, and T. Oda, “Behaviour of atomic oxygen in a pulsed dielectric barrier discharge measured by laser-induced fluorescence,” *J. Phys. D. Appl. Phys.*, vol. 38, no. 16, pp. 2812–2816, 2005.
- [5] A. Nikiforov, Q. Xiong, N. Britun, R. Snyders, X. P. Lu, and C. Leys, “Absolute concentration of OH radicals in atmospheric pressure glow discharges with a liquid electrode measured by laser-induced fluorescence spectroscopy,” *Appl. Phys. express*, vol. 4, no. 2, p. 26102, 2011.
- [6] S. Yonemori, Y. Nakagawa, R. Ono, and T. Oda, “Measurement of OH density and airhelium mixture ratio in an atmospheric-pressure helium plasma jet,” *J. Phys. D. Appl. Phys.*, vol. 45, no. 22, 2012.
- [7] L. Li *et al.*, “OH radicals distribution in an Ar-H₂O atmospheric plasma jet,” *Phys. Plasmas*, vol. 20, no. 9, 2013.
- [8] A. Nikiforov, L. Li, N. Britun, R. Snyders, P. Vanraes, and C. Leys, “Influence of air diffusion on the OH radicals and atomic O distribution in an atmospheric Ar (bio)plasma jet,” *Plasma Sources Sci. Technol.*, vol. 23, no. 1, 2014.
- [9] J. Luque, W. Juchmann, and J. B. Jeffries, “Absolute concentration measurements of CH radicals in a diamond-depositing dc-arcjet reactor,” *Appl. Opt.*, vol. 36, no. 15, p. 3261, 1997.
- [10] J. Luque, W. Juchmann, E. A. Brinkman, and J. B. Jeffries, “Excited state density distributions of H, C, C₂, and CH by spatially resolved optical emission in a diamond depositing dc-arcjet reactor,” *J. Vac. Sci. Technol. A Vacuum, Surfaces, Film.*, vol.

- 16, no. 2, pp. 397–408, 1998.
- [11] C. Gibaud, J. A. Snyder, V. Sick, and R. P. Lindstedt, “Laser-induced fluorescence measurements and modeling of absolute CH concentrations in strained laminar methane/air diffusion flames,” *Proc. Combust. Inst.*, vol. 30, no. 1, pp. 455–463, 2005.
- [12] J. Kiefer, Z. S. Li, J. Zetterberg, X.-S. Bai, and M. Aldén, “Investigation of local flame structures and statistics in partially premixed turbulent jet flames using simultaneous single-shot CH and OH planar laser-induced fluorescence imaging,” *Combust. Flame*, vol. 154, no. 4, pp. 802–818, 2008.
- [13] K. H. A. Bogart, J. P. Cushing, and E. R. Fisher, “Effects of plasma processing parameters on the surface reactivity of OH(X²I) in tetraethoxysilane/O₂ plasmas during deposition of SiO₂,” *J. Phys. Chem. B*, vol. 101, no. 48, pp. 10016–10023, 1997.
- [14] R. P. Cardoso, T. Belmonte, F. Kosior, G. Henrion, and E. Tixhon, “High-rate deposition by microwave RPECVD at atmospheric pressure,” *Thin Solid Films*, vol. 519, no. 13, pp. 4177–4185, 2011.
- [15] J. Luque, M. Kraus, A. Wokaun, K. Haffner, U. Kogelschatz, and B. Eliasson, “Gas temperature measurement in CH₄/CO₂ dielectric-barrier discharges by optical emission spectroscopy,” *J. Appl. Phys.*, vol. 93, no. 8, pp. 4432–4438, 2003.
- [16] K. H. A. Bogart, J. P. Cushing, and E. R. Fisher, “Surface reactivity measurements for OH radicals during deposition of SiO₂ from tetraethoxysilane/O₂ plasmas,” *Chem. Phys. Lett.*, vol. 267, no. 3–4, pp. 377–383, 1997.
- [17] Q. Xiong *et al.*, “Absolute OH density determination by laser induced fluorescence spectroscopy in an atmospheric pressure RF plasma jet,” *Eur. Phys. J. D*, vol. 66, no. 11, 2012.
- [18] W. Van Gaens and A. Bogaerts, “Kinetic modelling for an atmospheric pressure argon plasma jet in humid air,” *J. Phys. D: Appl. Phys.*, vol. 46, no. 27, p. 275201, 2013.
- [19] D. Schröder, H. Bahre, N. Knake, J. Winter, T. De Los Arcos, and V. Schulz-Von Der Gathen, “Influence of target surfaces on the atomic oxygen distribution in the effluent of a micro-scaled atmospheric pressure plasma jet,” *Plasma Sources Sci. Technol.*, vol. 21, no. 2, 2012.
- [20] J. Janča, A. Tálsky, and V. Zvoniček, “Kinetics of O²⁺ TEOS gas-phase chemical reactions in a remote RF plasma reactor with electron spin resonance,” *Plasma Chem. Plasma Process.*, vol. 16, no. 2, pp. 187–194, 1996.
- [21] D. L. Baulch *et al.*, “Evaluated kinetic data for combustion modelling,” *J. Phys. Chem. Ref. Data*, vol. 21, no. 3, pp. 411–734, 1992.
- [22] Q. Xiong *et al.*, “Absolute OH density determination by laser induced fluorescence spectroscopy in an atmospheric pressure RF plasma jet,” *Eur. Phys. J. D*, vol. 66, no. 11, 2012.
- [23] J. Brian and A. Mitchell, “The dissociative recombination of molecular ions,” *Phys. Rep.*, vol. 186, no. 5, pp. 215–248, 1990.
- [24] J. N. Murrell and J. A. Rodriguez, “Predicted rate constants for the exothermic reactions of ground state oxygen atoms and CH radicals,” *J. Mol. Struct. THEOCHEM*, vol. 139, no. 3–4, pp. 267–276, 1986.
- [25] P. Frank, “A high temperature shock tube study on fast reactions of methylene and methyl radicals,” in *Proc. Int. Symp. Rarefied Gas Dyn*, 1986, vol. 2, pp. 422–426.
- [26] D. A. Lichtin, M. R. Berman, and M. C. Lin, “KINETIC-STUDIES OF LASER

- INITIATED REACTIONS OF CH AND CN RADICALS,” in *Bulletin des Sociétés Chimiques Belges*, 1983, vol. 92, no. 6–7, p. 656.
- [27] W. Tsang and R. F. Hampson, “Chemical Kinetic Data Base for Combustion Chemistry. Part I. Methane and Related Compounds,” *J. Phys. Chem. Ref. Data*, vol. 15, no. 3, pp. 1087–1279, 1986.
- [28] D. L. Baulch *et al.*, “Evaluated Kinetic Data for Combustion Modeling : Supplement II Thermochemical analysis and kinetics aspects for a chemical model for camphene ozonolysis Evaluated Kinetic Data for Combustion Modeling : Supplement II,” vol. 757, no. 2005, 2012.

5

GENERAL CONCLUSIONS & OUTLOOKS

Over this work, a poly-diagnostic study of an atmospheric pressure plasma jet working in Ar/TEOS mixture was carried out by means of several ex-situ surface techniques combined with advanced gas-phase diagnostic methods. SiO₂-based thin films exhibiting a well-defined chemistry, a good morphological structure and high uniformity were studied in detail by FTIR, XPS, AFM and SEM analysis, while non-intrusive passive spectroscopy techniques (OES, filter imaging) and laser active spectroscopic methods (Rayleigh scattering, LIF and TALIF) were employed to shed light on the complexity of gas-phase mechanisms involved in the deposition process.

Even though proper conclusions were already drawn over previous chapters, a global results discussion is strongly required to further clarify the obtained result and identify a potential correlation between the most significant gas-phase processes and the surface features of the plasma-deposited films.

By combining the surface characterization results presented in Chapter 2 with gas-phase analysis outputs reported in Chapter 3 it is possible to deduce that after 60 s of plasma treatment at high power conditions (12 kV-12 kHz) and 409 K of gas temperature (Table 3.2), the surface temperature reaches a maximum value of 340 K (Figure 2.23), while the thin film surface appears full of defect as revealed by AFM (Figure 2.18) and SEM (Figure 2.21) analysis. On the other hand, plasma polymerization of silica-like thin films completely free from defect were successfully achieved on thermo-sensitive substrates under the lowest power conditions tested (6 kV-12 kHz). The results obtained pointed out the key role of thermal stress in defect formation and the maximum substrate temperature permitted (around 320 K) in case of deposition processes performed onto polypropylene foils. Therefore, two different spectroscopic methods for gas temperature (T_{gas}) measurements were proposed in order to provide an adequate control of the APPJ-assisted polymerization process. The rotational temperature of OH excited radicals obtained by OES, in the assumption of a non-Boltzmann rotational distribution, was found in a good agreement with Rayleigh scattering results thus revealing the possibility of using low-cost diagnostic equipments for in-situ temperature monitoring of atmospheric pressure Ar plasma as well as Ar/TEOS plasmas.

Apart from having a central role in the definition of thin film properties, the gas temperature has a strong influence on the kinetics of gas-phase reactions. The effect of power applied and, consequently, T_{gas} , as well as of TEOS admixture on ground-state O atoms, CH and OH radical production and recombination mechanisms was discussed in

detail by LIF and TALIF imaging. The spatial profile of the O TALIF signals, detected along the y-axis in Ar/TEOS mixture (Figure 4.10), highlighted an almost constant O atoms flux near the PP target as a function of the power applied, thus excluding differences in terms of gas-surface reactions between O atoms and thin films organic compounds. These results seem confirmed also by FTIR and XPS measurements, presented in Figure 2.13 and Table 2.1 respectively, which have shown thin films chemical compositions almost unchanged for all cases tested. Nevertheless, the O atoms, OH and CH radicals behaviours at 1.5 mm of distance from the HV tip (Figure 4.15) have revealed the dominant role of O atoms in hydrocarbon fragments dissociation processes, therefore highlighting the presence of oxidation mechanisms with an active role in the gas-phase inorganic unit formation. In order to establish the role of oxygen atoms in TEOS dissociation, a complementary gas-phase analysis of stable molecules produced during the treatment, by means of Gas Chromatography or Fourier-transform infrared spectroscopy, is strongly required. On the other hand, the importance of O atoms surface reactions in the achievement of pure silica layers onto thermo-sensitive substrates will be further clarified by performing post-treatments of the deposited thin films by means of oxygen-based plasmas. The thin film organic content as function of the post treatment time will be discussed by XPS analysis while SEM results will be used to detect an additional thermal stress induced by the plasma treatment.

Moreover, time-resolved electron density behaviour and excited species emission profiles (Figure 3.8), along with 2D imaging data of both excited (Figure 3.9) and ground species (Figure 4.12 - 4.14), were used to reveal the predominant gas-phase mechanisms induced by Ar metastable, electron or active species reactions. It was concluded that, whereas the O atom and OH radical generation is mostly determined by the dissociation of water molecules as already stated in the past in case of pure Ar discharges, an extensive understanding of the main TEOS dissociation products generated during the deposition process is crucial to identify the most significant CH radical production mechanisms. For the first time, a simplified model for CH radical formation in Ar/TEOS mixture has been proposed (Figure 3.5) by revealing the dominant role of Ar^m in TEOS dissociation processes.

Despite the above-mentioned experimental findings, which have provided useful preliminary informations about dominant gas-phase processes in Ar/TEOS plasmas, additional efforts are still required for quantitative measurements of active species in case of thin film deposition processes. The almost complete absence of reference data about monomer fragmentation pathways and relative quenching rates in case of Ar/TEOS plasma is only one of the barriers towards absolute density measurements. In fact, all the possible laser-excited states depopulation processes, such as rotational (RET) and vibrational (VET) energy transfer processes must be taken into account for a proper interpretation of the LIF and TALIF experimental results. Moreover, the influence on the fluorescence signal intensity of possible Mie scattering phenomena due to the presence of nanoparticles nucleated during the gas-phase process, must be properly estimated in order to avoid significant measurements errors. In light of this, the most significant collisional energy transfer processes taking place in Ar/air/TEOS mixtures, as well as the possible signal interferences caused by dust particles will be studied in detail with the objective of developing new LIF models for OH and CH radical absolute density calculation.

Lastly, the spatial distribution of CH radicals, Rayleigh scattering images and surface results were used to prove that the most important nucleation processes take place in the gas-phase. Indeed, besides the low CH signal detected in correspondence of the dielectric

plate as well as the strong Mie scattering signal recorded along the y-axis, AFM images of thin films deposited under the highest value of applied power (12 kV-12 kHz) revealed a surface microstructure characterized by a large amount of powder-like features (Figure 2.18), typically caused by the predominant role of gas-phase nucleation processes and subsequent deposition of dust particles on the target. However, at the same time, the presence of dust particles densely packed on the substrate was revealed by SEM images (Figure 2.21) and, consequently, the possibility of other mechanisms of formation at the gas-substrate interface cannot be excluded.

In conclusion, despite these surface and gas-phase results are just a small step towards an in-depth understanding of the deposition process mechanisms, the poly-diagnostic approach prosed in this work opens interesting perspectives both in terms of process control and development of new computational models. In particular, beside clarifying the key parameters to be monitored in case of APPJ-assisted deposition processes, such as T_{gas} , electrons and Ar metastables density, the experimental results obtained could potentially be used for the validation of simulation outputs. Much work still remains to be done to gather all the data required to complete this task and further collaborations between researchers of different fields, such as material science and physics, are strongly required for a full understanding of the process.

Annex I

Novel method for NH-rich coatings engineering by means of aerosol assisted atmospheric pressure plasma deposition ^a

<https://doi.org/10.1016/j.matlet.2017.11.116>

^a © 2017 Elsevier. Reprinted, with permission from [F. Barletta, A. Liguori, Ch. Leys, V. Colombo, M. Gherardi, A. Nikiforov, Novel method for NH-rich coatings engineering by means of aerosol assisted atmospheric pressure plasma deposition, Materials Letters, March 2018]



Novel method for NH-rich coatings engineering by means of aerosol assisted atmospheric pressure plasma deposition

F. Barletta^a, A. Liguori^b, Ch. Leys^c, V. Colombo^{a,b}, M. Gherardi^{a,b}, A. Nikiforov^{c,*}

^aAlma Mater Studiorum – Università di Bologna, Dipartimento di Ingegneria Industriale (DIN), Via Saragozza 8, 40123 Bologna, Italy

^bAdvanced Mechanics and Materials, Interdepartmental Center for Industrial Research (AMM-ICIR), Alma Mater Studiorum – Università di Bologna, Bologna, Italy

^cDepartment of Applied Physics, Ghent University, Sint-Pietersnieuwstraat 41, Gent 9000, Belgium

ARTICLE INFO

Article history:

Received 26 October 2017

Received in revised form 24 November 2017

Accepted 25 November 2017

Keywords:

Plasma aerosol deposition

Amide rich coatings

Biomaterials

ABSTRACT

Amine/amide-rich coatings possessing good biocompatibility are of high interest in the medical field. A new type of coatings with high content of NH groups has been prepared in a single step plasma process. Deposition is performed by atmospheric pressure plasma which is coupled to aerosol injection of liquid precursor. The method is applied for the polymerization of *N,N'*-methylenebisacrylamide precursor. The surface analyses, including X-ray photoelectron spectroscopy (XPS) and Fourier Transform Infrared spectroscopy (FTIR), show polymerization of the precursor with formation of amide-rich coatings with up to 8 at.% of N-containing groups. The coatings are stable in phosphate buffer saline (PBS) solution and characterized by improved biocompatibility to STEM cells.

© 2017 Elsevier B.V. All rights reserved.

1. Introduction

Engineering of biomaterials is one of the fastest growing fields of applied science. Nowadays numerous medical devices are made from polymers. One of the most used polymers is polyethylene (PE), however successful incorporation of PE based biomaterials in recipient body is compromised by low cells adhesion and proliferation [1]. The state of the art approach to solve the problem is modifying the surface of the polymeric substrate. Plasma enhanced chemical vapour deposition (PECVD) is considered to be such a method capable to deposit coatings with controlled surface morphology and chemistry [2]. Amine/amide group functionalized coatings are shown to improve interaction of cells with polymer materials by means of covalent bonding and electrostatic interactions [3]. Among different methods to introduce such groups, the use of a volatile allylamine precursor or its derivatives is the most developed [4]. The drawback of the method is the stability of the coatings in solutions. It is known that PECVD at low power leads to high solubility of the coatings preventing biomedical applications [5]. On the other hand, the use of high plasma power leads to the formation of stable films, but reduces the percentage of amines due to precursor fragmentation [6]. Here we tested an approach for deposition of amine/amide rich coatings based on aerosol assisted plasma deposition (AAPD). The principles of novel

AAPD processing are described by *F. Fanelli et al.* [7]. In this work, the AAPD approach has been adapted to deposit films at low plasma power keeping precursor functionality, but still producing stable films through the use of an appropriate precursor, which is a low-volatile amide containing agent *N,N'*-methylenebisacrylamide (MBA). Recently, *F. Arefi-Khonsari et al.* [8,9] have successfully used MBA as cross-linking agent with acrylic acid in PECVD in order to improve water stability of the coatings. The approach has shown the possibility to engineer water stable films but only at high plasma power and relatively high gas-/substrate temperature.

2. Experimental

The deposition was carried out on PE substrate by means of a single electrode plasma jet, developed in the University of Bologna [10,11]. The plasma is excited by a 10 kHz bipolar high voltage signal of 15 kV amplitude (AlmaPulse, Almaplasm srl). The schematic of the setup is presented in Fig. 1. He was used as plasma gas while a flow rate of 1 standard litre per minute (slm) was set using a digital mass flow controller (Bronkhorst, El-flow®). The main gas flow is passed through the primary channel while a precursor *N,N'*-methylenebisacrylamide (Sigma-Aldrich), in aerosol form, is injected through the secondary jet channel. Up to our knowledge, no attempts have been made so far to polymerize solely MBA due to its low volatility. In the present work, this issue is overcome by injection of MBA solution directly in the discharge

* Corresponding author.

E-mail address: anton.nikiforov@ugent.be (A. Nikiforov).

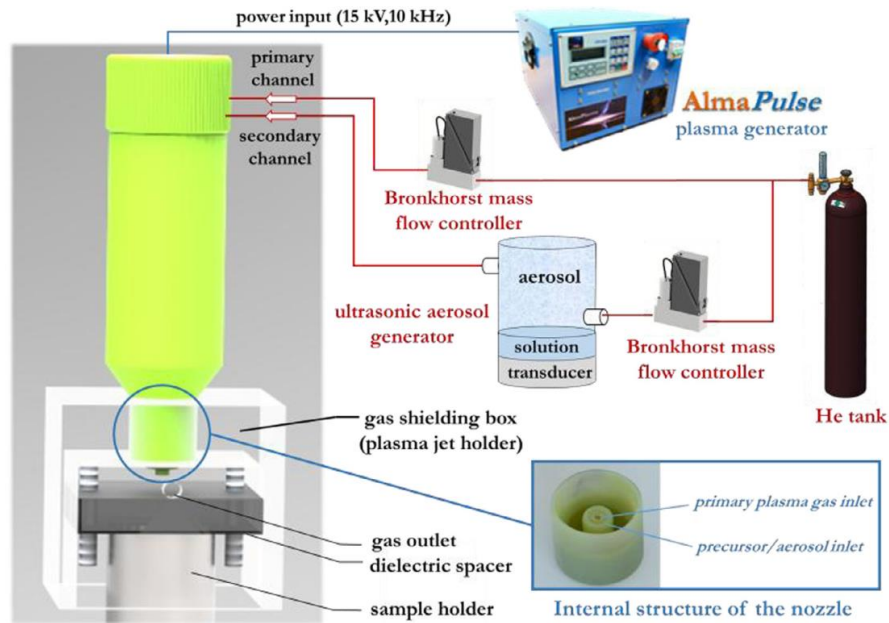


Fig. 1. The aerosol assisted plasma deposition system and photo of the internal structure of the plasma jet nozzle.

in form of aerosol with droplets size below $1\ \mu\text{m}$. The surface chemistry of the coatings was determined by XPS and FTIR spectroscopy.

Biocompatibility of the coatings was tested qualitatively by an assay with STEM cells. The live/dead cell staining was used to evaluate cell viability by fluorescence imaging.

3. Results and discussions

The capability of plasma assisted deposition of NH-rich coatings was tested through 1 min AAPD on PE films. FTIR spectrum reveals precursor polymerization and formation of NH-rich coatings as presented in Fig. 2.

The FTIR spectrum of MBA monomer is characterized by a strong absorption peak around $3380\text{--}3290\ \text{cm}^{-1}$ corresponding to secondary amine N–H stretching vibration, as well as by strong narrow peaks corresponding to deformation vibration of secondary amine at 1545 , 1627 and $1660\ \text{cm}^{-1}$ [12]. Polymerization of MBA results in strong broadening of N–H bands in both regions, similarly to polymerized allylamine coatings [5]. This effect is visible in Fig. 2 where the plasma coating is characterized by broad

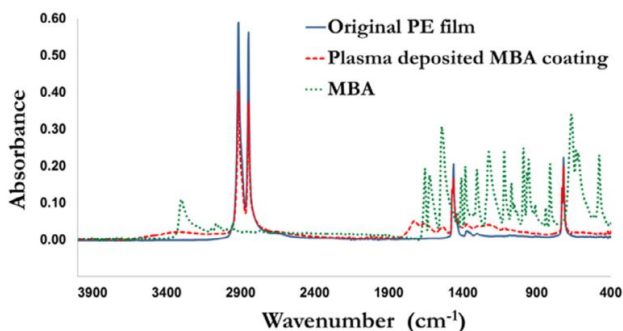


Fig. 2. FTIR spectrum of a coating deposited by plasma jet with MBA as precursor. FTIR spectra of original PE film and MBA are provided for comparison.

branches at $3400\text{--}3200\ \text{cm}^{-1}$ and $1800\text{--}1500\ \text{cm}^{-1}$ corresponding to polymerized film rich of NH-functional groups. The deposited polymer has been tested for stability by exposure for 24 h to PBS. As known, MBA is highly soluble in water based solutions; however, the plasma polymerized film has shown high stability and all characteristic FTIR peaks presented in Fig. 2 are detected after the stability tests. It is an important observation as, usually, stability of NH-rich films obtained from allylamine by PECVD processing is low and most of functionality is lost in first hours of water exposure [13].

Chemical composition of the coatings has been studied also by XPS analysis. Survey and high resolution spectra of N1s with deconvolution of the profile are presented in Fig. 3. The coating contains around 75 at.% of C, 14.7 at.% of O and as high as 8 at.% of N atoms at the surface of the deposits; with respect to the MBA precursor, a small increase of C (MBA: 70.3 at.%) and almost no change of O content (MBA: 14.5 at.%) are observed. The latter result probably indicates that oxidation of the precursor is considerably low during the deposition. The concentration of N drops significantly from 15.2 at.% in MBA to about 8 at.% in the coating. This result correlates well with FTIR measurements where considerable changes of the MBA structure due to polymerization were observed. Probably the precursor fragmentation and polymerization lead to the decrease of –NH bonds and to the reduction of N content in the film, as confirmed by XPS.

Indeed plasma polymerization can lead to an undesirable decrease of NH-functional groups in the coatings. Deconvolution of high resolution N1s peak, presented in Fig. 3b) has been carried out following [14] with assignments of N peaks as amines (398.9–399.3 eV), amides (399.8 eV), quaternary amines (401.3–401.5 eV) and –NO₂ groups (406–407 eV). The deconvolution results confirm that nitro groups are not formed due to absence of O₂ in the mixture. However, plasma fragmentation of the precursor is observed to affect the composition of N-containing groups, as amine groups (around 12.2%) and quaternary amines (around 17.4%) are present in the film, see Fig. 3b). Main contribution of 70.4% to N-containing groups is assigned to amide OC=NH– groups. Such high amount of amide groups can be indicative for good biocompatibility of the samples. The biocompatibility of PE film coated by the AAPD pro-

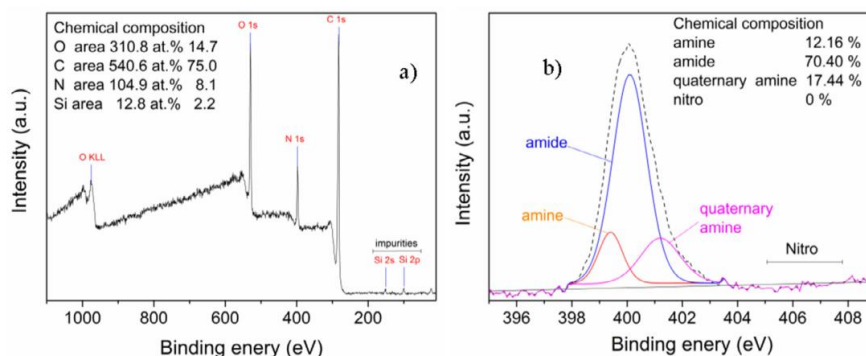


Fig. 3. Survey XPS spectra of the MBA films (a); deconvolution of N1s peak (b).

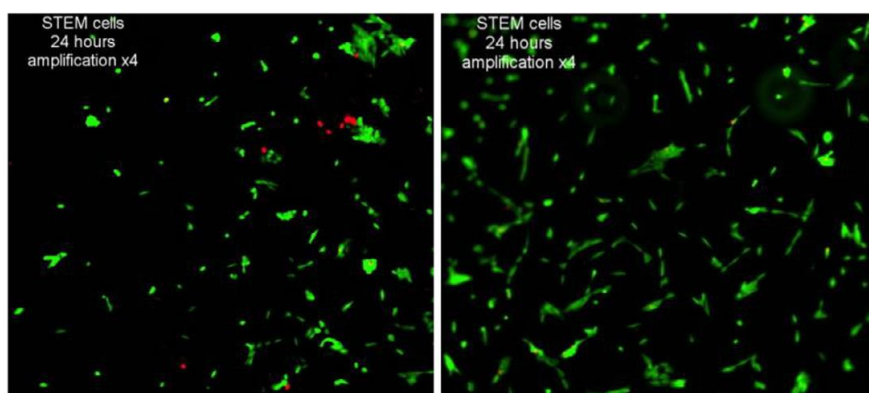


Fig. 4. STEM cell proliferation and morphology tests for a) untreated PE (control) and b) PE coated with MBA.

cess has been checked through qualitative cell assay tests. The representative averaged viability results of cell assay are presented in Fig. 4.

The control PE film has a surface chemistry which does not provide strong adhesion of the STEM cells and, correspondingly, the cells proliferation is rather limited, resulting in low cell viability. The fluorescence microscopy shows retracted round shaped cells indicating high stress on the cells. There is almost no spreading of the cells on the surface and a considerable amount of dead cells is, as indicated by red fluorescence signal. On the other hand, MBA plasma coated samples are characterized by cells having extended shape and spreading over the surface of the film. No dead cells are observed and that, together with the morphology of the STEM cells, indicate good cell-substrate interaction and improved biocompatibility.

4. Conclusion

A new method of plasma deposition coupled with direct aerosol injection of the precursor is tested for engineering of NH-rich coatings. An atmospheric pressure plasma jet is used for deposition process with *N,N'*-methylenebisacrylamide. Polymerization of the MBA is confirmed by broadening of IR band at 1800–1600 cm^{-1} . Up to 8 at.% of N containing bonds with mainly amide groups is determined in the coatings. Deposited films are stable in water based solutions and characterized by improved biocompatibility. The obtained results suggest that the new approach for coatings engineering based on aerosol injection can be applied for manufacturing of biomaterials.

Acknowledgements

The authors thank for support the Institute of Advanced Studies - Alma Mater Studiorum-Università di Bologna, the M.Era-Net project PlasmaTex IWT140812 and FWO funding, project V408517N.

References

- [1] L.G. Griffith, Polymeric biomaterials, *Acta Mater.* 48 (2000) 263–277.
- [2] P. Chu, Plasma-surface modification of biomaterials, *Mater. Sci. Eng. R Reports.* 36 (2002) 143–206.
- [3] A.A. Meyer-Plath, K. Schröder, B. Finke, A. Ohl, Current trends in biomaterial surface functionalization – Nitrogen-containing plasma assisted processes with enhanced selectivity, *User Model. User-Adapt. Interact.* 71 (2003) 391–406.
- [4] P. Hamerli, T. Weigel, T. Groth, D. Paul, Surface properties of and cell adhesion onto allylamine-plasma-coated polyethyleneterephthalat membranes, *Biomaterials* 24 (2003) 3989–3999.
- [5] G. Aziz, N. De Geyter, H. Declercq, R. Cornelissen, R. Morent, Incorporation of amine moieties onto ultra-high molecular weight polyethylene (UHMWPE) surface via plasma and UV polymerization of allylamine, *Surf. Coatings Technol.* 271 (2015) 39–47.
- [6] L. Denis, D. Cossement, T. Godfroid, F. Renaux, C. Bittencourt, R. Snyders, M. Heccq, Synthesis of allylamine plasma polymer films: correlation between plasma diagnostic and film characteristics, *Plasma Process. Polym.* 6 (2009) 199–208.
- [7] F. Fanelli, F. Fracassi, Aerosol-assisted atmospheric pressure cold plasma deposition of organic-inorganic nanocomposite coatings, *Plasma Chem. Plasma Process.* 473–487 (2014).
- [8] O. Carton, D.B. Salem, J. Pulpytel, F. Arefi-Khonsari, Improvement of the water stability of plasma polymerized acrylic acid/MBA coatings deposited by atmospheric pressure air plasma jet, *Plasma Chem. Plasma Process.* 35 (2015) 819–829.
- [9] D.B. Salem, O. Carton, H. Fakhori, J. Pulpytel, F. Arefi-Khonsari, Deposition of water stable plasma polymerized acrylic acid/MBA organic coatings by atmospheric pressure air plasma jet, *Plasma Process. Plasma Polym.* 11 (2014) 269–278.

- [10] A. Liguori, A. Pollicino, A. Stancampiano, F. Tarterini, M.L. Focarete, V. Colombo, M. Gherardi, Deposition of plasma-polymerized polyacrylic acid coatings by a non-equilibrium atmospheric pressure nanopulsed plasma jet, *Plasma Process. Polym.* 13 (2016) 375–386.
- [11] A. Liguori, E. Traldi, E. Toccaceli, R. Laurita, A. Pollicino, M.L. Focarete, V. Colombo, M. Gherardi, Co-deposition of plasma-polymerized polyacrylic acid and silver nanoparticles for the production of nanocomposite coatings using a non-equilibrium atmospheric pressure plasma jet, *Plasma Process. Polym.* 13 (2016) 623–632.
- [12] R.A. Heacock, L. Marion, The infrared spectra of secondary amines and their salts, *Can. J. Chem.* 34 (1956) 1782–1795.
- [13] A. Manakhov, L. Zajíčková, M. Eliáš, J. Čechal, J. Polčák, J. Hnilica, Š. Bittnerová, D. Nečas, Optimization of cyclopropylamine plasma polymerization toward enhanced layer stability in contact with water, *Plasma Process. Polym.* 11 (2014) 532–544.
- [14] T.R. Gengenbach, R.C. Chatelier, H.J. Griesser, Characterization of the ageing of plasma-deposited polymer films: global analysis of X-ray photoelectron spectroscopy data, *Surf. Interface Anal.* 24 (1996) 271–281.

Acknowledgement

A PhD is so much more than a degree, it's about becoming who you are meant to be. It can break you down into your most vulnerable form but has the potential to put you back together stronger than before. The process for becoming a determined, resilient and skilled researcher takes time and patience and can't be possible without the support of friends, family and scientific mentors. Although words cannot express my gratitude, I will try my best to acknowledge them.

First of all, I would like to thank my academic supervisor, Prof. Vittorio Colombo, for choosing me among many, for introducing me in the research world, teaching me to never took anything for granted or unreachable and especially for his utmost sincerity.

My sincerest thanks to my co-supervisor Dr. Matteo Gherardi for believing in me, for making me realize my strengths and my mistakes and listen to my views. A few lines aren't enough to describe what it's meant to me meeting him but I can sum up by saying that, without him, this experience just wouldn't have been the same.

My special heartfelt thanks to Dr. Anton Nikiforov for the enthusiasm, the knowledge and the kindness. I'm grateful to him for all the scientific discussions and for teaching me so much in such a short period of time. He remains my best role model for a researcher, always willing to contribute with his experience and knowledge to addressing new challenges of the plasma community.

I would also like to thank Dr. Nikolay Britun for helping me during the month spent in Mons, for passing on me his passion for plasma diagnostic and for his scientific attitude and great professionalism.

I am also grateful to my favourite labmates Emanuele Simoncelli, Tommaso Galligani, Filippo Capelli and Giulia Laghi. Words cannot express how grateful I am for their friendship, patience and confidence. Thanks to Emanuele for all the time spent together talking about life and science, for making me a better person and for supporting me every single day of this experience. Thanks to Tommaso for becoming an important part of my life, for the "everyday call", for the mutual admiration and for every scientific and personal challenge faced together. Thanks to Filippo for the humour, for facing each day with optimism and for making me stronger. Thanks to Giulia for believing in every proposal I've presented, for helping me stop being so focused on me and for all the cracked thin films obtained together. Lastly, thanks also to all the other colleagues for the time spent together and the memories.

Thanks to my parents, Giorgio and Monica, for all the love, the sacrifices and the support in every single day of my life. I know for sure that I could not ask a better family than this. Last but not least, thanks to Federico, the most important person of my life now and always, for being always on my side and believing in me more than anyone else.

*Bologna, October 2019
Federica Barletta*